UNIVERSITÀ
DI PARMA

UNIVERSITÀ DEGLI STUDI DI PARMA

DIPARTIMENTO DI SCIENZE MATEMATICHE, FISICHE E INFORMATICHE

DOTTORATO DI RICERCA IN FISICA

CICLO XXXVII

DESIGN AND CHARACTERIZATION OF SUPRAMOLECULAR CONSTRUCTS FOR PD-L1 TARGETED PHOTOIMMUNOTHERAPY

Coordinatrice:

Chiar.ma Prof.ssa Raffaella Burioni

Tutor:

Chiar.ma Prof.ssa Stefania Abbruzzetti

Dottoranda:

Manuela Maria Alampi

Anni accademici 2021/2022 - 2023/2024

Alla mia famiglia, quella di origine e quella che ho scelto lungo il cammino.

Un particolare grazie a mamma, Federica e Filippo.

"Nel mondo nulla di grande è stato fatto senza passione"

Georg W.F. Hegel

Abstract

Cancer remains a critical global health challenge, affecting nearly 20 million individuals and causing approximately 10 million deaths annually[1]. Conventional treatments, including surgical intervention, radiation therapy, and chemotherapy, are often inadequate for many patients. Emerging therapeutic resistance and intrinsic tumor heterogeneity contribute to these limitations[2]. Recent technological advances have enabled the combination of photodynamic therapy (PDT) and immunotherapy, leveraging immunoconjugates that combine photosensitizing and targeting capabilities[3,4]. Traditionally, the surface density of tumor-specific receptors and immune checkpoints, such as programmed death-ligand 1 (PD-L1), is considered a key determinant of therapeutic success in these treatments[5].

This thesis presents a novel photoactive supramolecular system designed to selectively target PD-L1 and investigate its role in predicting the efficacy of photoimmunotherapy. Atezolizumab, an FDA-approved checkpoint inhibitor, was conjugated with either the photosensitizer eosin 5-isothiocyanate (EITC) for targeted photoimmunotherapy of PD-L1, or the fluorescent probe Alexa Fluor 647 for imaging. First, we quantified membrane-bound PD-L1 in two human non-small cell lung cancer (NSCLC) cell lines expressing PD-L1 to a different level using direct stochastic optical reconstruction microscopy (dSTORM)[6]. This high-resolution imaging technique allowed us not only to estimate receptor density precisely but also to assess atezolizumab's binding affinity to its target. We conducted a comprehensive photophysical characterization of the EITC-atezolizumab photoimmunoconjugate using steady-state and time-resolved spectroscopic techniques. Next, we demonstrated the effectiveness of the conjugate for photoimmunotherapy, showing that it can induce significant cytotoxicity producing reactive oxygen species upon light exposure. However, our findings revealed no significant correlation between the density of PD-L1 receptors on the cell surface and the efficacy of PDT treatment. Notably, cells with both high and low PD-L1 expression showed similar responses to the treatment, suggesting that receptor density alone may not predict therapeutic success. These results challenge the conventional assumption that high PD-L1 expression is required for effective PD-L1-targeted therapies, suggesting broader clinical applicability of this approach to tumors with heterogeneous or low PD-L1 levels[7]. Additionally, we explored photochemical internalization (PCI) as a strategy to enhance drug delivery through light activation[8]. Although PCI significantly enhanced the internalization of macromolecules like gelonin, it did not enhance PDT efficacy when combined with PD-L1 blockade. Confocal microscopy was employed

to investigate the intracellular trafficking of the conjugate, revealing that PD-L1 may undergo recycling after internalization. However, recycling may limit the sustained efficacy of atezolizumab in NSCLC, as the re-expression of functional PD-L1 on the cell surface potentially diminishes long-term therapeutic effects[9]. Future experiments will be necessary to elucidate this aspect. These findings broaden the potential clinical applications of PD-L1-targeted photoimmunotherapy, suggesting adaptability even in tumors with low or heterogeneous PD-L1 expression.

Publications and Contributions

Publications Related to This Thesis:

- Delcanale P, Alampi MM, Mussini A, Fumarola C, Galetti M, Petronini PG, Viappiani C, Bruno S, Abbruzzetti S. *A Photoactive Supramolecular Complex Targeting PD-L1 Reveals a Weak Correlation between Photoactivation Efficiency and Receptor Expression Levels in Non-Small-Cell Lung Cancer Tumor Models*. Pharmaceutics. **2023**; 15(12):2776. https://doi.org/10.3390/pharmaceutics15122776

Other Publications:

- Porciani D, Alampi MM, Abbruzzetti S, Viappiani C, Delcanale P. *Fluorescence Correlation Spectroscopy as a Versatile Method to Define Aptamer-Protein Interactions with Single-Molecule Sensitivity*. Anal Chem. **2024**; 96(1):137-144. https://doi.org/10.1021/acs.analchem.3c03341.

Poster communication:

- Alampi MM, Delcanale P, Mussini A, Fumarola C, Galetti M, Petronini PG, Viappiani C and Abbruzzetti S. *A Photoactive Supramolecular Complex Targeting PD-L1 Reveals a Weak Correlation between Photoactivation Efficiency and Receptor Expression Levels in Non-Small-Cell Lung Cancer Tumor Models*. XXVII Congresso Nazionale SIBPA 2024, Genova (Italy) June 16th –20th 2024

Contents

Chapter 1

Introduction

In 2022, the International Agency for Research on Cancer estimated 20 million new cancer cases and nearly 10 million cancer-related deaths worldwide, confirming cancer as the most aggressive form of noncommunicable diseases[1]. Cancer remains one of the most pressing global health challenges, with enormous social, economic, and political implications. Aging populations, lifestyle changes, and environmental factors increase the global cancer burden, heavily straining healthcare systems and economies worldwide.

Lung cancer is one of the most prevalent and deadliest cancers, accounting for over 2 million new cases and nearly 1.8 million deaths globally each year[1]. The high mortality rate is often explained by the late-stage diagnosis, the aggressive nature of lung tumors, and the frequent development of resistance to standard therapies which significantly limit long-term survival outcomes[2]. Lung cancer is divided into small cell lung cancer (SCLC) and non-small cell lung cancer (NSCLC), with NSCLC comprising about 85% of cases.[10]. SCLC is generally more aggressive and strongly associated with a history of smoking, while NSCLC includes several subtypes, with adenocarcinoma being the most common. Several key factors contribute to the poor prognosis of lung cancer, especially the development of resistance to therapies and the late detection of the disease, with approximately 70% of patients diagnosed at locally advanced (stage III) or metastatic (stage IV) stages[2].

Therapies for lung cancer are selected based on the type and molecular characteristics of the tumor. Traditional treatment options include surgery, radiation therapy, and chemotherapy, which are often used in combination depending on the stage of the disease. Surgery remains the cornerstone of treatment for early-stage NSCLC, while chemotherapy, typically with platinum-based agents, and radiation therapy are more commonly used for advanced or metastatic cases[10]. However, despite the progress in these conventional therapies, the prognosis remains poor, with a 5-year survival rate for localized lung cancer of approximately 60%, that drops dramatically to around 6% for metastatic cases, where cancer has spread beyond the lungs[11]. Recent advances in targeted therapies and immunotherapies provide new hope for patients with advanced NSCLC. One of the most notable breakthroughs has

been the development of immune checkpoint inhibitors (ICIs), such as pembrolizumab, nivolumab, and atezolizumab, which aim to improve the body's immune response against tumors. These therapies target inhibitory receptors such as PD-L1 and CTLA-4, which cancer cells exploit to evade immune surveillance. By blocking these immune checkpoints, ICIs restore T-cell function, allowing the immune system to attack and destroy cancer cells. ICIs have demonstrated improved survival in patients with NSCLC, especially in those with high PD-L1 expression (approximately 25–30% of NSCLC), and have become a mainstay in the treatment of advanced tumors[2]. However, resistance to ICIs, both primary and acquired, remains a major challenge, with only 20-30% of patients responding effectively to these treatments. These limitations highlight the need for new strategies and more accurate biomarkers to predict ICIs efficacy and improve patient outcomes[12].

Among the most promising approaches is photodynamic therapy (PDT), a light-based treatment modality that has garnered increasing attention for its precision and versatility in oncology. PDT uses photosensitizers (PSs) that, when activated by a specific wavelength of light, generate reactive oxygen species (ROS) to target cell death. The origins of light-based therapies date back to ancient times, with sunlight being applied to treat skin conditions like vitiligo[13]. However, the photodynamic effect was scientifically demonstrated only in the early 1900s by Oscar Raab, who showed that acridine red dyes could kill microorganisms, but only in the presence of light[14]. Later, his mentor Hermann von Tappeiner expanded on this work and coined the term "photodynamic action" after successfully treating six patients with basal cell carcinoma using eosin and white light. This term specifically refers to light-activated processes that lead to cell death in the presence of oxygen[15–17]. Modern PDT advanced with the development of lasers and effective light-sensitive agents in the 1960s and 1970s, setting the stage for its current applications in oncology. A key milestone was the development of the hematoporphyrin derivative (HpD) by Lipson and Schwartz, which led to the approval of Photofrin® as the first FDA-approved PS for cancer treatment in the 1990s[18]. Since then, PDT continues to evolve, with second- and third-generation PSs developed to improve selectivity, reduce side effects, and enhance efficacy across a range of cancers and other diseases.

Given the limitations of current NSCLC therapies, this thesis aims to explore innovative strategies that combine PDT with immunotherapy to enhance treatment efficacy. Chapter 2 and Chapter 3 lay the theoretical groundwork, outlining the photophysical principles underlying the light-based therapies investigated in this work, namely, photodynamic therapy and photochemical internalization. These chapters provide the essential background needed to understand how these approaches leverage light activation for therapeutic purposes. A key objective of this research is the development of a novel photoactive construct designed to selectively bind to PD-L1 and induce light-mediated cytotoxic effects. Leveraging the specificity of the monoclonal antibody atezolizumab, which targets PD-L1, this construct is conjugated with a PS to achieve localized cytotoxicity in response to light exposure. By combining immune checkpoint blockade with PDT, this dual strategy aims not only to directly kill

tumor cells but also to modulate the tumor microenvironment, enhancing the immune system's ability to combat cancer. In Chapter 4, the components of the photoimmunoconjugate, atezolizumab as the targeting system and EITC as the active payload, are described in detail, along with an overview of the target, PD-L1. The synthesis and characterization of this photoimmunoconjugate, including its binding affinity and photophysical properties, are thoroughly examined in Section 5.3 and Section 5.4. An additional hypothesis explored in this thesis is the potential correlation between PD-L1 density on cancer cells and the outcome of photodynamic treatment. As a critical immune checkpoint protein, PD-L1 plays a central role in tumor immune evasion and is a key target for photoimmunotherpay. Given the heterogeneous nature of PD-L1 expression across different tumors, an advanced imaging approach, detailed in Section 5.5, was employed to quantify PD-L1 density in various NSCLC cell lines. This analysis served as the foundation for subsequent studies to assess whether higher PD-L1 expression correlates with increased binding and accumulation of the photoimmunoconjugate, thereby amplifying the photodynamic effect. Section 6.3 investigates whether PD-L1 expression levels could be used as a predictive marker for therapy response, potentially offering a more personalized treatment strategy. In addition, in light of the challenges posed by the hypoxic tumor microenvironment and limited uptake of PSs, this thesis explores the integration of photochemical internalization (PCI) with photoimmunotherapy. PCI represents a promising approach for enhancing intracellular delivery of therapeutic agents, ensuring that even when cancer cells exhibit resistance mechanisms, such as poor drug uptake or sequestration in endocytic vesicles, the therapeutic payload can still reach critical intracellular targets. This strategy is thoroughly evaluated in Section 6.6, with particular attention to its impact on improving the overall efficacy of the treatment, especially in NSCLC cells that express low levels of PD-L1 or are otherwise less responsive to standard therapies. A final focus of this thesis is the investigation of PD-L1's intracellular trafficking, as its localization and distribution within the cell may influence the effectiveness of photoimmunotherapy. Section 6.7 explores this by investigating the accumulation of PD-L1 in intracellular organelles, such as endosomes and lysosomes, after binding with the atezolizumab-based immunoconjugate. This analysis helped to clarify how PD-L1 internalization and its subsequent subcellular localization impact the therapeutic outcomes of photoimmunotherapy. Through these investigations, this thesis aims to contribute to a more comprehensive understanding of NSCLC treatment by combining the precision of immune-targeted therapies with the cytotoxic potential of light-activated compounds. Moreover, by addressing the limitations of current therapeutic strategies, this work aspires to improve treatment outcomes for patients with limited therapeutic options, particularly those affected by NSCLC.

In addition to the work presented here, during the PhD I actively contributed to other research projects, including a recently published study on aptamer-protein interactions using fluorescence correlation spectroscopy (FCS) (Analytical Chemistry **2024** 96(1), 137-144). This project demonstrated

FCS as a highly sensitive method for quantifying aptamers binding affinities and kinetics at the single-molecule level, offering a more precise alternative to conventional bulk techniques.

Chapter 2

Photodynamic Therapy

Photodynamic therapy (PDT) is a minimally invasive treatment used in a wide range of clinical applications for both malignant and nonmalignant conditions[19]. Its therapeutic effect depends on the interaction of three essential components: a photosensitizer (PS), visible or near-infrared light, and molecular oxygen. Individually, these components are harmless, but when combined, they trigger photosensitized reactions that generate cytotoxic reactive oxygen species (ROS), with singlet oxygen being the most biologically significant. In cancer therapy, PDT can kill tumor cells through three main mechanisms: direct ROS-mediated damage to cancer cells, disruption of the tumor vasculature, and activation of the immune system[20]. The efficacy depends on factors like the PS type, subcellular localization, dose, and light fluence. The time between the administration of the PS to the patient and light activation, known as the drug-to-light interval, is another critical factor for optimizing treatment outcomes. This interval can range from minutes to days, depending on the PS's pharmacokinetics[20]. One key advantage of PDT is its high specificity for target cells, achieved by the selective accumulation of the PS in targeted tissues and the localized application of light to the treatment area. This two-tiered targeting minimizes collateral damage to healthy tissues, making PDT effective for treating accessible or localized tumors, such as those in the skin, head, neck, and lungs[13]. Despite these advantages, PDT faces significant limitations with metastatic or disseminated cancers. One major obstacle is the inability to effectively treat metastatic tumors that are deeply embedded or spread across the body. Since PDT requires direct light activation of the PS, tumors that are inaccessible to light, such as metastases in bone, brain, or deeply located organs, remain challenging to treat. In addition to light penetration issues, the uneven distribution of PSs within tumors is another limiting factor in treating metastasis. Tumor regions that are distant from blood vessels often receive inadequate PS concentrations due to poor vascularization, making them less responsive to PDT. Similarly, areas of the tumor with low oxygen levels, known as hypoxic zones, are problematic as molecular oxygen is necessary for generating ROS. Hypoxia is particularly common in rapidly growing tumors, where the demand for oxygen exceeds supply. These factors, along with the need for localized light exposure, limit PDT's

ability to achieve complete tumor eradication, particularly in widespread or more aggressive metastatic tumors. Combining PDT with other therapies, like immune modulators, may address its limitations, potentially improving outcomes for patients with metastatic cancers. The choice of the light source also plays a critical role in ensuring effective treatment. Light penetration into tissues depends on its wavelength and tissue optical properties like scattering, absorption, and reflection. Red to near-infrared light (600–1200 nm) penetrates tissues more deeply than shorter wavelengths because of reduced absorption by tissue chromophores like hemoglobin and melanin, and lower scattering. However, the ideal therapeutic window for PDT is restricted between 650 and 800 nm. Shorter wavelengths are absorbed more strongly, limiting their penetration to superficial tissues, while longer wavelengths do not provide sufficient energy (above 95 kJ/mol) to activate the PS and generate singlet oxygen. Clinically, lasers and light-emitting diodes (LEDs) are commonly used as light sources. Depending on tumor location, light can be delivered externally or through optical fibers inserted directly into the tumor. For deeper-seated tumors, light in the 600–900 nm range is preferred, as it provides the best balance between tissue absorption and scattering, allowing for the treatment of internal cancers without invasive surgery. Recent advances in PS design and delivery strategies have extended PDT's therapeutic potential. Second- and third-generation PSs, with improved tissue penetration and reduced side effects, combined with targeted delivery systems like immunoconjugates, offer more precise treatment options[21]. These innovations are enabling PDT to address previously untreatable conditions and further solidifying its role in modern therapeutic approaches.

Beyond oncology, PDT has been successfully applied for inactivating microorganisms and viruses, in a procedure known as photodynamic inactivation. The photosensitized reactions that generate ROS can effectively destroy pathogenic bacteria[22], viruses[23], and fungi[24], making photodynamic inactivation a promising alternative to traditional antimicrobial and antiviral treatments, particularly in the face of rising antibiotic resistance. Some interesting non-clinical applications include disinfection of surfaces and packaging, decontamination of fresh produce and water, wastewater treatment, sterilization of equipment, and several other uses in fields such as agriculture, food safety, environmental conservation, air purification, and cultural heritage preservation[25].

2.1 Photophysics of Organic Compounds in Solution

Molecular orbital theory provides a theoretical framework for understanding the electronic structure of molecules, which is strictly dependent on the relative energies and occupancy of molecular orbitals. Optical transitions occur when electrons move between molecular orbitals, either through absorption (from lower- to higher-energy orbitals) or emission (from higher- to lower-energy orbitals) of light. Absorption is an instantaneous event that occurs on a femtosecond timescale. According to the Franck-Condon principle, only electrons can rearrange during this time lapse while the nuclear configuration

remains unchanged. Typically, the highest occupied molecular orbital (HOMO) and the lowest unoccupied molecular orbital (LUMO) are involved, with the HOMO-LUMO energy gap corresponding to the minimum energy an electron must absorb to cross the $S_0 \rightarrow S_n$ energy barrier and be promoted to an excited state through a "vertical transition".

Optical transitions are governed by selection rules, which dictate the probability of a transition based on symmetry considerations and conservation principles. For a transition to be allowed: (i) the symmetry of the initial and final states must be preserved; (ii) there must be a non-zero change in angular momentum (*angular momentum conservation*); (iii) the initial and final states must have different parities; and (iv) the total spin angular momentum of the system must remain constant (*spin conservation*). Hence, transitions that preserve both spatial symmetry and spin configuration are more likely to occur[26]. In addition to these selection rules, the Pauli's exclusion principle and Hund's rules provide further constraints on electronic transitions within molecules. Pauli's principle asserts that no two electrons in an atom can occupy the same quantum state simultaneously, while Hund's rules state that, for a given electronic configuration, the electronic state with maximum spin multiplicity (i.e., the maximum number of unpaired electrons) will have the lowest energy. Nonetheless, in real systems a number of factors lead to violations of selection rules, allowing otherwise forbidden transitions to take place.

Commonly, a Jablonski diagram is used to illustrate photophysical processes that occur after a molecule has been photoexcited (Figure 2.1). This energy diagram, named after the Polish physicist Aleksander

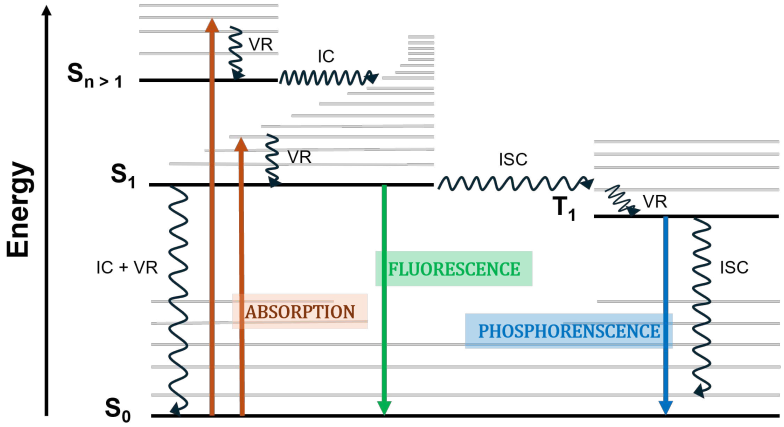

Figure 2.1: Jablonski diagram for a molecule in solution. Radiative (fluorescence, phosphorescence) and non-radiative (VR, IC, ISC) transitions are shown as straight or curved arrows, respectively. Singlet (S) or triplet (T) spin multiplicity of each electronic state is specified. Adapted from Edinburgh Instruments Ltd[27].

Jabłoński, displays the energy levels (S_n, T_n) and their associated vibrational states as horizontal lines, with arrows indicating radiative (straight) or non-radiative (curved) transitions allowed between them. In most cases, organic compounds are singlet in their ground state, with an even number of paired electrons and a spin multiplicity of 1. A well-known exception is molecular oxygen, which has a spin multiplicity of 3 in its ground state. The peculiar photophysics of this molecule will be discussed in detail in Section 2.2.

For a generic molecule, when a photon is absorbed upon excitation, an electron is promoted to an excited state with higher energy and the same spin multiplicity. The energy gap between the initial and final electronic states (e.g., between S_0 and S_1 or between S_0 and S_2) must correspond to the energy of the photon, given by the Planck-Einstein relation:

$$E = h\nu = \frac{hc}{\lambda} \tag{2.1}$$

where E is the energy of the photon, h is the Planck's constant (6.63×10^{-34} Js), ν and λ are the frequency and wavelength of the electromagnetic radiation, respectively, and c is the speed of light in vacuum (2.98×10^{8} m/s). According to Kasha's rule, the molecule must relax to S_1 before returning to its ground state whether a $S_{n>1}$ state has been initially populated[28]. In solution, excess energy is quickly dissipated right after absorption through internal conversion (IC), where the molecule transitions between iso-energetic states of the same multiplicity, followed by vibrational relaxation (VR) where the molecule loses energy as heat within the same electronic state by relaxing to its lowest vibrational level. From S_1, the ground state can be recovered directly through the emission of a photon (fluorescence) or indirectly by populating a triplet state via intersystem crossing (ISC). The lifetime of the first excited singlet state, τ_S, and the corresponding decay rate, k_S, are defined as:

$$\tau_S = \frac{1}{k_S} = \frac{1}{k_{fl} + k_{ic}^S + k_{isc}^S} \tag{2.2}$$

where k_{fl}, k_{ic}^S, and k_{isc}^S are the kinetic rates for fluorescence, internal conversion and intersystem crossing, respectively. In solution, VR is so rapid ($k \sim 10^{10}$-10^{12} s^{-1}) that it outcompetes all other relaxation pathways and determines the loss of some excitation energy in the form of kinetic energy. This results in a red-shift in the fluorescence emission spectrum, known as the Stokes shift. The rate of IC depends on the energy difference between orbitals. Specifically, the process is faster the lower is the energy gap, which means IC can rapidly proceed ($k \sim 10^{9}$-10^{11} s^{-1}) between singlet excited states with $n \geqslant 1$, as they are closely energy spaced. In contrast, the transition $S_1 \rightarrow S_0$ is slower due to the large energy gap, allowing IC to compete with fluorescence and ISC relaxation pathways. However, transitions between states of different multiplicity are forbidden in quantum mechanics due to spin inversion, since this violate the conservation of the total angular momentum. By reason of that, ISC is weakly allowed aside from specific molecules, like PSs, that have overlapping vibrational levels of S_1 and T_1. In this case, the electron spin motion is coupled to its orbital motion, determining simultaneous changes in both spin and orbital angular momentum, in order to preserve the total angular momentum of the molecule. This process, described by El-Sayed's rule, is known as *spin-orbit coupling* and notably increases the probability of singlet $\rightarrow$ triplet transitions[29]. Similarly, the transition $T_0 \rightarrow S_0$, which requires an additional spin flip, is slow and can occur via non-radiative ISC (k_{isc}^T = 10^{-2}-10^{4} s^{-1}) or by emitting light as phosphorescence (k_{ph} = 10^{-2}-10^{2} s^{-1}). As a result, the triplet state is generally long-lived, with lifetimes ranging from microseconds to hours, compared to the first excited singlet

state, whose lifetime is typically on the order of nanoseconds. The lifetime τ_T and the decay rate k_T of the triplet state are defined as follow:

$$\tau_T = \frac{1}{k_T} = \frac{1}{k_{ph} + k_{isc}^T} \tag{2.3}$$

It is important to note that in solution the lifetimes of singlet and triplet states, as well as the quantum yields of radiative processes, are considerably affected by the local environment, particularly by solvent polarity and solute-solvent interactions. In fluid solvents at room temperature, general solvent effects can be overlooked only during absorption, as solvent relaxation occurs on a slower timescale (10-100 ps)[30]. Moreover, quenchers such as oxygen, amines, and halogens can further reduce fluorescence intensity and triplet state lifetime.

For clarity, the typical timescales of photophysical process are summarized in Table 2.1.

Characteristic timescales	
Absorption	10^{-15} s
Vibrational relaxation	10^{-12} - 10^{-10} s
Internal conversion	10^{-11} - 10^{-9} s
Fluorescence	10^{-10} - 10^{-7} s
Intersystem crossing	10^{-10} - 10^{-8} s for $S_1 \rightarrow T_1$ 10^{-4} - 10^{2} s for $T_1 \rightarrow S_0$
Phosphorescence	10^{-6} - 1 s

Table 2.1: Charactheristic timescales of the principal photophysical processes. The timescale of a process deeply influences its probability to occur, with spin-forbidden transitions being slower and therefore less probable. Optical selection rules favor allowed transitions over slower spin-forbidden processes.

2.2 Photophysics of Oxygen in Solution

Molecular oxygen plays a key role in several photobiological processes, and its unique electronic configuration lends it distinctive properties regarding its magnetic, spectroscopic and chemical behaviour. Unlike most natural compounds, molecular oxygen in its ground state, $O_2(X^3\sum_g^-)$ or $^3O_2$, exists as a spin triplet, with two unpaired electrons occupying anti-bonding π_x^* and π_y^* orbitals, in accordance with Hund's law. The two lowest-energy excited states, $O_2(a^1\Delta_g)$ and $O_2(b^1\sum_g^+)$, have singlet multiplicity and lie approximately 95 kJ/mol and 158 kJ/mol above the triplet ground state, respectively. The electronic configurations of these three states differ only in how two electrons are distributed between the degenerate π-antibonding orbitals (Figure 2.2), resulting in a different behaviour of the molecule when reacting with other species.

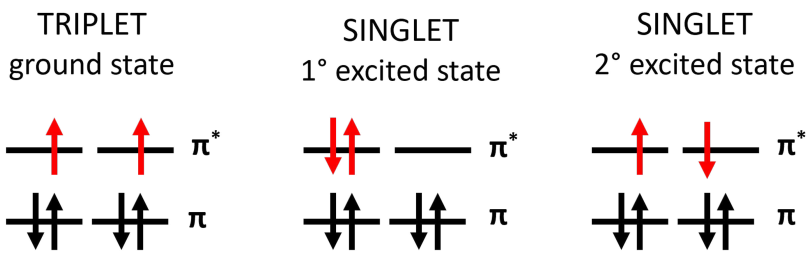

Figure 2.2: Electronic configuration of molecular oxygen.

As mentioned, oxygen in the ground state has an open-shell configuration, which gives rise to its paramagnetic nature. However, despite being a diradical triplet, $O_2(X^3\sum_g^-)$ is remarkably stable, owing to a large resonance stabilization energy of about 100 kcal/mol. This stabilization significantly increases the energy barrier for reactions, thereby preventing $O_2(X^3\sum_g^-)$ from hydrogen atom abstraction and autoxidation reactions[31]. In contrast, the first excited state $O_2(a^1\Delta_g)$, commonly referred to as singlet oxygen or $^1O_2$, is a highly-reactive metastable species that is doubly degenerate on the basis of orbital symmetry. Since the $O_2(a^1\Delta_g) \rightarrow O_2(X^3\sum_g^-)$ transition is spin forbidden, singlet oxygen is relatively long-lived, with a characteristic lifetime that is solvent-dependent, ranging from 3-4 μs in aqueous solution up to 64-65 minutes in the gas-phase[32,33]. Then, this molecule is stable enough to react with a variety of cellular components (discussed in more detail in later Section 2.2.3 on singlet oxygen interactions with biological systems). Despite its higher energy, $O_2(b^1\sum_g^+)$ is short-lived, existing only on the picosecond timescale in solution-phase systems[33]. In fact, the non-radiative $O_2(b^1\sum_g^+) \rightarrow O_2(a^1\Delta_g)$ relaxation prevails over the phosphorescence emission at 765 nm (associated to the $O_2(b^1\sum_g^+) \rightarrow O_2(X^3\sum_g^-)$ transition), as the angular momentum is conserved. As of now, $O_2(b^1\sum_g^+)$ is not known to react with other molecules in solution.

2.2.1 Production and Detection of Singlet Oxygen in Solution

The highly reactive and short-lived nature of singlet oxygen, henceforth referred to as $^1O_2$, makes its direct detection challenging. The most ubiquitous test for revealing the presence of $^1O_2$ in solution is the direct observation of its phosphorescence emission at 1270 nm in time-resolved photon counting experiments. Despite being very week, this signal has been detected in various biological systems, including single cells and tissues[34,35]. Alternatively, chemical probes can be used to indirectly detect $^1O_2$. Singlet oxygen sensor green (SOSG), a highly sensitive fluorescent probe, interacts with $^1O_2$ to produce a detectable fluorescence signal[36]. While highly sensitive, SOSG may suffer interference from other ROS. Electron paramagnetic resonance spectroscopy, combined with spin-trap reagents, offers a more specific detection method by forming stable radicals upon reaction with $^1O_2$, although this technique requires more complex instrumentation[37].

$^1O_2$ can be generated through a variety of mechanisms, including chemical reactions and gaseous discharge[38–41]. However, the most efficient and widely used method for $^1O_2$ production is photo-

sensitization, a bimolecular energy transfer process between a photoexcited PS and ground-state molecular oxygen ($^3O_2$). As already discussed, when irradiated with light at a wavelength matching its

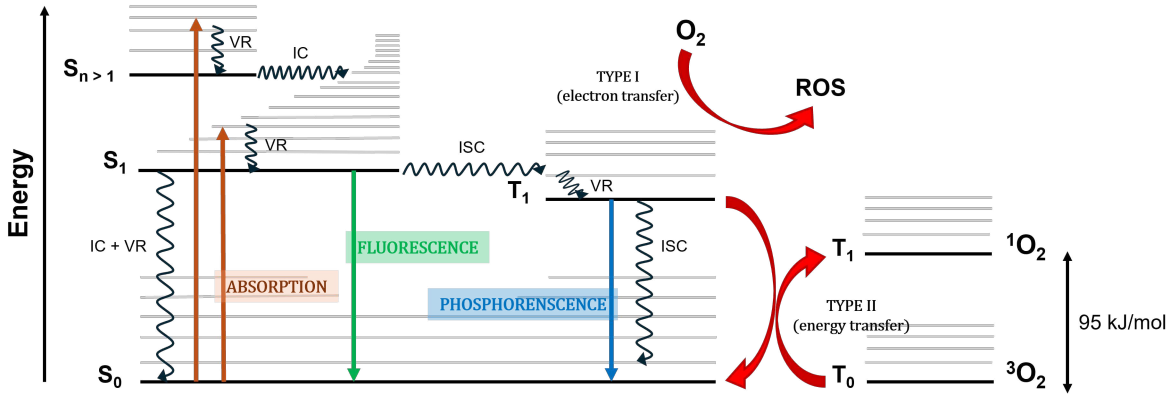

Figure 2.3: Modified Jablonski diagram for O_2 photosensitization.

absorption band, the PS is promoted from its ground state to an excited singlet state (S_n). Following rapid VR to S_1, it may undergo ISC to its triplet state (T_1) with a different spin multiplicity. The probability of populating the triplet state is described by the quantum yield of triplet state formation, Φ_T, representing the fraction of absorbed photons that lead to triplet state formation. The reaction between the PS in T_1 and $^3O_2$ is spin-allowed and can proceed through two distinct photosensitized reactions of Type I and Type II, both resulting in the generation of reactive species.

In a Type I reaction, the PS in its triplet state is engaged in electron transfer processes. Initially, the PS is oxidized by a substrate (commonly a biomolecule), resulting in the formation of the PS radical cation ($PS^{+\cdot}$). Molecular oxygen can subsequently undergo electron transfer with this PS radical, forming the superoxide anion radical ($O_2^{-\cdot}$). This reactive species can either act as an oxidizing agent, subsequently being converted into hydrogen peroxide (H_2O_2) via the enzymatic activity of superoxide dismutase, or it can act as a reducing agent, reverting to $^3O_2$ [42]. H_2O_2, in turn, may be reduced to generate the highly reactive hydroxyl radical ($HO^{\cdot}$), which is responsible for significant oxidative damage to biological structures. The products generated through Type I photosensitized reactions are collectively termed reactive oxygen species (ROS). Alternatively, whether the energy absorbed by the PS exceeds 158 kJ/mol, a Type II reaction can take place. This involves direct energy transfer from the PS in triplet state to $^3O_2$, and leads to the formation of singlet oxygen, primarily in its $O_2(a^1\Delta_g)$ state. This process, also known as *Dexter energy transfer*, is spin-allowed and requires collision between the excited PS and ground-state oxygen, for the simultaneous exchanging of two electrons without a net charge transfer. Even though the other singlet oxygen state, $O_2(b^1\Sigma_g^+)$, is also populated, it rapidly relaxes to $O_2(a^1\Delta_g)$ with near-perfect efficiency [43]. Thus, $^1O_2$ is considered the final product of the Type II process.

Considering that O_2-induced quenching of the PS's triplet state competes kinetically with the monomolecular radiative and non-radiative deactivation processes (i.e., phosphorescence and ISC), the

equation 2.3 expressing the lifetime of the triplet state becomes:

$$\tau_T = \frac{1}{k_T} = \frac{1}{k_{ph} + k_{ISC}^T + k_q[O_2]} \tag{2.4}$$

Here, k_q is the quenching rate constant, whose value is diffusion-limited and typically on the order of 10^9-10^{10} $M^{-1}s^{-1}$.

Another critical parameter to quantitatively measure the efficiency of the process is the quantum yield of singlet oxygen generation, Φ_Δ, defined as the ratio of the number of singlet oxygen molecules generated to the number of photons absorbed by the PS. It depends on the quantum yield of triplet state formation, Φ_T, and can be calculated as[44]:

$$\Phi_\Delta = \Phi_T S_\Delta S_q \tag{2.5}$$

where $S_\Delta = \frac{k_{et}}{k_q}$ represents the fraction of molecules in the triplet state quenched by oxygen that leads to $^1O_2$ generation, and $S_q = k_q \frac{[O_2]}{k_q O_2 + k_T}$ reflects the efficiency of O_2-induced quenching considering all possible de-excitation pathways of the triplet state. In most air-equilibrated solutions and in the absence of other quenchers, the kinetic is governed by bimolecular quenching[43]. Under these conditions:

$$k_{ph} + k_{ISC}^T \ll k_q[O_2] \tag{2.6}$$

This implies that $S_q \approx 1$, allowing the simplification of the quantum yield of singlet oxygen as follows[44]:

$$\Phi_\Delta = \Phi_T S_\Delta \tag{2.7}$$

Once $^1O_2$ is generated, its decay follows a typical exponential pattern with a characteristic lifetime τ_Δ. Both energy transfer (Type II) and electron transfer (Type I) reactions are possible during PDT. It is generally accepted that most PSs can generate both $^1O_2$ and ROS, but the rate of $^1O_2$ production (Type II) is typically much higher than that of radical formation (Type I), often by two orders of magnitude ($k \approx 1\text{-}3\times10^9$ mol^{-1} s^{-1} for Type II vs. $k \leqslant 1\times10^7$ mol^{-1} s^{-1} for Type I). Therefore, energy transfer processes (Type II) generally dominate in PDT, with $^1O_2$ being the primary reactive species driving therapeutic outcomes[45].

2.2.2 Lifetime and Diffusion of Singlet Oxygen

A comprehensive understanding of $^1O_2$ diffusion and its interaction within cells has profound implications for the design and optimization of effective PDT and other photosensitization-based treatments. The diffusion of $^1O_2$ in cellular environments is a complex phenomenon, heavily influenced by the crowded and heterogeneous nature of the intracellular milieu. Factors such as the viscosity of the cytoplasm, the presence of organelles and membranes, as well as local concentrations of quenchers and antioxidants, all impact the mobility and lifetime of this reactive species.

Once generated in solution, $^1O_2$ can diffuse over a certain distance *d*, determined by its lifetime τ_Δ, and diffusion coefficient *D*. This relationship is governed by the equation:

$$d = \sqrt{6tD} \tag{2.8}$$

Since τ_Δ represents the time required for $^1O_2$ concentration to decrease by a factor of 1/e, it is reasonable to assume that the concentration of $^1O_2$ decays to zero at t = $5\tau_\Delta$ [46].

Early attempts to measure τ_Δ in biological systems relied on monitoring its characteristic near-infrared luminescence at around 1270 nm, which is proportional to its lifetime[35]. These early studies estimated $^1O_2$ lifetime to be approximately 10-300 ns[47,48], limiting its diffusion distance to ~10-20 nm when using the diffusion coefficient for oxygen in water (D = 1.4×10^{-5} cm^2s^{-1}). Considering that $^1O_2$ in pure water has a lifetime of ~3.5 μs[32], the authors hypothesized that endogenous quenchers, such as proteins, dramatically reduce its lifetime in intracellular environments. More recent studies, however, have reported a longer lifetime of ~3 μs within cells for $^1O_2$, with an intracellular diffusion coefficient of D = 2-4×10^{-6} cm^2s^{-1}, lower than in water[34,46,49]. Based on these data, the diffusion distance of $^1O_2$ extends up to ~200 nm. However, it is still quite short compared to the typical size of eukaryotic cells, which ranges from 10 to 100 micrometers in diameter. Consequently, the effects of $^1O_2$ are highly localized within cells, and its cytotoxic action depends critically on the spatial positioning of the PS during PDT. This underscores the importance of targeted delivery strategies in PDT to ensure effective treatment outcomes by directing the PS to tumor sites or specific intracellular regions.

2.2.3 Singlet Oxygen Reactions with Biological Molecules

$^1O_2$ is widely recognized as the primary cytotoxic agent generated during PDT. Originating from the excitation of ground-state oxygen to a higher-energy singlet state, it initiates a cascade of oxidative reactions with biological molecules, which are pivotal in mediating the therapeutic effects of PDT. Understanding these interactions is essential not only for optimizing PDT but also for elucidating the broader mechanisms of oxidative stress, cellular signaling, and disease pathogenesis.

Reactions with Biological Molecules

$^1O_2$ preferentially reacts with electron-rich biomolecules such as lipids, nucleic acids, and proteins. In cell membranes, $^1O_2$ induces lipid peroxidation, particularly targeting unsaturated lipids. This process leads to the formation of lipid hydroperoxides and other reactive lipid species, compromising membrane integrity and triggering cell death pathways[50]. Among nucleobases, guanine is the most reactive toward $^1O_2$ due to its low ionization potential[51]. Oxidation of guanine results in various forms of DNA damage, including mutations and strand breaks, which compromise genetic integrity and can lead to mutagenesis, carcinogenesis, and ultimately cell death. Proteins are also highly susceptible to $^1O_2$-induced oxidative damage, particularly at residues containing sulfur (e.g., methionine, cysteine)

and those with unsaturated structures (e.g., tryptophan, tyrosine, histidine). These amino acids are efficient scavengers of $^1O_2$ through chemical quenching ($k > 10^7\ M^{-1}s^{-1}$)[45], with the exception of tryptophan for which also physical quenching is not negligible[52]. Interestingly, recent studies indicated that the reactivity of amino acids is influenced not only by their location within the protein and their accessibility, but also by the protein's local environment[53,54]. Oxidative modifications can alter proteins' structure and function, potentially leading to cellular dysfunction or death.

Cells selectively remove $^1O_2$ by either physical or chemical quenching, mitigating its cytotoxic effects and ensure cellular survival[44]. Physical quenching involves the non-reactive collisional deactivation of $^1O_2$ excited state through interactions with surrounding molecules, transferring energy to the quenching molecule without forming new chemical bonds or consuming oxygen. In contrast, chemical quenching results in the irreversible deactivation of $^1O_2$, forming stable chemical products. Clearly, efficient scavenging of $^1O_2$ by biomolecules results in a shortening of its lifetime and sphere of action. Therefore, PDT protocols must be optimized so that $^1O_2$ remains sufficiently reactive to induce cytotoxic effects in targeted cells, despite being subject to quenching mechanisms.

Effects on Tumors

As previously discussed, the production of ROS species through photosensitization can result in significant cellular damage and death, as these species react with various biological targets, including lipids, proteins, and DNA. The efficiency of ROS-induced cytotoxicity in a biological system, however, is primarily determined by the limited diffusion range of $^1O_2$, which restricts its sphere of activity to less than 200 nm. Consequently, the precise localization of the PS within or near target cells is a critical determinant of the therapeutic effectiveness. The oxidative damage triggered by $^1O_2$ in PDT leads to a multifaceted response in cancer cells, primarily through direct cytotoxicity, vascular shutdown, and immune modulation (Figure 2.4). It has become evident that the induction of all three mechanisms is essential for achieving long-term tumor regression[18].

PDT induces various forms of cell death, including necrosis, apoptosis, autophagy, and other non-conventional pathways[55,56]. Experimental evidence suggests that the initial site of photodamage is crucial in determining the specific modality of cell death triggered by light. For instance, necrosis is often associated with high concentrations of the PS or high light doses, leading to a rapid and uncontrolled cell death characterized by loss of membrane integrity and cell lysis. This can cause inflammation due to the release of intracellular contents into the tumor microenvironment (TME). Apoptosis, in contrast, is a controlled, multi-step form of programmed death encoded in every cell. It can be triggered by the activation of cell surface death receptors or the release of cytochrome c following mitochondrial photodamage[57]. This process is often the preferred outcome in PDT because it minimizes widespread inflammation and avoid rapid oxygen depletion, which is a common concern associated with necrosis[25]. To promote apoptosis, lower light fluence rates are generally preferred,

as they are less likely to induce necrotic cell death, thereby ensuring a more controlled therapeutic outcome[13]. Beyond necrosis and apoptosis, PDT can also induce autophagy, a process in which cells degrade their own components to survive under stress. Depending on the context, autophagy can lead to either cell survival or cell death[58]. Additionally, PDT has been shown to impair the endoplasmic reticulum, potentially triggering paraptosis[59], and can disrupt the cytoskeleton, leading to anoikis in response to loss of cellular adhesion[60]. The balance between these outcomes is influenced by the extent of photodamage and the cell's capacity to detoxify reactive intermediates produced by the PS or to repair the resulting damage.

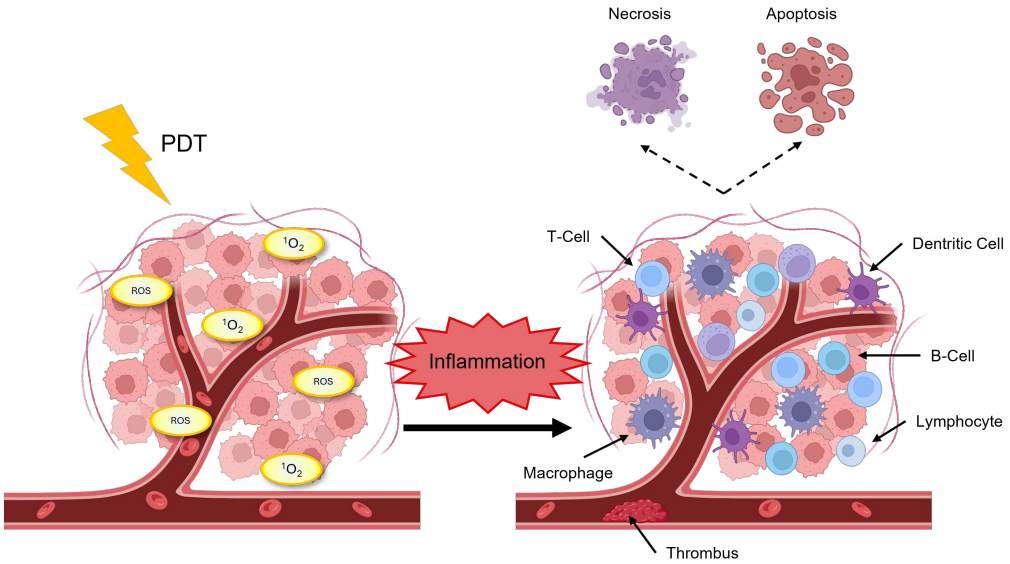

Figure 2.4: Different effects of PDT on tumor cells, combining direct cell death, immune activation, and vascular disruption. Targeted light activation of a PS within tumor cells generates ROS and $^1O_2$, causing direct cytotoxic effects such as necrosis and apoptosis. This cell damage triggers an inflammatory response that recruits and activates immune cells, including T-cells, B-cells, lymphocytes, macrophages, and dendritic cells, to infiltrate the tumor site, potentially enhancing the anti-tumor immune response and improving long-term therapeutic outcomes. Additionally, damages of blood vessels feeding the tumor may limit nutrient supply and contribute to further tumor regression. Created in Biorender.com.

In addition to directly inducing cell death, PDT can disrupt the blood vessels supplying the tumor, depriving cancer cells of oxygen and nutrients. This vascular shutdown results in tumor necrosis and creates a hostile environment that may impair tumor growth, potentially increasing susceptibility to subsequent treatments and achieving long-term tumor control[61]. Reducing the drug-to-light period can be a sound strategy to enhance this effect.[25]. However, the consumption of oxygen to generate ROS can exacerbate hypoxic conditions within the TME, potentially limiting the overall effectiveness of the treatment. Interestingly, PDT-induced cell death can also stimulate the immune system. When tumor cells die, they release damage-associated molecular patterns, which can enhance the recruitment and activation of immune cells, such as dendritic cells, macrophages, and T-cells, within the TME[56]. This immune response is particularly significant in immunogenic cell death, where pro-inflammatory cytokines and tumor antigens are released, promoting a robust anti-tumor immune response.

2.3 Photosensitizers

Since their discovery nearly a century ago, significant effort has been dedicated to the development of increasingly efficient PSs for both preclinical and clinical applications. The National Cancer Institute (2024) defines a PS as "*a drug used in photodynamic therapy that becomes active and kills the cancer cells when absorbed by cancer cells and exposed to light*"[62]. Photochemical and photophysical alteration of biological structures are achieved through photosensitization in the presence of oxygen (see Section 2.2.3); hence, high quantum yields of triplet state formation and singlet oxygen generation are in general desirable properties for a PS. For maximal therapeutic efficacy, an ideal PS should possess other relevant features[21,63,64]. A high absorption coefficient in the therapeutic window (650–800 nm) is particularly important, as light penetrates tissues more deeply at these wavelengths but yet retains enough energy to generate $^1O_2$. Conversely, minimal absorption in the 400–600 nm range is preferred to avoid photosensitization of superficial tissues such as skin. The PS should also exhibit low dark toxicity to prevent off-target effects before light activation and demonstrate minimal photobleaching to sustain efficacy during the treatment. Likewise, selective accumulation in malignant tissues and rapid clearance from normal tissues are highly desirable to minimize long-term side effects. Photostability is particularly important not only to minimize the dose of PS required to obtain the desired photodynamic effect, but also to prevent the formation of secondary oxidative products with unknown behaviour[21]. Additionally, for high reproducibility, the PS should be chemically pure and water-soluble for intravenous administration. The primary limitation of most PSs is their poor hydrophilicity, which is particularly problematic in clinical practice, as it leads to aggregation in the bloodstream[20]. This necessitates the use of carriers, as liposomes, nanoparticles, or hydrogels, to enhance PSs solubility and stability in aqueous solution, and facilitate their deliver to tumor tissues[13].

2.3.1 Classification

PSs are generally classified into three generations, reflecting their temporal and functional development[21,64]. First-generation PSs, such as Photofrin® and hematoporphyrin derivatives, were introduced in the mid-1990s and were the earliest to receive the FDA approval for cancer treatment. However, they had significant limitations, including prolonged skin photosensitivity (lasting up to two months post-treatment), poor water solubility, low purity, and susceptibility to photobleaching. These drawbacks led to the development of second-generation PSs, primarily synthetic derivatives of chlorins (Foscan®), bacteriochlorins, phthalocyanines, verteporfin (Visudyne®), hypericin, xanthenes (rose bengal), phenothiazines (methylene blue), and protoporhyrin IX precursor (Hexvix®, Metvix®, Levulan®)[4]. Despite improved photophysical properties and tissue penetration, their limited tumor selectivity motivated the creation of third-generation PSs, which aim for increased specificity through conjugation of well-known PSs with targeting-moietis (e.g., proteins, antibodies, carbohydrates, and liposomes) or

their encapsulation into carriers (e.g., nanoparticles or quantum dots)[21].

Although these advancements have broadened PDT's applications, it is essential to note that not all newer-generation PSs outperform their predecessors in every clinical setting. Therefore, many experts prefer to classify PSs based on their chemical structure rather than generation, broadly dividing them into porphyrin-based and nonporphyrin-based categories[65–67]. Porphyrin-derived PSs include compounds with a tetrapyrrole macrocycle structure, often incorporating a central metal atom. First-generation PSs and most second-generation ones fall into this category. Porfimer sodium (Photofrin®) and chlorin e6 are prime examples, with the latter attracting interest for its superior properties in cancer therapy[68]. Conversely, nonporphyrin-based PSs encompass synthetic dyes and natural PSs lacking the tetrapyrrole ring structure but capable of generating ROS upon light exposure. These compounds can have different chemical structures and properties, and overcome some limitations of porphyrins, particularly in terms of tissue selectivity and activation wavelengths. The strongest absorption band of porphyrins is found in the ultraviolet to blue region (around 400–450 nm), known as the Soret band. However, light penetration at these wavelengths is limited to 1–2 mm due to high absorption by tissue chromophores and scattering. The weaker absorption Q-bands in the visible region (usually > 600 nm) are the ones typically used in PDT treatments, as red-light penetration is deeper, but even in this case, it is limited to 5–10 mm at most. In contrast, nonporphyrin-based PSs are designed to absorb light in the near-infrared region, corresponding to the tissue optical window, which allows for deeper penetration, reaching several centimeters (about 10–15 mm or more), making them more suitable for treating deeper-seated tissues.

Recent developments in metal-organic frameworks (MOFs)[69] and metal-based PSs[70], such as Iridium(III) complexes and ruthenium-based compounds, are leading the charge toward fourth-generation PSs. These compounds show great promise for their enhanced photophysical properties, high singlet oxygen yields, and improved tissue specificity. The most exciting advancements involve the functionalization of PSs to improve tumor selectivity and enhance their photophysical properties. PSs have being engineered to respond to specific biological or physical stimuli, such as pH, temperature, or enzyme presence, allowing localized activation within the TME[13]. Chemical modifications also enhance solubility and stability, while incorporation of PSs into water-soluble host molecules, such as nanoparticles or cyclodextrins, facilitates their bioavailability, prevents aggregation, and allows for controlled release. Notably, these innovations facilitate the development of theranostic agents that serve both as PSs for inducing cell death through the generation of ROS upon light activation and as imaging tools for real-time monitoring of tumor response and treatment efficacy. Boron dipyrromethene (BODIPY) dyes and organic fluorophores, for instance, are valued for their strong fluorescence and photostability, making them ideal candidates for theranostic application[21].

Although many potent PSs have been developed to date, relatively few have demonstrated consistent clinical efficacy and gained regulatory approval[64].

2.3.2 Subcellular Localization

The therapeutic efficacy of PDT heavily depends on the subcellular localization of PSs, as $^1O_2$ has a limited diffusion range of less than 200 nm during its lifetime. Therefore, proximity to vital cellular structures is critical for maximizing the cytotoxic effects of PDT[18]. PSs that localize in mitochondria or the endoplasmic reticulum are more likely to induce apoptosis, a controlled form of cell death that minimizes inflammation and tissue damage. In contrast, PSs that accumulate in lysosomes or plasma membranes may induce necrosis or necroptosis, potentially triggering immune responses that could complement cancer immunotherapy approaches. Importantly, clinically approved PSs avoid nuclear localization, thereby reducing the risk of DNA damage that might result in carcinogenesis or the emergence of resistant cell populations[19]. Given the short-lived nature and restricted diffusion of ROS, PSs must accumulate in organelles where cellular repair mechanisms are less effective for optimal photodynamic efficacy. Mitochondria and lysosomes, for example, are sites where ROS-mediated damage is often irreversible, leading to cell death with minimal chances for repair. Conversely, PSs that localize in the cytosol or away from vital organelles may allow cells to activate antioxidant responses or DNA repair pathways, potentially reducing PDT effectiveness[21].

The physicochemical properties of PSs, including their charge, size, and hydrophobicity, significantly influence their intracellular trafficking and biodistribution in specific organelles[71]. Targeting strategies can be both passive or active. In solid tumors, the abnormal and leaky vasculature, coupled with impaired lymphatic drainage, allows larger molecules and nanoparticles to accumulate more readily within the tumor tissue than in normal tissues, a phenomenon called enhanced permeability and retention (EPR) effect. This increased permeability is particularly beneficial for delivering PSs deeper in the TME. The net charge of a PS determines its interaction with cellular membranes. Positively charged PSs readily cross the negatively charged cellular membranes and tend to accumulate in mitochondrial membranes, while hydrophobic PSs are more likely to localize in lipid-rich environments such as the plasma membrane or lysosomes. Amphiphilic PSs (particularly important in photochemical internalization, see Chapter 3) are internalized via endocytosis which favours their localisation to the endosomes. The molecular size influences the diffusion, such that larger PS molecules often diffuse more slowly within cells, resulting in preferential localization near their site of entry. However, there is still much uncertainty about how the structural properties and dimensions of PSs influence their localization within cells. Another critical property is lipophilicity, which seems to contribute to the preferential uptake of PSs by tumors and affect their subcellular distribution[71]. Hydrophilic PSs often bind albumin and exploit the EPR effect to accumulate in the interstitial space of the tumor[20]. More hydrophobic PSs, instead, preferentially bind to low-density lipoproteins, often abnormally expressed by cancer cells[18]. Recent advancements in third-generation PSs leverage conjugation to specific targeting moieties to actively direct PSs to specific organelles, enhancing selective distribution within cancer

cells. Suitable carriers include antibodies, peptides, nucleic acids and other high affinity ligands that bind to specific organelle-associated receptors[13].

The TME plays a crucial role in PS localization and efficacy. The hypoxic conditions common in tumors (oxygen concentration less than 1 μM), along with acidic pH and abnormal vasculature, can hinder the effectiveness of Type II PDT mechanisms, which rely on oxygen for ROS generation. In these environments, PSs must be carefully selected to ensure optimal uptake and localization in hypoxic zones, where ROS generation may be impaired. PSs that preferentially accumulate in malignant cells but avoid normal tissues help improve therapeutic selectivity, reduce off-target phototoxicity and increase overall treatment efficacy.

2.4 Photoimmunotherapy for Cancer Treatment

PDT has emerged as a powerful and minimally invasive treatment option for various cancers and non-malignant conditions. Despite its advantages, such as high selectivity, minimal systemic toxicity, and the ability to be repeated without cumulative side effects[19], PDT has certain limitations. These include restricted tissue penetration of light, hypoxic conditions in tumors that reduce ROS generation, and the risk of incomplete eradication of tumor cells, which can lead to recurrence[13]. Traditional cancer treatments, such as chemotherapy and radiotherapy, are effective at targeting rapidly dividing cancer cells but often cause significant side effects due to their lack of selectivity for neoplastic cells over healthy tissue. While potent, these therapies have broad cytotoxic effects that limit the dosage that can be safely administered, often resulting in suboptimal tumor eradication. Tumor recurrence and the development of drug resistance are also frequent challenges, as some cancer cells can survive or adapt to withstand the therapy over time. Consequently, various combinations with other therapies have been explored, including PDT with surgery[72], chemotherapy[73], radiotherapy[74], immunotherapy[4,75], and other novel modalities[76–78], each offering distinct advantages based on the biological mechanisms they target. Both *in vitro* and *in vivo* studies have shown that combining PDT with other therapeutic modalities achieves synergy, resulting in a more potent effect of the treatment compared to administering each therapy individually.

PDT in combination with immunotherapy, commonly referred to as photoimmunotherapy (PIT), is of particular relevance to this thesis. Under normal conditions, the immune system operates through two primary mechanisms, the innate and adaptive immune responses, to defend the host from pathogens such as bacteria, viruses, toxins and also cancer cells[79]. However, tumors have evolved sophisticated strategies to evade immune detection and destruction, a phenomenon known as “immune escape” or “immune evasion”. Accumulating evidence shows that tumors exploit physiological immune pathways as mechanisms to escape immune surveillance and ultimately grow uncontrolled[80].

PIT was first introduced in cancer treatment in the early 1980s, with initial preclinical studies

demonstrating the potential of targeting cancer cells by coupling PSs to monoclonal antibodies[3]. Its clinical relevance quickly emerged due to its ability to precisely target and kill cancer cells with minimal damage to surrounding healthy tissues. Beyond its direct cytotoxic effects, PIT can also modulate the TME, enhancing the immune system's ability to recognize and destroy cancer cells. The induction of immunogenic cell death by PIT releases tumor-associated antigens, potentially activating an adaptive immune response and fostering long-term immune surveillance, thereby reducing the risk of recurrence[75]. Monoclonal antibodies are the most widely used targeting agents in PIT due to their high specificity for tumor-associated antigens[4]. Researchers engineered these antibodies to recognize and bind to specific proteins overexpressed on cancer cells surfaces and, when conjugated to a PS, allow specific targeting followed by light-activated localized destruction. Several approved antibodies have been widely exploited to create effective photoimmunoconjugates targeting relevant membrane receptors, including EGFR (cetuximab, panitumumab), HER2 (trastuzumab, pertuzumab), PSMA (J591), CD20 (rituximab), and MUC1 (HuHMFG1)[4,81]. These antibodies are typically conjugated to IRDye 700DX (IR700) or chlorin e6, although the use of different PSs has also been reported. One of the most successful applications of PIT is the cetuximab-IR700 conjugate, which has demonstrated high efficacy in preclinical models, particularly in head and neck cancers where EGFR is overexpressed. This conjugate is currently in clinical trials where has shown promising results in targeting EGFR-positive tumors[82,83]. HER2-targeted PIT has also been developed using trastuzumab-IR700 conjugates for HER2-positive breast cancers[84].

PIT is also highly synergistic with immune checkpoint inhibitors (ICIs), which block inhibitory pathways that tumors use to suppress the immune system. ICIs are a new class of immune-modulating monoclonal antibodies designed to prevent cancer cells from binding critical checkpoint receptors on T-cells, such as cytotoxic T-lymphocyte antigen 4 (CTLA-4), programmed death receptor 1 (PD-1), and its ligand, programmed death-ligand 1 (PD-L1). Ipilimimab (targeting CTLA-4) was the first FDA-approved ICI for the treatment of advanced melanoma[85]. Currently, three anti-PD-1 antibodies (nivolumab, pembrolizumab, cemiplimab) and three anti-PD-L1 antibodies (atezolizumab, durvalumab, avelumab) have passed the clinical trial phase and are currently used in the clinical practice[86]. These antibodies can be linked to active payloads (e.g., chemotherapeutic drugs, PSs, radionuclides, toxins) to enhance anti-tumor efficacy by simultaneously blocking immune suppression and delivering direct cytotoxic effects to cancer cells[87]. For instance, EGFR- and HER2-targeted PIT combined with ICIs has demonstrated improved tumor control in preclinical studies, even in tumors that initially exhibited resistance to immunotherapy[88,89].

Chapter 3

Photochemical Internalization

Photochemical internalization (PCI) is an advanced drug-delivery technology derived from photodynamic therapy (PDT) principles at the Norwegian Radium Hospital[8]. PCI facilitates the targeted release of therapeutic macromolecules from endolysosomal vesicles directly into the cytosol of cells using a sub-lethal dose of PDT. This method overcomes a significant challenge in drug delivery: many therapeutic agents, such as proteins, nucleic acids, and some chemotherapeutics, are too large or hydrophilic to penetrate the plasma membrane effectively and are typically taken up by cells via endocytosis. However, after internalization, these molecules are often trapped in endosomes and eventually degraded in lysosomes, limiting their therapeutic efficacy. PCI uses light-activated photosensitizers (PSs) to accumulate in endosomal membranes and selectively disrupt them, allowing the release of entrapped molecules into the cytosol where they can reach their intracellular targets. Unlike conventional PDT, which directly kills cells through the production of reactive oxygen species (ROS), PCI focuses on releasing therapeutic agents into the cytosol without causing widespread cell death. Accordingly, in PCI the cytotoxic activity primarily arises from the therapeutic agent itself rather than from photochemical reactions. Nevertheless, PCI efficacy depends on PS characteristics, such as localization within intracellular compartments and specific photophysical properties. Among all types of available PSs, amphiphilic compounds are ideal for PCI due to their preferential localization in lipid-rich endosomal and lysosomal membranes enclosing the therapeutics. Additionally, they partially intercalate into the plasma membrane, positioning them for effective photoactivation.

One of the main advantages of PCI is its ability to achieve selective endosomal escape through controlled photoactivation of PSs. Therapeutic release only occurs in the areas exposed to light, typically confined to the treatment region, which minimizes systemic side effects and reduces off-target damage to surrounding healthy tissues. To date, PCI has prove to enhance the cytotoxic activity of numerous macromolecules in over 80 cancer cell lines and various animal models[90]. Notable examples include immunotoxins, chemotherapeutics, nucleic acids for gene delivery, synthetic proteins and peptides for cancer vaccination, and oligo- and polynucleotides[91].

PCI can also be applied to smaller molecules (i.e., with molecular weight < 900 Daltons), provided that they accumulate within endocytic vesicles, expanding its utility beyond macromolecular therapeutics. This flexibility opens new possibilities for PCI to enhance the efficacy of a wide range of therapeutic agents, from large biomolecules to small-molecule drugs.

3.1 Mechanism of Action: Principles of PCI

Many therapeutics struggle to penetrate cell membranes on their own due to their size, charge, or molecular nature. Cells typically internalize these agents via endocytosis, forming vesicles, called endosomes, that transport substances within the cell[92]. Without a mechanism to escape, these therapeutic agents remain trapped inside endosomes, which eventually fuse with lysosomes where their contents are degraded by lysosomal enzymes. For these therapies to be effective, they must either penetrate the plasma membrane or escape from endolysosomes into the cytosol to interact with their intended molecular targets. PCI technology provides a controlled release of therapeutics trapped in endocytic vesicles of neoplastic cells by using amphiphilic PSs and confined intracellular PDT. The conventional “light-after" PCI approach involves the co-administration of the therapeutic agent and the PS, prior to light exposure. After a sufficient incubation period (long enough for both the PS and therapeutic drug to localize within the endocytic vesicles, but not so long that degradation of the drug begins), visible light of a specific wavelength matching the PS absorption band is applied. Upon light activation, the PS generates ROS, including $^1O_2$, which having a short lifetime and limited diffusion range, selectively disrupts the lipid bilayers of endosomes and lysosomes. This allows the therapeutic molecules trapped inside to escape into the cytosol, where they can exert their therapeutic effects (Figure 3.1). Alternatively, the therapeutic molecule can be administered during a chase period in PS-free medium to promote detachment of the PSs from the plasma membrane, thereby minimizing accumulation in that area and reducing potential off-target effects. In addition to the conventional “light-after” approach, an alternative strategy known as “light-before" PCI has shown promise in specific scenarios. In this protocol, the application of light precedes the administration of therapeutics by 6-8 hours. Interestingly, this approach has demonstrated greater effectiveness in some *in vitro* studies compared to the conventional “light-after” procedure[90], with its applicability also confirmed *in vivo* by Berg et al.[93]. Although the exact subcellular mechanism is still unclear, it was proposed that photochemically-damaged and undamaged endocytic vesicles may fuse creating new vesicles with permeabilized membranes that facilitate the escape of subsequently internalized therapeutic agents[94]. This strategy may be advantageous when precise timing of drug release is critical to avoid premature degradation of the therapeutics and optimize therapeutic outcomes.

Regardless of the specific PCI strategy adopted, these processes are tightly controlled. Since PSs are only activated by light, PCI provides a highly localized and regulated release of therapeutic agents,

ensuring that drug delivery is confined to specific regions within the body. The short-range action of $^1O_2$ further minimizes off-target effects and reduces damage to surrounding healthy tissues.
Overall, PCI presents a powerful method for enhancing cytosolic concentrations of macromolecular therapeutics, allowing these agents to bypass the degradative pathways of endocytosis and lysosomal degradation. This precise and localized control makes PCI a promising tool for developing more effective treatments in oncology, gene therapy, and other challenging therapeutic applications.

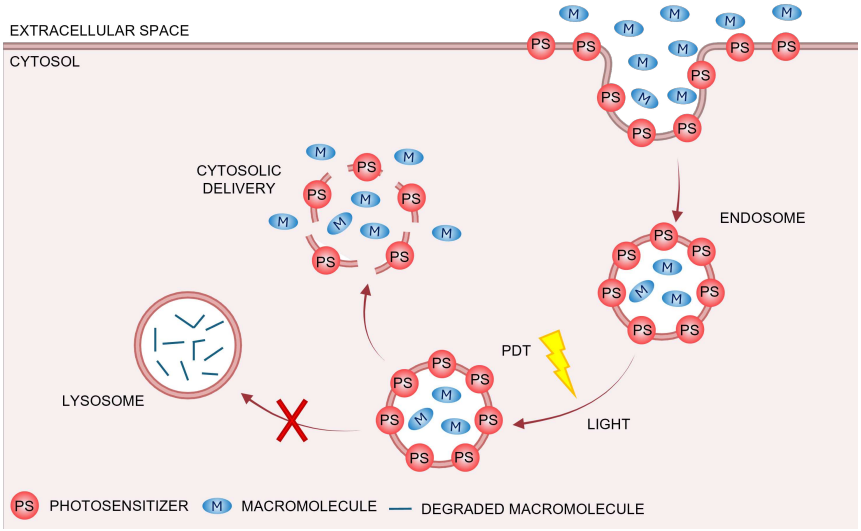

Figure 3.1: Mechanism of action of PCI. Therapeutic macromolecules (e.g., toxins, immunotoxins, or drugs) and PSs are internalized by the cell through endocytosis. The PSs accumulate on the membranes of newly formed endosomes containing the therapeutic macromolecules. Typically, endocytic vesicles fuse with lysosomes, where the cargo is degraded by lysosomal enzymes. Upon light exposure before lysosomal degradation occurs, the PSs generate $^1O_2$ and ROS, disrupting the endosomal membranes and allowing the therapeutic macromolecules to escape into the cytosol, thereby avoiding lysosomal degradation and enhancing their therapeutic efficacy. Created in Biorender.com.

3.2 Uptake of Photosensitizers via Endocytosis

Endocytosis is a fundamental cellular process through which cells internalize extracellular material by engulfing it in membrane-bound vesicles. This process intimately regulates many cellular functions, including nutrient uptake, regulation of signaling pathways, immune response, and the removal of cellular debris[92]. In PCI, endocytosis is particularly important as it serves as the primary pathway for the internalization of both PSs and therapeutic agents. Highly hydrophilic PSs cannot easily cross the hydrophobic plasma membrane and are commonly taken up through pinocytosis, a non-specific and inefficient form of endocytosis where the cell membrane invaginates, trapping extracellular fluid and solutes from the surrounding medium. Once internalized, PSs are located within the endosomal matrix, where they generate ROS upon photo-activation, potentially damaging the therapeutic cargo rather than selectively disrupting the endosomal membrane[91]. However, conjugating PSs to targeting moieties such as antibodies allows them to be internalized via receptor-mediated endocytosis, offering a more selective and efficient uptake mechanism. Amphiphilic PSs are preferred in PCI due to their

effective interaction with lipid bilayers of cell membranes. Their hydrophobic regions (such as non-polar hydrocarbon chains or aromatic rings) anchor within the inner part of lipid membranes, while their hydrophilic portions (composed of polar functional groups) interact with the aqueous extracellular environment and membrane components, stabilizing the PSs. This dual nature facilitates the internalization of PSs through adsorptive endocytosis. Nearby the cell, the hydrophobic domains of the PSs interact with the outer leaflet of the plasma membrane, promoting invagination and vesicle formation. The hydrophilic portions, instead, face the extracellular space and prevent the complete penetration of the PS through the membrane. Consequently, once endosomes are formed, PSs are typically localized in the inner leaflet of these vesicles[91]. This localization is crucial to ensure $^1O_2$ generation within the endosomal membrane, selectively disrupting it with minimal damage to surrounding cellular structures or therapeutic agents that can eventually translocate to the cytosol.

The most commonly used PSs in PCI are three porphyrin-based molecules: $AlPcS_{2a}$ (aluminum phthalocyanine disulfonate), $TPPS_{2a}$ (disulfonated tetraphenyl porphine), and $TPCS_{2a}$ (disulfonated tetraphenyl chlorin). All three compounds have two closely located sulfonate groups in their structure, which confer the necessary hydrophilic properties to create amphiphilic molecules capable of localizing within endocytic vesicles. The phthalocyanine $AlPcS_{2a}$ is water-soluble and exhibits strong absorption in the red to near-infrared region of the spectrum, which enables deeper tissue penetration. For these reasons, it has been traditionally chosen for *in vivo* studies. However, its clinical application is limited by batch-to-batch variability due to the existence of multiple isomers[95]. $TPPS_{2a}$, on the other hand, absorbs in the blue-violet region, making it less effective for treating deeper-seated tumors. To overcome this limitation, $TPCS_{2a}$ was developed for clinical use by the di-imide reduction of $TPPS_{2a}$[95]. This PS is commercially known as fimaporfin, and its clinical formulation is marketed under the name Amphinex® (PCI Biotech AS, Oslo, Norway). In this formulation, fimaporfin is solubilized in a mixture of Tween 80, mannitol, and Tris buffer at a pH of 8.5. $TPCS_{2a}$ has been tested in a variety of both *in vitro* and *in vivo* studies to determine its pharmacokinetics, distribution, and overall effectiveness in treating malignancies when combined to light exposure[91]. Notably, fimaporfin has undergone evaluation in Phase I/II clinical trials. Sultan et al. conducted the first Phase I trial to assess the safety and tolerability of $TPCS_{2a}$-mediated PCI of bleomycin, reporting significant antitumor activity in patients with superficial skin and head and neck tumors of various primary histologies[96]. Following this, a multi-center Phase II study was launched to examine both superficial tumors (similar to those in the Phase I trial) and deeper head and neck cancers requiring interstitial illumination through the insertion of multiple optical fibers into the tumor. However, the study was terminated before completion in June 2015 due to commercial and clinical challenges. Recently, the safety of $TPCS_{2a}$-mediated PCI of gemcitabine was comfirmed in a Phase I/II dose escalation study involving patients with advanced inoperable cholangiocarcinomas[97]. Additionally, a concurrent Phase I dose escalation trial demonstrated that combining PCI with Hiltonol for intradermal vaccination is safe when fimaporfin doses remain below 17.5 μg[98].

3.3 Application of PCI in Cancer Therapy

PCI has shown considerable promise in cancer therapy, particularly in enhancing the delivery of chemotherapeutic agents and immunotoxins that are typically limited by poor intracellular penetration or degradation within endolysosomal compartments. Many chemotherapeutic agents, for instance, exhibit limited efficacy because they become trapped in endosomes and are subsequently degraded in lysosomes after internalization. PCI has successfully enhanced the therapeutic potential of four different chemotherapeutic agents (bleomycin, doxorubicin, mitoxantrone, camptothecin)[90]. Similarly, gemcitabine, a nucleotide analogue commonly used in several cancers, also faces such limitations. Recent studies demonstrated that PCI-mediated delivery of gemcitabine significantly improved its cytotoxicity in patients with unresectable perihilar cholangiocarcinoma, overcoming its typical entrapment in endocytic vesicles[97]. These cases demonstrate how PCI can transform the efficacy of chemotherapeutics that might otherwise have restricted intracellular delivery. In addition to chemotherapeutic drugs, PCI has also been used to enhance the delivery of smaller molecules, including highly potent targeted toxins (free or conjugated immunotoxins)[90]. While these molecules effectively induce apoptosis or inhibit protein synthesis in cancer cells, their therapeutic potential is often hindered by poor cytosolic delivery and endolysosomal entrapment. PCI can overcome these barriers, enhancing the cytosolic release of these toxins and substantially increasing their potency and selectivity for cancer cells. For instance, numerous studies have demonstrated the success of PCI to facilitate the release of type I ribosome-inactivating proteins (RIPs), such as gelonin and saporin, significantly enhancing their cytotoxicity in both *in vitro* studies[99–101] and *in vivo* models[102]. These toxins consist only of a single enzymatic A-chain, responsible for their toxic activity, but they lack an additional B-chain for cell targeting, as type II RIPs. As a consequence, type I RIPs are taken up primarily through pinocytosis and typically directed to lysosomes for degradation, resulting in a limited cytotoxicity in intact cells. By facilitating endosomal escape, PCI allows these toxins to bypass lysosomal degradation, greatly improving their therapeutic efficacy. Furthermore, PCI has shown great promise in enhancing the efficacy of various immunotoxins, including MOC31-gelonin in EpCAM-positive cancer cells[103], EGF-saporin and centuximab-saporin in EGFR-positive cancer cells[104,105], and VEGF121/rGel in VEGFR1 expressing cancer cell lines[106].

PCI's potential also extends to the field of immunotherapy, including its combination with cancer vaccines and checkpoint inhibitors. Preclinical studies suggest that PCI can improve antigen presentation, thereby boosting the efficacy of cancer vaccines[94]. By improving the intracellular delivery of vaccine components, PCI has the potential to amplify immune responses, making it a valuable tool in combination cancer therapies[91]. Despite these advances, there are still challenges to be addressed before PCI full potential can be realized. Further research is needed to optimize the choice of PSs and therapeutic agents, improve the light delivery systems, and fully understand the long-term safety of PCI-based therapies. Nonetheless, PCI presents a powerful, localized method for enhancing the cytosolic delivery of

therapeutic agents, making it a promising technology for advancing cancer treatment and overcoming barriers in intracellular drug delivery.

Chapter 4

Aim of the Work: Design of a Supramolecular Complex for Targeted PIT in Cancer Treatment

In the rapidly evolving field of nanomedicine, immunoconjugates represent a groundbreaking fusion of targeted therapy and advanced nanotechnology. These innovative constructs harness the specificity of antibodies to deliver therapeutic agents directly to disease sites, thereby minimizing off-target effects and enhancing treatment efficacy[87]. The combination of immunoconjugates with photodynamic therapy (PDT), a novel technique termed photoimmunotherapy (PIT), is particularly promising, offering a more precise and effective approach to cancer treatment[4]. PD-L1, a major molecular target in immunotherapy, is overexpressed in several cancers and plays a critical role in tumor immune evasion and drug resistance by binding PD-1, primarily expressed on T-cells[80,87]. By inhibiting the PD-1/PD-L1 axis, immunotherapies, such as monoclonal antibodies, allow the immune system to coordinate an effective and sustained response against tumors.

To advance targeted cancer therapy, we developed a supramolecular complex that combines photosensitizing and targeting capabilities. We employed atezolizumab, an immune checkpoint inhibitor (ICI) against PD-L1, as both the carrier and targeting system, and eosin, a well-known photosensitizer (PS), as the active compound. To form a stable protein-based nanostructure, late abbreviated as EITC-atezolizumab, the PS was covalently linked to the antibody (Figure 4.1). Atezolizumab enhances immune recognition of tumor cells and improves targeting precision through its specific binding to PD-L1-expressing cancer cells. This design aims to increase therapeutic efficacy while minimizing damage to healthy tissues. Additionally, atezolizumab's ability to inhibit tumor cell immune evasion through the blockade of the PD-1/PD-L1 interaction may improve treatment effectiveness. Recent studies have demonstrated that photoactive conjugates containing eosin are effective against bacteria[22,107,108] and cancer cells[109] through photoactivation, making eosin an excellent candidate for

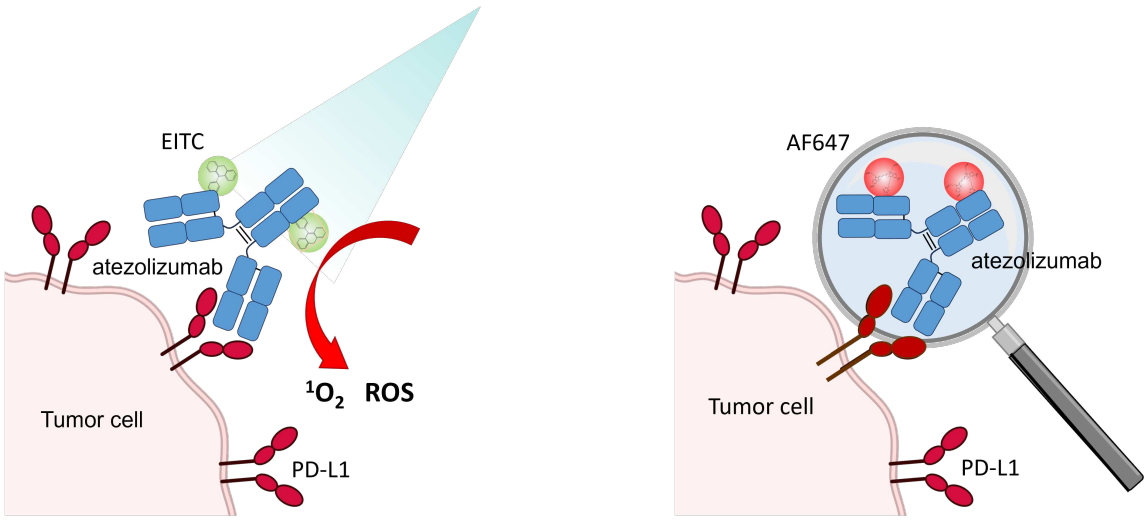

(A) *The EITC-atezolizumab Complex for PDT*

(B) *The AF647-atezolizumab Complex for Imaging*

Figure 4.1: Schematic representation of supramolecular complexes utilized for PDT and imaging. A) Sketch representing EITC-atezolizumab binding PD-L1 receptors. Atezolizumab acts as targenting system and is covalently linked to the PS EITC. Upon light activation, EITC reacts with molecular oxygen to generate $^1O_2$ and ROS. B) Sketch representing a similar complex modified for imaging with the brighter fluorophore AF647 replacing EITC. dSTORM and confocal images were acquired to prove the selectivity of the conjugate for PD-L1 and track its subcellular distribution. Adapted from Alampi et. al[110].

photoinducing cancer cell death. The project aims to evaluate the therapeutic effectiveness of this novel photoimmunoconjugate and to explore correlations between treatment outcomes and PD-L1 density on NSCLC cells. Given that PD-L1 expression levels can vary significantly among cancer cells, establishing whether tumors with higher PD-L1 expression are more susceptible to this targeted approach is of utmost importance for personalizing cancer therapy based on PD-L1 expression profiles and potentially improving patient survival rates. In this scenario, the method used to compare receptor density across different cell lines is crucial for investigating how PD-L1 levels affect treatment outcomes.

In this study, we tested the selectivity of the EITC-atezolizumab complex for PD-L1 and assessed PD-L1 levels across three different cell models using flow cytometry and dSTORM super-resolution microscopy. Both techniques rely on fluorescent probes to detect membrane receptors. However, while eosin is a potent $^1O_2$ generator, its limited brightness restricts its use for effective imaging and monitoring, preventing the EITC-atezolizumab complex from being suitable for these applications. To stain PD-L1 receptors, we employed a standard protocol using commercially available antibodies in flow cytometry experiments; for dSTORM imaging, instead, we conjugated the Alexa Fluor 647 dye to atezolizumab (Figure 4.1B). Alexa Fluor 647, hereafter referred to as AF647, offers superior fluorescence and brightness compared to eosin, allowing for more accurate visualization of the immunoconjugates' distribution and localization on PD-L1-expressing cells, and thereby improving the overall reliability of our experimental approach.

4.1 PD-1/PD-L1 Immune Checkpoint

Immune checkpoints play a crucial role in regulating the immune response, and their manipulation has become a cornerstone of modern cancer therapy. Among these, the programmed death receptor 1 (PD-1) and its ligand, programmed death ligand 1 (PD-L1), have emerged as crucial targets, fundamentally transforming cancer treatment.

The PD-1/PD-L1 axis functions as a vital immune checkpoint, modulating the immune system's ability to attack cancer cells. Under normal conditions, this pathway is crucial for maintaining self-tolerance and preventing autoimmune reactions by suppressing T-cell activity[80]. However, many tumors exploit this mechanism to evade immune surveillance by over-expressing PD-L1, which inhibits anti-tumor immune responses and promotes tumor growth.

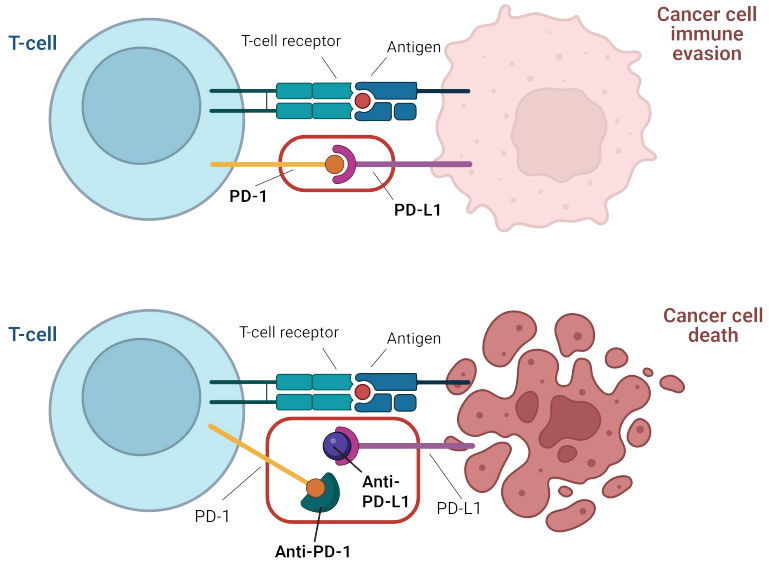

Figure 4.2: Illustration of the PD-1/PD-L1 interaction and the mechanism of action of checkpoint inhibitors. PD-L1, expressed on tumor cells, binds to the PD-1 receptor on T-cells, leading to immune suppression and allowing cancer cells to evade immune detection. Checkpoint inhibitors block this binding, reactivating T-cells and restoring their ability to attack and destroy cancer cells, thereby enhancing the immune response against tumors. Created in Biorender.com.

PD-1, also known as CD279, is a type I transmembrane glycoprotein predominantly found on activated T-cells, but it is also present on B-cells, natural killer cells, dendritic cells, and certain myeloid cells. It functions as an inhibitory receptor within the CD28 family, crucial for downregulating immune responses and maintaining self-tolerance. When PD-1 engages with its ligands, PD-L1 (CD274; B7-H1) and PD-L2 (CD273; B7-DC) to form a 1:1 complex, it transmits inhibitory signals that reduce T-cell proliferation, cytokine production, and cytotoxic activity[111]. This regulatory function is essential for preventing autoimmune damage and controlling inflammatory responses.

PD-L1 is a transmembrane protein widely expressed on various cell types, including tumor cells, antigen-presenting cells, and non-hematopoietic cells. PD-L1 is not just a passive receptor that binds to PD-1 on T-cells to suppress immune responses. It can also send signals back into the tumor cell, a

process known as reverse signaling. Studies have suggested that this signaling can promote tumor cell survival, resistance to apoptosis, and even increased proliferation, even without binding to PD-1[112–116]. In contrast, PD-L2, while structurally similar, is more selectively expressed, primarily on dendritic cells and macrophages[86], but its interaction with PD-1 has been less extensively explored compared to the well-studied PD-1/PD-L1 pathway.

The PD-1/PD-L1 interaction triggers a cascade of intracellular events, leading to the phosphorylation of PD-1's intracellular domains and the recruitment of the phosphatase SHP-2. SHP-2 then dephosphorylates key molecules involved in T-cell receptor signaling, reducing T-cell activity[80]. Consequently, T-cells produce fewer cytokines, proliferate less, and exhibit diminished cytotoxicity. While this mechanism is essential for immune homeostasis, tumors often hijack it by upregulating PD-L1, thus escaping immune surveillance. To counteract this evasion, ICIs have been developed to block the PD-1/PD-L1 interaction. These monoclonal antibodies specifically target PD-1 or PD-L1, preventing their binding and effectively removing the inhibitory signals that suppress T-cell activity. As a result, T-cells are reactivated to target and destroy cancer cells, leading to significant tumor regression and, in some cases, long-term remission (Figure 4.2).

As mentioned, PD-L1 is expressed in a variety of human cancers, including lung carcinomas[86], but its levels can vary significantly depending on the cell type and are influenced by multiple factors which can either lead to its upregulation or downregulation. For instance, interferon-gamma (IFN-γ) is a key upregulator of PD-L1, enhancing its levels by activating specific signaling pathways[80]. Conversely, interleukin-6 (IL-6) can downregulate PD-L1 through the activation of transcription factors often linked to tumor progression and immune evasion[117]. Additionally, high oxidative stress levels and therapies targeting PD-1 or PD-L1 can also influence PD-L1 expression, often reducing its levels[118]. However, the regulation of PD-L1 expression in tumors is complex, and the correlation between PD-L1 expression levels and treatment outcomes is still not fully understood, highlighting the need for further research to clarify how these factors influence therapeutic efficacy and patient responses to immunotherapy.

4.2 Targeting System: Atezolizumab

Atezolizumab (Tecentriq, Genentech, Inc.) is the first PD-L1 inhibitor approved by the FDA in 2016 for treating patients with metastatic urothelial carcinoma or non-small cell lung cancer[119]. Atezolizumab is a fully human IgG1 antibody directed to PD-L1 with a modified Fc fragment. The Fc region on an antibody tipically binds Fcγ receptors on various immune cells, whose engagement is particularly important to elicit antibody effector functions, like antibody-dependent cellular cytotoxicity (ADCC) and complement-dependent cytotoxicity (CDC) against PD-L1-positive cancer cells. However, ICIs are not tumor-specific and stimulated ADCC/CDC can destroy healthy cells, causing tissue damage and unwanted side effects. To prevent this, atezolizumab has an N297A mutation in its Fc domain which

leads to antibody aglycosylation and eliminates effector functions[120].

Immunoglobulins G (IgGs) consist of two heavy (H) chains and two light (L) chains. Each heavy chain has three constant domains (C_H1, C_H2 and C_H3) and one variable domain (V_H). Light chains instead have only two domains, one constant (C_L) and one variable (V_L). When fully folded, each IgG antibody can be cleaved into three functionally distinct fragments: one crystallizable fragment (Fc), formed by the paired C_H2 and C_H3 domains, and two identical fragment antigen binding (Fab) regions, each consisting of a full light chain and the V_H and C_H1 domains of the heavy chain. The Fab regions are responsible for antigen recognition and binding. A short and flexible sequence of amino acids, called the hinge region, links each Fab region to the Fc region by disulfide bonds.

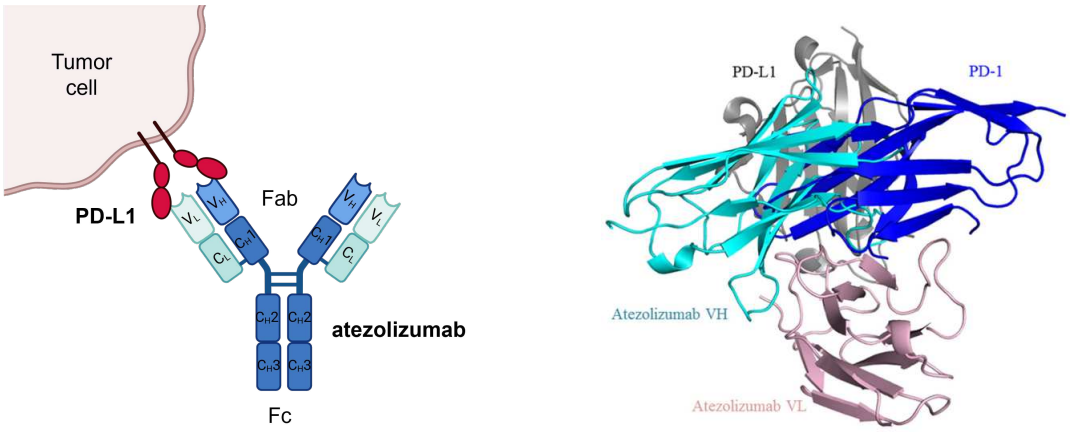

(A) *Atezolizumab Binding PD-L1*

(B) *Superimposition of PD-1/PD-L1 and PD-L1/atezolizumab Complexes*

Figure 4.3: Interaction of atezolizumab with PD-L1. A) Sketch representing atezolizumab binding PD-L1. Heavy and light chains are represented in blue and green, respectively. Costant (C) and variable (V) domains are specified. B) Superimposition of PD-1/PD-L1 complex and PD-L1/atezolizumab complex from Zhang et. al[121]. PD-1 and atezolizumab compete for the same surface area on PD-L1.

Zhang et. al. recently solved the crystal structure of atezolizumab, and showed that both its heavy and light chains interact with PD-L1, thereby participating in binding[121]. They also superimposed the structure of PD-L1/atezolizumab complex with the structure of PD-1/PD-L1 complex (PDB: 4ZQK), demonstrating that atezolizumab competes with PD-1 for the same surface area of PD-L1 (Figure 4.3B). Hence, they can't bind the same receptor simultaneously and atezolizumab effectively blocks PD-1/PD-L1 pathway. Notably, in contrast to what happens with the monoclonal antibodies pembrolizumab and nivolumab that bind PD-1, the structure of PD-L1 does not change significantly after the binding with anti-PD-L1 antibodies[111].

The amino acids sequence of atezolizumab was used to estimate the extinction coefficient of the protein at 280 nm, as previously described[122]:

$$\epsilon(280nm)(M^{-1}cm^{-1}) = (\#Trp)(5,500) + (\#Tyr)(1,490) + (\#cistyne)(125) \tag{4.1}$$

From the previous equation, we obtained a value of 232,400 M^{-1} cm^{-1}, that was used to calculate the concentration of the antibody in all the experiments of this work.

To date, atezolizumab has been used for PIT only in one study, where it was combined with the PS chlorin e6 to treat HCT-116 colon cancer cells. The results showed that, in a mouse model, tumor mass decreased by over 50% when the treatment was applied under light exposure, compared to dark conditions[68]. Additionally, atezolizumab was used in photochemical internalization experiments to target cells expressing PD-L1. This approach combined atezolizumab with the PS fimaporfin/$TPCS_{2a}$ to enable light-triggered release of drugs from endo/lysosomal compartments, thereby enhancing the selective elimination of PD-L1-positive cells through light activation[101].

4.3 Photosensitizer: Eosin 5-Isothiocyanate

Figure 4.4: Chemical structure of eosin 5-isothiocyanate.

Eosin, also known as tetrabromofluorescein, is a synthetic acid derivative of brominated fluorescein. It is widely recognized for its utility as a histological stain, commonly used in combination with other dyes such as hematoxylin and methylene blue. Eosin has received FDA approval for use in pharmaceuticals and cosmetics due to its safety and effectiveness[127]. As an organic sodium salt, it is soluble in both aqueous and polar organic solvents, whereas its photophysical properties are significantly influenced by the solvent's polarity[128]. In non-aqueous solutions, reduced quenching effects and non-radiative losses, along with better stabilization of the triplet state, often lead to increased quantum yields of fluorescence, triplet state formation and singlet oxygen generation. Among organic solvents, DMSO is particularly effective for diluting eosin. However, its potential toxicity and disruptive effects on cellular systems make it unsuitable for certain biological applications; thus, PBS is generally preferred in these contexts. The main photophysical properties of eosin in aqueous solution are reported in table 4.1.

In this work, eosin 5-isothiocyanate (EITC) was used. EITC is an amine-reactive derivative of eosin, where the isocyanate group (-N=C=O) has been substituted with an isothiocyanate group (-N=C=S). This structural modification introduces a sulfur atom in place of the oxygen atom, enhancing its reactivity

	τ (ns)	Φ_F	Φ_T	Φ_Δ
Eosin	1.21[123]	0.2[124]	0.71[125]	0.61[126]
		0.24[123]	0.8[124]	
			0.64[126]	

Table 4.1: Photophysical properties of the molecule eosin dissolved in PBS buffer.

towards amine, thiol and hydroxyl groups in biological molecules. The chemical formula for EITC is $C_{21}H_7Br_4NO_5S$, and its structure is reported in Figure 4.4. EITC exhibits improved photostability and distinctive photophysical characteristics compared to the original fluorescein. This improvement is attributed to the presence of four bromine atoms on the eosin core, which increase spin-orbit coupling and thereby enhance the likelihood of intersystem crossing. This results in efficient formation of the triplet state, crucial for its role as a PS, but also in a reduced fluorescence brightness.

The molecular weight of EITC is 704.96 and its molar extinction coefficient is 95,000 M^{-1} cm^{-1} at 525 nm. Its unique properties make EITC a versatile and effective PS, with possible applications in PDT, cell imaging, and molecular labeling.

Chapter 5

Materials and Methods

5.1 Materials

CD274 (PD-L1, B7-H1) Antibody (Catalog #13-5983-82), Mouse IgG1 Cross-Adsorbed Secondary Antibody (Catalog #A-21240), CellMask™ Plasma Membrane Stain, LysoTracker® Probe and Alexa Fluor 647 NHS ester were purchased from Invitrogen by Thermo Fisher Scientific (Waltham, Massachusetts, USA). IgG from normal human serum and eosin 5-isothiocyanate (EITC) were from Sigma-Aldrich (Saint Louis, MO, USA). The therapeutic antibody atezolizumab was obtained from the Inpatient Pharmacy of University Hospital of Parma and the Hospital Pharmacy at Oslo University Hospital, Rikshospitalet (Oslo, Norway). PD-10 desalting columns were from Cytiva (Marlborough, MA, USA). Phycoerythrin (PE) isotype control mouse IgG1κ (clone MOPC-21, Catalog #554680) and PE anti-human PD-L1 (clone MIH1, Catalog #557924) were purchased from BD Biosciences (San Jose, CA, USA). The photosensitizer $TPCS_{2a}$ (fimaporfin) and the toxin gelonin were provided by PCI Biotech AS (Oslo, Norway).

5.2 Cell Lines

The human non-small cell lung cancer (NSCLC) cell lines H322 (ATCC CRL-5806), H1975 (ATCC CRL-5908), and A549 (ATCC CCL-185), and the human breast cancer cell line MDA-MB-231 (ATCC HTB-26) were originally obtained from the American Type Culture Collection (ATCC, Manassas, VA, USA). The human dermal fibroblast (HuDe) cell line was obtained from the Istituto Zooprofilattico Sperimentale (Brescia, Italy). MDA-MB-231, H322, H1975 and A549 cells were cultured in Roswell Park Memorial Institute medium (RPMI 1640) supplemented with 2 mM Glutamine. Only for PCI experiments, A549 cells were cultured in Ham's F-12K (Kaighn's) Medium. HuDe fibroblasts were cultured in Dulbecco's Modified Eagle Medium (DMEM) supplemented with 2 mM Glutamine.
All cultured media were supplemented with 10% Fetal Bovine Serum (FBS), and 100 U/ml Penicillin-100 µg/ml Streptomycin. All cell models were maintained at 37°C in a water-saturated atmosphere of 5% CO_2 in air.

5.3 Purification of Atezolizumab and Labeling with EITC or Alexa Fluor 647

Atezolizumab was endowed with phosensitizing or fluorescent properties through conjugation with eosin 5-isothiocyanate (EITC) or an N-hydroxysuccinidimidyl ester (NHS) derivative of Alexa Fluor 647 (AF647), respectively. For both dyes, the reaction happens with the primary amines of the protein to form stable dye-antibody complexes, referred to as EITC-atezolizumab or AF647–atezolizumab.

Prior to labeling, atezolizumab was purified from excipients in the pharmacological solution and placed in PBS buffer at pH = 7 by means of a gravity column for desalting (Sephadex G25, PD-10 column). The dyes were dissolved in DMSO buffer to obtain a concentrated stock solution of a few millimolar (mM), and an excess of dye was added to the antibody solution to initiate the reaction. In the final volume, the molar ratio of antibody to dye was 1:6. For the EITC-atezolizumab conjugation, the reaction mixture was incubated overnight at room temperature. For the AF647-atezolizumab conjugation, sodium bicarbonate was added to a final concentration of 0.1 M (10% of the total volume) and the mixture was stirred for 2 hours at room temperature. After incubation, samples were filtered using a PD-10 column equilibrated with PBS buffer at pH = 7 to separate dye-protein conjugates from unbound fluorescent dyes. Finally, the concentration of the complex and its degree of labeling (DOL) were determined spectroscopically as:

$$[Protein(M)] = \frac{[A_{280} - (A_{dye} \times CF_{280})] \times dilutionfactor}{\epsilon_{ab}} \tag{5.1}$$

$$DOL = \frac{A_{dye} \times dilutionfactor}{\epsilon_{dye} \times [protein(M)]} \tag{5.2}$$

where ϵ is the extinction coefficient at λ_{max} in M^{-1} cm^{-1}, and CF_{280} is the correction factor for the dye's contribution to the absorbance at 280 nm.

The DOL is expressed as moles dye per mole protein, and indicates the average number of dye molecules coupled to each antibody molecule. In our preparations, we obtained a DOL $\approx$ 2.5 for both dyes. The values of ϵ and CF_{280} for EITC and AF647 are reported in table 5.1.

Dye	λ_{max} **(nm)**	ϵ **(M^{-1} cm^{-1})**	**CF_{280}**
EITC	525	95,000	0.28
AF647	650	239,000	0.03

Table 5.1: Properties of EITC and Alexa Fluor 647 used to label atezolizumab.

5.4 Fluorescence Spectroscopy: Steady-State and Time-Resolved Techniques

5.4.1 Steady-State Measurements and Fluorescence Decays

Absorption spectra were collected using the Jasco V-650 (Jasco Europe) double-beam spectrophotometer. Steady-state fluorescence measurements were conducted using an FS5 Spectrofluorometer (Edinburgh Instruments Ltd., Livingston, UK). For all samples, fluorescence excitation, fluorescence emission, and anisotropy spectra were recorded.

A comparative method was used to estimate the fluorescence quantum yield, Φ_F, of EITC-atezolizumab from the emission spectra, using eosin in PBS as reference molecule:

$$\Phi_{F,EITC-atez} = \Phi_{F,eosin} \cdot \left(\frac{F_{EITC-atez}}{F_{eosin}}\right) \cdot \left(\frac{1-10^{-A_{eosin}}}{1-10^{-A_{EITC-atez}}}\right) \tag{5.3}$$

where F is the integrated fluorescence intensity, and A is the absorbance at the excitation wavelength. The experiments were conducted at a temperature of 20°C.

Fluorescence lifetime decays were recorded with an FLS920 time-correlated single photon counting (TCSPC) system (Edinburgh Instruments Ltd., Livingston, UK) with pulsed LED excitation at 500 nm for EITC or 600 nm for AF647, and a repetition rate of 5 MHz. Data were analyzed using the analysis software FLS980 by operating the re-convolution between the exponential decay model and the experimental instrument response function (IRF), obtained by measuring the scattered light from a suspension of polystyrene beads. To ensure the accuracy of the fits, the reduced chi-squared value was minimized. Additionally, the fit quality was further verified by visually examining the weighted residuals and their autocorrelation.

The mean fluorescence lifetime, τ_{mean}, for a biexponential decay was calculated as a weighted average of the two lifetimes, τ_1 and τ_2, with corresponding amplitudes A_1 and A_2, using the following formula:

$$\tau_{mean} = \frac{A_1\tau_1 + A_2\tau_2}{A_1 + A_2} \tag{5.4}$$

5.4.2 Triplet Quantum Yield and Triplet State Decays

To gain a comprehensive understanding of the photophysical properties of our samples, the triplet quantum yield, Φ_T, and triplet state decays were measured. These evaluations are crucial for determining the efficiency of intersystem crossing and the lifetime of the triplet state, which are strictly interconnected with the quantum yield of $^1O_2$ production (see below).

To monitor the formation and decay of the triplet state of our samples, we exploited the laser flash photolysis (LFP) technique. This time-resolved method allows to track the time evolution of excited states via transient absorption measurements. The experimental set-up was previously described in detail[129]. The sample was photoexcited with the second harmonic (532 nm) of a pulsed Nd:Yag laser

(Surelite I-10, Continuum, San Jose, CA, USA). The continuous wave (cw) output of a Xe arc lamp, coupled to a monochromator, served as probe for the detection. To minimize light scattering from the excitation beam, the probe beam was oriented at a 90° to the pump beam. The transmitted light was then collimated and focused through the slits of a second monochromator coupled to a photomultiplier, with the signal subsequently loaded onto a digital oscilloscope. The baseline measurement was obtained by blocking the pump beam, thereby illuminating the sample only with the probe beam.

In transient absorption measurements, the excitation of the sample with a nanosecond pulsed laser (pump) results in the formation of short-living transient species, which can cause the sample's absorption to either increase or decrease relative to the ground state. The absorption variation ΔA at a specific detection wavelength is defined as:

$$\Delta A(t) = \log\left(\frac{I_0(t < t_0)}{I(t)}\right) \tag{5.5}$$

where I_0 and I are the intensities (corrected for the signal of the baseline) of the probe light that passes through the sample, measured before and after laser excitation, respectively.

In this work, the kinetics of EITC-atezolizumab and free EITC were followed at 526 nm and 524 nm, respectively. EITC was used as reference for determining the quantum yield of triplet state formation for EITC-atezolizumab:

$$\Phi_{T,EITC-atez} = \Phi_{T,EITC} \cdot \left(\frac{\Delta A_{EITC-atez}}{\Delta A_{EITC}}\right) \cdot \left(\frac{1 - 10^{-A_{532,EITC}}}{1 - 10^{-A_{532,EITC-atez}}}\right) \tag{5.6}$$

where ΔA values were retrieved from the experimentally measured transient absorbance changes.

5.4.3 Singlet Oxygen Quantum Yield

The efficiency of EITC-atezolizumab in generating $^1O_2$ is crucial for its application in PDT. The singlet oxygen quantum yield, Φ_Δ, of the complex was estimated using a comparative method with a reference compound of known quantum yield. $^1O_2$ detection in solution was achieved using the commercially available fluorescent sensor named Singlet Oxygen Sensor Green (SOSG) (Invitrogen, Waltham, MA, USA), following the manufacturer's instructions. A 5 mM stock solution of SOSG in methanol was prepared immediately before measurements.

The SOSG molecule consists of a fluorescein derivative moiety (*Fl*) and an anthracene-derived trapping moiety (*An*) covalently linked together. In the absence of oxygen, a photo-induced electron transfer (PET) occurs between the trapping moiety (electron donor) and the fluorophore (electron acceptor), resulting in fluorescence quenching of the fluorophore in its singlet excited state. Conversely, when the anthracene moiety reacts with $^1O_2$, it forms an endoperoxide (EP) anthracene moiety with a HOMO energy lower than that of the fluorophore. This change prevents the trapping moiety from quenching the fluorophore, allowing it to decay through fluorescence.[36]. The SOSG molecule and the formation of SOSG-EP are reported in Figure 5.1. Since the concentration of $^1O_2$ produced upon illumination is

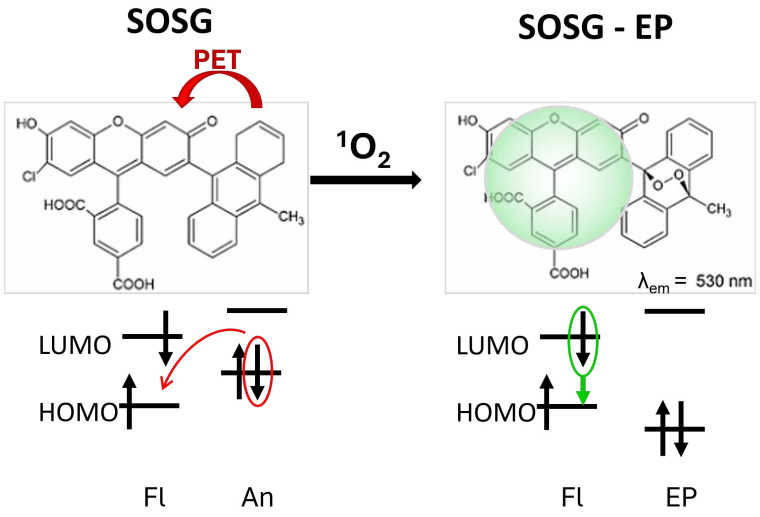

Figure 5.1: Chemical structure of SOSG molecule and intramolecular PET which results in fluorescence quenching. Upon interaction with $^1O_2$, SOSG-EP is formed and the fluorescence pathway is repristinated. Adapted with permission from Kim et. al[36]. Copyright 2024 American Chemical Society.

directly proportional to the fluorescence emission intensity of SOSG, singlet oxygen quantum yield of EITC-atezolizumab can be retrieved by comparing the integrated fluorescence intensities of SOSG in the sample and reference solutions, corrected for the emission of SOSG alone.

In this work, rose bengal and eosin were used as reference compounds. Solutions containing SOSG + immunoconjugate, SOSG + rose bengal, SOSG + eosin or only SOSG were prepared in order to have a final concentration of SOSG of 1.5 μM. The solutions were illuminated for 160 seconds using a continuous wave Nd:YAG laser (Laser Quantum, Manchester, UK) with an internally frequency-doubled output at 532 nm (1 W), attenuated to 30 mW. Emission spectra of SOSG in each solution were recorded every 20 seconds between 495-700 nm (λ_{ex} = 488 nm). The fluorescence intensity of SOSG at 528 nm against the illumination time were plot and a linear fit was performed to determine the slope of the fit for the sample (EITC-atezolizumab) and the reference compounds (rose bengal and eosin). Finally, the quantum yield of singlet oxygen formation was determined using the follow equation:

$$\Phi_\Delta = \Phi_{\Delta,ref} \cdot \left(\frac{slope_{EITC-atez}}{slope_{ref}}\right) \cdot \left(\frac{1-10^{-A_{EITC-atez}}}{1-10^{-A_{ref}}}\right) \tag{5.7}$$

where A is the absorbance at 532 nm.

5.5 dSTORM Super-Resolution Microscopy

5.5.1 Principles and Microscope Setup

Direct stochastic optical reconstruction microscopy (dSTORM) is a single-molecule–based localization technique that allows sub-diffraction-limit resolution of labeled structures by means of reversibly photoswitchable fluorophores and fluorescent probes. The photoswitching mechanism, named blinking, is reported in Figure 5.2. The fluorophore in the triplet state (^{3}F) can decay back to the ground state

or be reduced to a non-fluorescent (dark or "off ") state, F·, in the presence of electron donors, such as thiols. Some fluorophores might be further reduced by thiols to a non-fluorescent leuco form (FH). Both the radical F· state and the leuco FH state can recover the fluorescent state (often referred to as the "on" state) spontaneously or by oxidation[130]. Principle of dSTORM is based on the ability of some fluorophores to undergo several off-on-off cycles: upon irradiation, the majority of fluorophores goes to a dark state and only a small fraction of them resides in an activated fluorescent state and are optically resolvable from the rest, meaning that they can be localized with high precision since their images are not overlapping. Then, activated fluorophores return to the ground state from which they can be

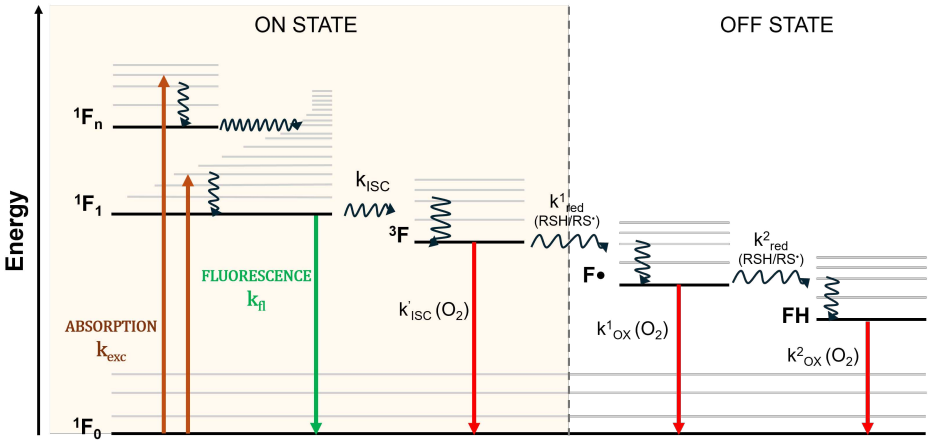

Figure 5.2: Photoswitching mechanism of fluorophores in dSTORM. The triplet state of the fluorophore, ^3F, can be reduced by thiols (e.g., β-mercaptoethylamine (MEA) or GSH) to a non-fluorescent state, either the radical state F· or the leuco state FH. The oxygen naturally present in aqueous solutions oxidises the dark states, which are switched back to the fluorescent state.

excited again or undergo photobleaching. This process is repeated several times in order to collect an image stack of thousands of images, in each of which a different subset of fluorophores is stochastically activated and detected. The super-resolved image is eventually reconstructed from the point-spread function of each molecule localized. An appropriate solution buffer containing both an oxygen scavenger and a thiol-containing reducing agent is required to favor the blinking mechanism[131,132].

In this work, we used a dSTORM buffer composed of 5% w/v glucose, 100 mM cysteamine, 0.5 mg/ml glucose oxidase, and catalase 40 mg/ml in PBS buffer (pH = 7.4). Image quality was enhanced working in total internal reflection fluorescence (TIRF) mode and about 20 nm resolution was achieved, overcoming the optical diffraction limit imposed by Abbe's law. Super-resolved images were acquired using the Oxford Nanoimaging (ONI) Nanoimager-S Mark III microscope equipped with a 100x/1.4 oil immersion objective from Olympus and four excitation lasers (405/488/561/640 nm). The fluorescence emission was collected by the objective and split into two channels (576-620 nm and 665-705 nm) by a 640LP dichroic beam-splitter. Finally, the signal was recorded using a CMOS camera (Hamamatsu OrcaFlash 4.0) to obtain 428 × 684 images with a pixel size of 117 nm.

5.5.2 Sample Preparation and Imaging

Viable cells ($15x10^3$ cells per well) were seeded in 8-well Chamber Slides (Thermo Scientific, Waltham, MA, USA, Nunc Lab-Tek II Chamber Slide) and allowed to grow for 48 hours in the incubator. Cells were chemically fixed by adding 100 μl of 2% PFA in PBS for 15 minutes at room temperature, and next gently rinsed three times with PBS. After the washing steps, a blocking solution composed of PBS + 2% BSA was added to each well, and incubated for 20 minutes at room temperature, in order to reduce the amount of unspecific binding. Cells were finally rinsed twice with PBS and left in PBS buffer. To label PD-L1 receptors, an anti-PD-L1 primary monoclonal antibody was added at the concentration of 5 μg/ml in PBS + 1% BSA and incubated for 1 hour at room temperature. Cells were rinsed three times with PBS and then incubated with an AF647-conjugated secondary antibody (5 μg/ml) diluted in PBS + 1% BSA + 0.05% Tween 20 at room temperature for 1 hour protected from light. Finally, cells were gently washed three times with PBS to remove any unbound antibody, and placed in dSTORM imaging buffer. Cells incubated with the secondary antibody only were used as controls.
During dSTORM acquisition, the sample was continuously illuminated at 640 nm (nominal power: $\sim$327 mW) with an integration time of 15 ms for 20,000 frames. For each cell model, a minimum of 11 cells were sampled, and at least 5 cells were included for each control experiment. To identify signals from individual receptors (see Section 5.5.3), calibration images were collected under the same imaging condition, but with a reduced concentration of primary antibody (0.125 μg/ml) to allow only a subset of well-separated PD-L1 proteins on the cell surface to be fluorescently tagged.
In those experiments whether the ability of atezolizumab to selectively target PD-L1 was investigated, cells were stained with 1 μM AF647-atezolizumab in FBS-free medium at 37°C for 1 hour in the dark, and then fixed as described above. dSTORM buffer was added right before imaging. In control experiments, cells were incubated with an AF647-labelled IgG to evaluate nonspecific staining.

5.5.3 dSTORM Images Analysis

All acquired image stacks were reconstructed and processed using NimOS software (v1.19.4) from ONI. The software identifies the positions of each blinking dye in every frame by fitting the point-spread function of the emission with a 2D Gaussian, and determining the center of the emission. The x-y coordinates, referred to as localizations, are saved in a .csv file. The final super-resolved image is reconstructed by plotting the position of each fluorophore. The intensity threshold of single-molecule detection was set to a minimum of 300 photons to filter out false spots caused by noise. Intensity values of 500 and 800 were also tested, but increasing the threshold did not enhance image quality; instead, real localizations could be missed by the software. The first 1500 frames were discarded do to artifacts from the non-blinking behaviour of fluorophores during the initial milliseconds of illumination. Data analysis was performed using a custom MatLab script, which quantifies localization density in

selected regions of interest (ROIs) from each dSTORM image using the localization list and corresponding bright field image. ROIs were manually selected on bright field images by drawing polygonal areas that matched the cell shape. In order to quantify PD-L1 membrane receptors, the localization density within each cell has to be divided by the number of localizations per single PD-L1. This is necessary due to the fact that a single fluorophore might blink multiple times within the acquisition time, and polyclonal secondary antibodies may bind multiple fluorophores to a single receptor. Calibrated dSTORM images, obtained with a low concentration of primary antibody, were used to determine the mean number of localizations per single PD-L1. At this purpose, clusters of localizations were identify by means of a previously developed mean-shift clustering algorithm[6,133], which outputs, given a specified bandwidth of 30 nm, a set of cluster centers indicating the position of each receptor. Clusters were filtered to exclude those containing less than 5 localizations or with an unrealistic size ($>$ 100 nm) for a receptor. The remaining clusters were binned based on their number of localizations, resulting in a distribution that was not symmetrical. The average number of localizations per receptor was finally obtained by fitting the distribution with a mono-exponential function and extracting the mean value from the fitted curve.

5.6 Confocal Microscopy

5.6.1 Sample Preparation and Imaging

Confocal images of fixed NSCLC cells were acquired to monitor PD-L1 internalization and determine the distribution of atezolizumab at cellular level. A sequential addition protocol without washing steps was employed to label PD-L1 receptors, the plasma membrane and acid organelles with AF647-atezolizumab (1 μM), CellMask® Green Plasma Membrane (1x) or LysoTracker blue (75 nM), respectively. The order of dye addition was adjusted based on the required incubation time for the AF647-atezolizumab complex, which was varied to test six different conditions, that is 5 minutes, 30 minutes, 1 hour, 2 hours, 6 hours and 24 hours of incubation. The incubation time for LysoTracker was 1 hour, whereas CellMask was incubated for 10 minutes. All incubations were performed in culture medium at 37°C and the samples were kept in the dark. After the final incubation period for each condition, cells were extensively rinsed with PBS and fixed as described in Section 5.5.2.

The samples were immediately imaged by means of a Zeiss C Plan-Apochromat 63x/1.4 NA oil DICII on a confocal/two-photon laser-scanning microscope (LSM 980 NLO Airyscan 2, Carl Zeiss MicroImaging GmbH, Jena, Germany). The microscope is equipped with five diode lasers (405/445/488/514/639 nm), and a DPSS laser (561 nm). To minimize cross-talk between channels, sequential scanning was employed. LysoTracker was excited at 405 nm and an emission filter of [410-464 nm] was set. For CellMask, an excitation wavelength of 488 nm and an emission filter of [490-642 nm] were used. AF647-atezolizumab was excited at 639 nm with emission collected through a [642-695 nm] filter. The

pinhole size was set to 1 airy unit for all channels. Three independent experiments were conducted for each condition, with a minimum of 25 cells imaged per condition in each experiment.
To provide additional and complementary insights into the vesicular trafficking of PD-L1, particularly the involvement of late endosomes, immunofluorescence analysis was performed using cells stained with a CD63 (MX-49.129.5) mouse monoclonal antibody. Following PD-L1 staining with AF647-atezolizumab, the cells were fixed with 2% PFA for 15 minutes, permeabilized with 0.5% Triton X-100 in PBS + 3% BSA for 1 hour, and finally incubated with CD63 (1:400) overnight at 4°C. Detection of late endosomes in the cytoplasm was performed using a Goat anti-Mouse IgG (H+L) secondary antibody (1:500) conjugated to Alexa Fluor 488 (AF488) in PBS containing 3% BSA for 1 hour at room temperature. Images were acquired using a Plan Apo VC 100x Oil DIC N2 Objective mounted on a Nikon AXR line-scanning confocal microscope provided with the Nikon spatial array confocal (NSPARC) detector. AF488-labelled secondary antibody and AF647-atezolizumab were excited at 488 nm and 640 nm, respectively. Two separate experiments were performed for each condition, with at least 20 cells imaged per condition in each experiment.

5.6.2 Confocal Images Analysis

Confocal images analysis and colocalization measurements between PD-L1 and lysosomes were conducted using the ZEN 3.8 software (Carl Zeiss MicroImaging GmbH, Jena, Germany). To filter out low-intensity background fluorescence, a threshold of 5000 intensity units was applied. The degree of colocalization between the AF647 signal (representing atezolizumab bound to PD-L1) and the LysoTracker signal (marking lysosomes) was quantified over time using the Pearson's correlation coefficient and the Mander's overlap coefficient, two widely used methods in fluorescence microscopy to assess spatial relationships between signals[134].
The Pearson's correlation coefficient quantifies the linear correlation between the intensity distributions of two fluorescent signals. It compares how the intensities of the two channels vary across the entire image. For a two-color image, the Pearson's coefficient is calculated as:

$$R_r = \frac{\sum_i (Ch1_i - Ch1_{aver}) * (Ch2_i - Ch2_{aver})}{\sqrt{\sum_i (Ch1_i - Ch1_{aver})^2 * (Ch2_i - Ch2_{aver})^2}} \tag{5.8}$$

where $Ch1_i$ and $Ch2_i$ are the intensity values of pixel i in the first and second channel, respectively, while $Ch1_{aver}$ and $Ch2_{aver}$ are the average intensities of channels 1 and 2 across the entire image. The Pearson's coefficient values are in the range [-1, 1], where:

- +1 indicates a perfect positive correlation, meaning that as the intensity of one signal increases, the other also increases proportionally;
- -1 indicates a perfect negative correlation, where an increase in one signal corresponds to a decrease in the other;

- 0 suggests no linear relationship, meaning the two signals are distributed randomly relative to each other.

The Pearson's correlation coefficient is particularly valuable for assessing the global relationship between two signals. In this study, it was used to reveal how the distribution of the AF647-atezolizumab complex correlates with that of lysosomes marked by LysoTracker. A high Pearson's coefficient would suggest that the internalized antibody is spatially related to lysosomes.

The Mander's overlap coefficient, instead, provides a more direct assessment of spatial colocalization by quantifying the degree of overlap between the two signals. Unlike the Pearson's coefficient, the Mander's coefficient does not rely on intensity relationships but instead measures how much of one signal is co-located with the other within the sample. The Mander's coefficient is split into two components:

$$M_1 = \frac{\sum_i Ch1_{i,coloc}}{\sum_i Ch1_{i,total}} \quad \text{and} \quad M_2 = \frac{\sum_i Ch2_{i,coloc}}{\sum_i Ch2_{i,total}} \tag{5.9}$$

M_1 measures the fraction of signal 1 (i.e., AF647-atezolizumab) that overlaps with signal 2 (i.e., LysoTracker), giving insight into how much of the antibody signal is localized within lysosomes. M_2 measures the fraction of the LysoTracker signal that overlaps with the AF647-atezolizumab signal, showing how much of the lysosomal population is associated with the antibody. Both M_1 and M_2 range from 0 (no overlap) to 1 (perfect overlap). The Mander's overlap coefficient is particularly useful for biological studies, as it gives a more detailed understanding of spatial relationships within a cell.

In this study, the Mander's coefficient indicates the extent to which the AF647-atezolizumab complex is co-localized with lysosomes, helping to assess whether and when the antibody is trafficked to lysosomes after internalization.

5.7 Cell Viability and Cell Death Assays

5.7.1 MTT and MTS Assays

The MTT assay is an established and almost ubiquitous method to assess cell viability and proliferation. It relies on the enzymatic reduction of 3-[4,5-dimethylthiazole-2-yl]-2,5-diphenyltetrazolium bromide (MTT), a yellow water-soluble tetrazolium dye, to MTT-formazan, a violet-blue water-insoluble molecule that requires dissolution with DMSO. Thus, the MTT assay evaluates enzymatic activity mediated by mitochondrial succinate dehydrogenase in living cells.

Similarly, MTS [3-(4,5-dimethylthiazol-2-yl)-5-(3-carboxymethoxyphenyl)-2-(4-sulfophenyl)-2H-tetrazolium] is a tetrazolium salt. However, unlike MTT, the formazan products generated by MTS reduction are water-soluble, eliminating the need for DMSO dissolution. Both assays measure metabolic activity and provide comparable information on cell viability.

Viability was evaluated using the MTT assay 24 hours post-light exposure in all PDT experiments, or with the MTS assay 48 hours after irradiation in PCI experiments, unless otherwise specified.

In brief, for the MTT assay, cells were incubated for up to 1 hour in FBS-free culture medium supplemented with MTT 1 mg/ml. The produced formazan crystals were then solubilized by DMSO and the absorbance was measured at 565 nm by means of a microplate plate reader (Infinite 200 PRO, TECAN, Männedorf, Switzerland). When the MTS assay was performed, cells were incubated with 0.33 mg/ml MTS in cultured media for 2-3 hours. Absorbance was measured at 490 nm using a plate reader (PowerWave XS2 microplate spectrophotometer) with the Gen5 software program (Biotek Instruments Inc., Winooski, VT, USA).

5.7.2 The ATP Assay

The ATP assay relies on the measurement of adenosine triphosphate (ATP) levels using a firefly luciferin-luciferase system. It is well established that the dramatic reduction of ATP is associated to cell death, therefore ATP concentration is an appropriate parameter for measuring living cell number. Besides, the ATP assay is much more sensitive and reliable than the MTT assay[135,136] and can provide useful information about cell functionality.

In this work, ATP levels were measured using the CellTiter-Glo 2.0 Assay (Promega Biosciences San Luis Obispo, CA, USA) according to the manufacturer's instructions. Cells were seeded at a density of 5×10^3 cells per well in a poly-L-lysine-coated white 96-well plate (Nunc) and after 48 hours they were treated with the photoactivatable compound. The ATP concentration was evaluated 3 hours and 24 hours after PDT treatment. Briefly, 50 μl of reagent was added to each well containing 50 μl of PBS. The solution was mixed for 5 minutes on an orbital shaker to induce cell lysis and then was left to incubate for 8 minutes protected from light. The luminescent signals were recorded with a microplate plate reader (Infinite F200, TECAN).

5.7.3 Hoechst 33342/Propidium Iodide (PI) Double Staining

The quantification of cell death using double staining with Hoechst 33342 and propidium iodide (PI) is a common method to assess cell viability based on membrane integrity and nuclear morphology.

Hoechst 33342 is a blue-fluorescent nuclear stain that binds to the minor groove of DNA with a preference for adenine-thymine (A-T) rich regions. This dye is cell-permeable and can stain the nuclei of both live and dead cells. Upon binding to DNA, Hoechst 33342 emits blue fluorescence, allowing visualization of nuclear morphology and revealing the gradients of nuclear damage. PI is a red-fluorescent DNA-binding dye that intercalates between the bases of DNA and is only taken up by cells with compromised membranes. Its fluorescence increases 20-30 fold upon binding, marking dead cells with red fluorescence. By combining these two dyes it's possible to distinguish between: live cells, which show blue-fluorescent nuclei, indicating intact membranes and no uptake of PI; necrotic or late apoptotic cells, whose nuclei exhibit both blue (Hoechst 33342) and red (PI) fluorescence, with red typically dominating due to the loss of membrane integrity; and early apoptotic cells, which display blue

fluorescence with Hoechst 33342, showing chromatin condensation and fragmented nuclei, without PI staining, as their membranes remain intact in the early stages of apoptosis.
In our experiments, cells were double stained with Hoechst 33342 (5 μg/ml) and PI (2 μg/ml) for 5 minutes in the dark, then analyzed using a Nikon Eclipse E400 microscope, as described previously[137].

5.8 Oxidative Stress Detection

Reactive oxygen species (ROS) production and elimination are part of a well-balanced physiological process called *redox signaling*. This process helps cells maintain steady-state levels of free radicals, which are crucial for various metabolic pathways. However, when cells experience extreme or prolonged stress, it can result in excessive ROS generation, potentially causing irreversible damage to biomolecules such as DNA, proteins, and lipids, ultimately leading to cell death[42,51]. Photoactive compounds are known to be stress inducers, making the assessment of ROS levels a valuable strategy to evaluate the impact of PDT on cancer cell metabolism. Among all radical species, hydrogen peroxide (H_2O_2) is the most stable and with the longest half-life in solution. Additionally, it can freely diffuse through cells membrane allowing its detection both directly in cell culture plate and in the culture medium[138].
To measure the ROS generated following PDT treatment, the ROS-Glo H_2O_2 assay (Promega Biosciences San Luis Obispo, CA) was employed. After irradiation, the culture medium was replaced with a solution containing a 125 μM dilution of H_2O_2 substrate dilution buffer in complete colture medium. The plates were then incubated for 3 hours at 37°C. Following incubation, 50 μl of the medium containing the H_2O_2 substrate was transferred from each well to a separate white plate. The ROS-Glo detection solution was added to each well to achieve a final volume of 100 μl. Luminescence signals indicating H_2O_2 levels in the samples, were recorded using a microplate reader (Infinite F200, TECAN).

5.9 Photodynamic Therapy of NSCLC Cells

Cells were seeded in poly-L-lysine-coated 96-well microplates (Thermo Fisher Scientific, Waltham, MA, USA) at a density of 5×10^3 cells per well. After two-days, the cells were treated with increasing concentrations of EITC-atezolizumab (0.5 μM, 1μM, 5 μM and 10 μM), and incubated for either 2 hours or 20 hours at 37°C protected from light. Control groups were treated with atezolizumab or eosin alone (at the highest concentration), or with EITC-atezolizumab under dark conditions (Figure 5.3A). All incubations were performed in phenol red-free and FBS-free medium, completed with 2% BSA to favor cell adhesion. Following treatment, cells were exposed to light for 60 minutes, corresponding to a light fluence of 51.8 J/cm^2 (unless explicitly mentioned otherwise), and then kept in a humidified environment with 5% CO_2 at 37°C, protected from light until further analysis. For the irradiation of cell cultures, the blue (458/25 nm) and green (523/40 nm) light of an RGB LED light source (Studio Par 64 CAN RGBWA+UV 12, Cameo, Anspach, Germany) was used. The irradiance at the surface of the

96-well plate was homogeneous and corresponded to 14.4 mW/cm^2, unless otherwise specified.

To validate the protocol and ensure the optimization and reliability of the experimental setup and conditions, we initially used the well-known PS hypericin. Our group has previously demonstrated its effectiveness in PDT treatments in other cancer cell models *in vitro*.[139].

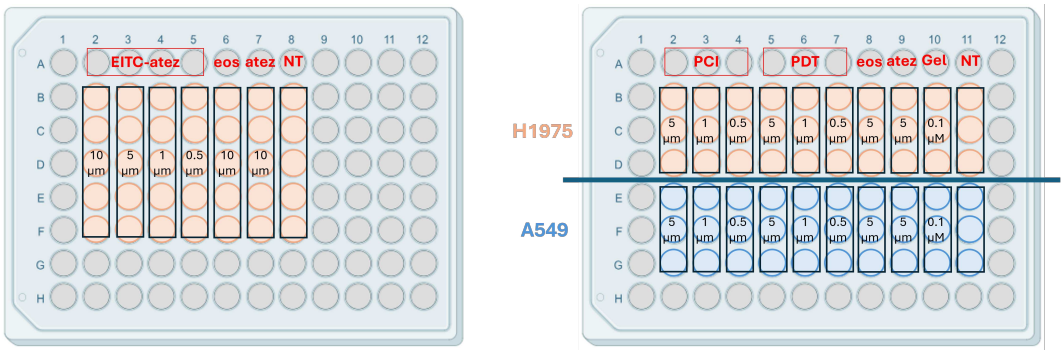

(A) *PDT Plate* **(B)** *PCI Plate*

Figure 5.3: Schema of the 96-well illuminated plates used for PDT (left) and PCI (right) experiments. Both plates were illuminated with the blue and green output of a RGB LED lamp for 60 minutes. A) Cells were incubated with increasing concentrations of EITC-atezolizumab for 2 hours or 20 hours and then illuminated. B) Cells were seeded on the same plate and treated in parallel. In PCI wells, EITC-atezolizumab was co-incubated with gelonin. PDT wells received EITC-atezolizumab only.

5.10 Photochemical Internalization of Gelonin

To build on our PDT experiments, we explored combining PDT with photochemical internalization (PCI) of the recombinant toxin gelonin to determine if this approach would yield improved results. These experiments were conducted at the Norwegian Radium Hospital (Department of Radiation Biology, Institute for Cancer Research, Oslo University Hospital).

Cells were seeded in 96-well plates (Nunc) at a density of 5×10^3 cells per well and left for overnight attachment. Two parallel experiments were performed, varying the light dose (illumination duration) or the concentration of EITC-atezolizumab. In the first case, cells were co-incubated with a fixed concentration of the complex (1 μM) and of the toxin (100 nM) for 20 hours, before being washed with complete medium and illuminated. Otherwise, cells were co-incubated with EITC-atezolizumab at increasing concentrations and gelonin (100 nM) for 20 hours, and then washed twice with complete medium to remove unbound antibodies before illumination. Subsequently, cells were irradiated for 60 minutes with a RGB LED light source (Studio par 64 CAN RGBWA+UV 12, Cameo, Anspach, Germany) emitting broadband blue and green light at 18.1 mW/cm^2. Cell viability was evaluated after 48 hours with the MTS assay, and the effects of PDT and PCI were compared. The schema of the irradiated plate is shown in Figure 5.3B. An identical plate was prepared to assess dark toxicity.

We also evaluated whether PD-L1 blockade affects the outcome of the treatment. For this purpose, we used atezolizumab in combination with the PS fimaporfin/TPCS$_{2a}$ to mimic a previously established

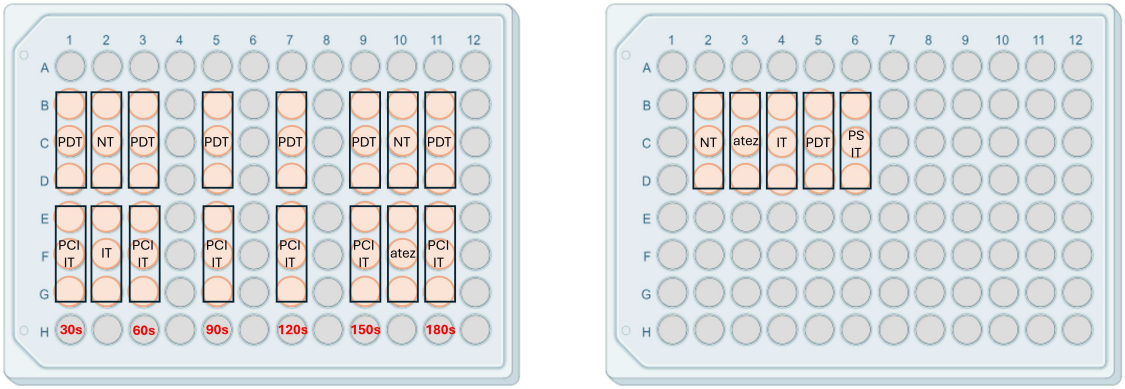

(A) *Irradiated Plate* **(B)** *Dark Plate*

Figure 5.4: Scheme of 96-well plates used in PCI experiments. A) In the irradiated plate: PDT refers to atezolizumab + $TPCS_{2a}$; PCI IT refers to atezolizumab + $TPCS_{2a}$ + gelonin; IT refers to gelonin alone. The plate was exposed to light for 0, 0.5, 1, 1.5, 2, 2.5 and 3 minutes, corresponding to a light fluence of 0, 0.26, 0.51, 0.77, 1, 1.3, and 1.5 J/cm^2. B) In the dark plate: PS IT refers to $TPCS_{2a}$ + gelonin.

PCI protocol[101]. Cells were seeded as described above, and then co-incubated with atezolizumab (1 μM, 5 μM or 10 μM) and $TPCS_{2a}$ for 20 hours. The PS was diluted to a final concentration of 0.2 μg/ml (in H1975) or 0.5 μg/ml (in A549) from a stock solution of 0.35 mg/ml in 50 mM Tris buffer pH = 8.5, 2.8% mannitol, and Tween 80. The following day, cells were washed twice with complete medium, and chased in PS-free medium for 4 hours to remove membrane-bound $TPCS_{2a}$. Gelonin (100 nM) was added during the chase period, and then replaced with fresh medium before illumination. Cells were exposed for 0, 0.5, 1, 1.5, 2, 2.5 and 3 minutes to the blue light output of the LumiSource lamp (PCI Biotech AS, Oslo, Norway). The lamp emits in the range 400-500 nm, with a maximum at λ_{max} = 435 nm, and an homogenous irradiance of $\approx$ 8.5 mW/cm^2 across the all area. Cytotoxicity was finally measured by the MTS assay 48 hours after light exposure. Scheme of the illuminated and dark plate are shown in Figure 5.4.

Chapter 6

Results and Discussion

6.1 The EITC-atezolizumab Complex for PDT and PCI

6.1.1 General Photophysical Properties of EITC-atezolizumab

Photophysics of the EITC-atezolizumab complex was investigated using time-resolved and steady-state optical spectroscopies. In this work, the photosensitizer (PS) EITC was dissolved in DMSO to obtain a high concentrated PS stock (> mM). DMSO is a convenient solvent for this type of applications because it can be easily mixed with PBS and concentrations up to 10% (v/v) are well tolerated for a protein, without denaturation taking place. The conjugation between EITC and atezolizumab was performed in PBS buffer at pH = 7 to prevent the aggregation of the antibody at higher pH, which might be explained by its aglycosylated state[120]. As previously reported, the position of the absorption band of eosin and its derivatives is influenced by the polarity of the solvent[128], a phenomenon called *solvatochromism*. For example, a red shift of the maximum peak occurs when changing the buffer from PBS to DMSO[22]. Considering the absorbance spectra reported in Figure 6.1A, EITC exhibits a strong absorbance in the green region of the visible spectrum, with a primary absorbance peak around 522 nm in PBS buffer. When bound to atezolizumab, the peak slightly shifts to 525 nm. A smaller absorbance band falls in the UV range, corresponding to the main absorbance band of the antibody. The contribution of EITC at 280 nm must therefore be taken into account when calculating the molar concentration of atezolizumab, modifying the Lambert-Beer law as follow:

$$A_{atez}(280nm) = A(280nm) - [A_{EITC}(524nm) \times 0.28] \tag{6.1}$$

where CF = 0.28 is the correction factor of eosin at 280 nm.

The degree of labeling (DOL) of atezolizumab, defined as the average number of EITC molecules conjugated to each antibody, can be determined as the ratio [EITC]/[atezolizumab] (equation 5.2). Using 95,000 $M^{-1}cm^{-1}$ and 232,400 $M^{-1}cm^{-1}$ as molar absorption coefficients for EITC and atezolizumab, respectively, in our preparation the DOL was approximately 2.5.

Conjugation to the antibody does not dramatically alter EITC's fluorescent properties, as also observed

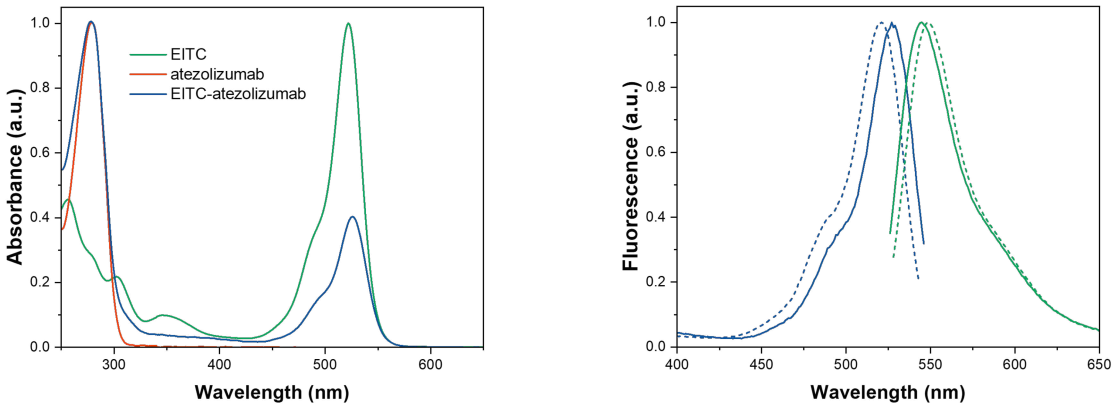

(A) *Absorption Spectra* **(B)** *Excitation/Emission Spectra*

Figure 6.1: Absorption, excitation and emission spectra of EITC and EITC-atezolizumab. A) Absorption spectra of EITC (green), atezolizumab (red) and the EITC-atezolizumab complex (blue) in PBS buffer at pH = 7. The spectra are normalized at 522 nm (EITC) or at 280 nm (atezolizumab alone or bound to EITC). B) Normalized fluorescence excitation (blue, λ_{em} = 550 nm) and emission (green, λ_{ex} = 520 nm) spectra of EITC-atezolizumab (solid lines) and EITC (dashed lines) in PBS buffer at pH = 7.

with streptavidin at low DOL[22]. After binding, the emission spectrum of EITC shows minimal changes, while its excitation spectrum still closely resembles its absorption spectrum (6.1B). Despite the stability in the spectral behavior, the fluorescence quantum yield, Φ_F, is affected by the conjugation. It is well established that the Φ_F of a sample can be estimated by comparison with a molecule of known quantum yield[30]. Using eosin in PBS as a reference (Φ_F = 0.24[123]) and applying equation 5.3, the estimated quantum yield of EITC-atezolizumab was determined to be Φ_F = 0.11. In comparison, the quantum yield of free EITC in PBS is 0.18[22], indicating a slight reduction in fluorescence efficiency upon conjugation. One possible explanation is that EITC may act as a quencher, where interactions between EITC molecules lead to a decrease in fluorescence emission. However, due to the low DOL, this event is unlikely. Similarly, aggregation of EITC in solution was excluded. We concluded that fluorescence quenching results from interactions between EITC molecules and amino acid residues within the antibody to which the PS is bound.

Finally, the formation of a stable conjugate between EITC and atezolizumab was proved by steady-state fluorescence anisotropy and fluorescence lifetime measurements. Fluorescence excitation anisotropy provides information on the rotational diffusion of a system during the interval between the absorption of polarized light and subsequent fluorescence emission. Free diffusing fluorophores in solution quickly rotate, reorienting their transition dipole several time within their fluorescence lifetime. When they are linked to a macromolecule, the rate of the rotational diffusion decreases due to the bigger size of the system. Therefore, the emitted fluorescence will be polarized (i.e., the anisotropy will be non-zero) only when the fluorophore holds a preferential orientation, such as when it is bound to a protein which reduces its rotational freedom. As shown in Figure 6.2A, the fluorescence anisotropy of EITC

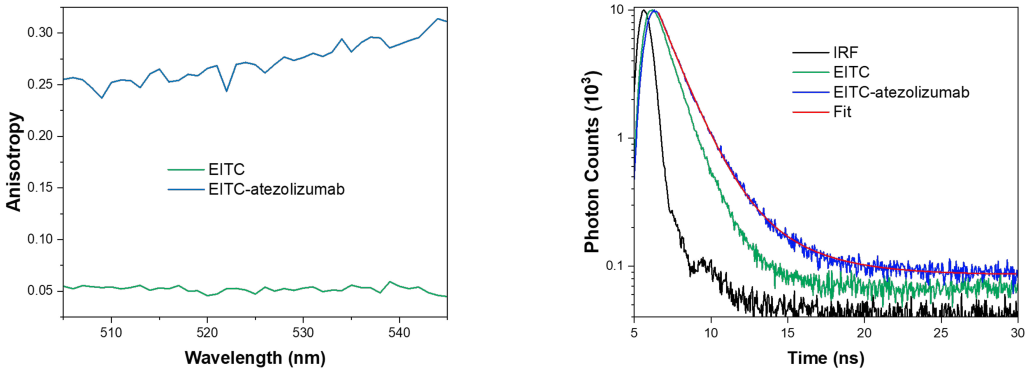

(A) *Anisotropy Spectra* **(B)** *Fluorescence Decays*

Figure 6.2: Anisotropy spectra and fluorescence decays of EITC (green) and EITC-atezolizumab (blue) in PBS buffer. A) Fluorescence excitation anisotropy spectra collected at 550 nm. The samples were excited between 505 and 545 nm with 1 nm excitation bandwidth. B) Fluorescence lifetime decays acquired using a TCSPC system at an excitation wavelength of 500 nm and an emission wavelength of 550 nm. IRF (black) and the exponential fit of the decay of EITC-atezolizumab (red) are also shown.

in PBS is negligible, while the anisotropy of the conjugate varies from 0.25 to 0.31 between 500 and 550 nm, where the PS has its maximum absorption. This result provides a clear indication of the successful binding between EITC and atezolizumab. An additional evidence of the formation of the EITC-atezolizumab complex is given by fluorescence decay time curves. For both free EITC and EITC bound to atezolizumab in PBS buffer, the lifetime decays were measured by exciting the sample with a pulsed LED emitting at 500 nm, and collecting the fluorescence signals at 550 nm. Fluorescence lifetimes were then extrapolated by performing the re-convolution between a proper exponential fitting function and the instrument response function (IRF). Representative lifetime decays are reported in Figure 6.2B. Fluorescence decay of EITC is well-described by a mono-exponential function, with a lifetime of τ = 1.16 ± 0.01 ns, consistent with our previous observation[22] and with the lifetime of free eosin in solution, equal to 1.21 ns[123]. Conversely, the fluorescence emission of the EITC-atezolizumab complex is best fitted by a bi-exponential function and occurs with a mean lifetime of τ_{mean} = 1.31 ± 0.03 ns, slightly longer than the one associated to the PS alone (Table 6.1). These results represent a conclusive proof of the binding between EITC and atezolizumab to form a stable complex.

	τ (ns)	Φ_F
Eosin	1.21[123]	0.24[123]
	1.231 ± 0.003[22]	
EITC	1.16 ± 0.01	0.18 ± 0.02[22]
	1.117 ± 0.003[22]	
EITC-atezolizumab	1.31 ± 0.03	0.11 ± 0.01

Table 6.1: Fluorescence lifetimes of eosin, EITC, and EITC-atezolizumab in PBS buffer.

6.1.2 Triplet State Formation and Singlet Oxygen Production

To effectively carry out its photosensitizing activity, EITC must preserve its ability to undergo intersystem crossing and generate $^1O_2$ efficiently, even when bound to atezolizumab. Therefore, the quantum yields of triplet state formation, Φ_T, and singlet oxygen generation, Φ_Δ, for the EITC-atezolizumab complex were measured.

Using a homemade LFP setup[129], the samples in PBS were photoexcited at 532 nm to induce the formation of a transient triplet state, whose evolution was monitored by probing the conjugate and free EITC at 522 nm and 526 nm, respectively.

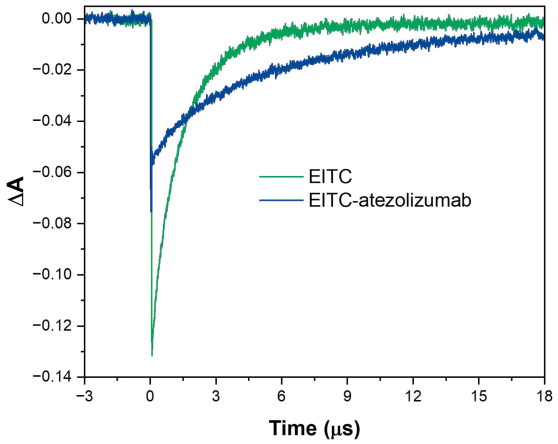

Figure 6.3: Transient absorption curves for EITC (green) and the EITC-atezolizumab complex (blue) at 522 nm and 526 nm, respectively. Excitation was performed at 532 nm.

The transient absorption spectra, shown in Figure 6.3, exhibit a decrease in absorbance in the ground state region immediately following excitation, indicative of ground state depletion. Concurrently, an increase in absorbance is observed in the triplet state region, reflecting its formation. The changes in absorbance (ΔA) are more pronounced for free EITC than for the complex, suggesting that the binding to the antibody reduces the efficiency of triplet state formation while simultaneously increasing the triplet state lifetime. As the triplet state decays over time, the absorbance associated with the ground state gradually recovers. This recovery phase allows for the determination of the triplet state's

	τ_1 (μs)	A_1	τ_2 (μs)	A_2
Eosin	2.0 ± 0.1[22]			
EITC	2.2 ± 0.1 2.1 ± 0.1[22]			
EITC-atezolizumab	4.16 ± 0.02	63%	15.5 ± 0.1	37%

Table 6.2: Lifetime of the triplet state of eosin, EITC, and EITC-atezolizumab in PBS buffer (pH = 7).

lifetime by fitting the recovery portion of each signal with an appropriate exponential model. In our measurements, the kinetic of EITC in PBS is well-described by a monoexponential decay with a lifetime of 2.2 ± 0.1 μs, consistent with our previous results[22]. In contrast, the kinetic of the EITC-atezolizumab complex is better described by a bi-exponential decay (Table 6.2). This longer lifetime suggests that the protein exerts a shielding effect, protecting the PS from interaction with oxygen diffusing in solution. Using the data retrieved from the transient absorption curves and applying equation 5.6, we estimated the triplet quantum yield of the EITC-atezolizumab complex to be 0.20 ± 0.05, a value lower than the quantum yield of free EITC in PBS, which is 0.49[22]. This result is consistent not only with the observed decrease in triplet state formation efficiency, but also with the possibility that the PS binds to a region of the protein rich in aromatic amino acids, which are known to readily quench the triplet state. A similar quenching effect was observed in our previous studies with EITC bound to streptavidin (Φ_T = 0.1), although this did not significantly impair the PS's ability to generate $^1O_2$ and kill bacteria cells[22].

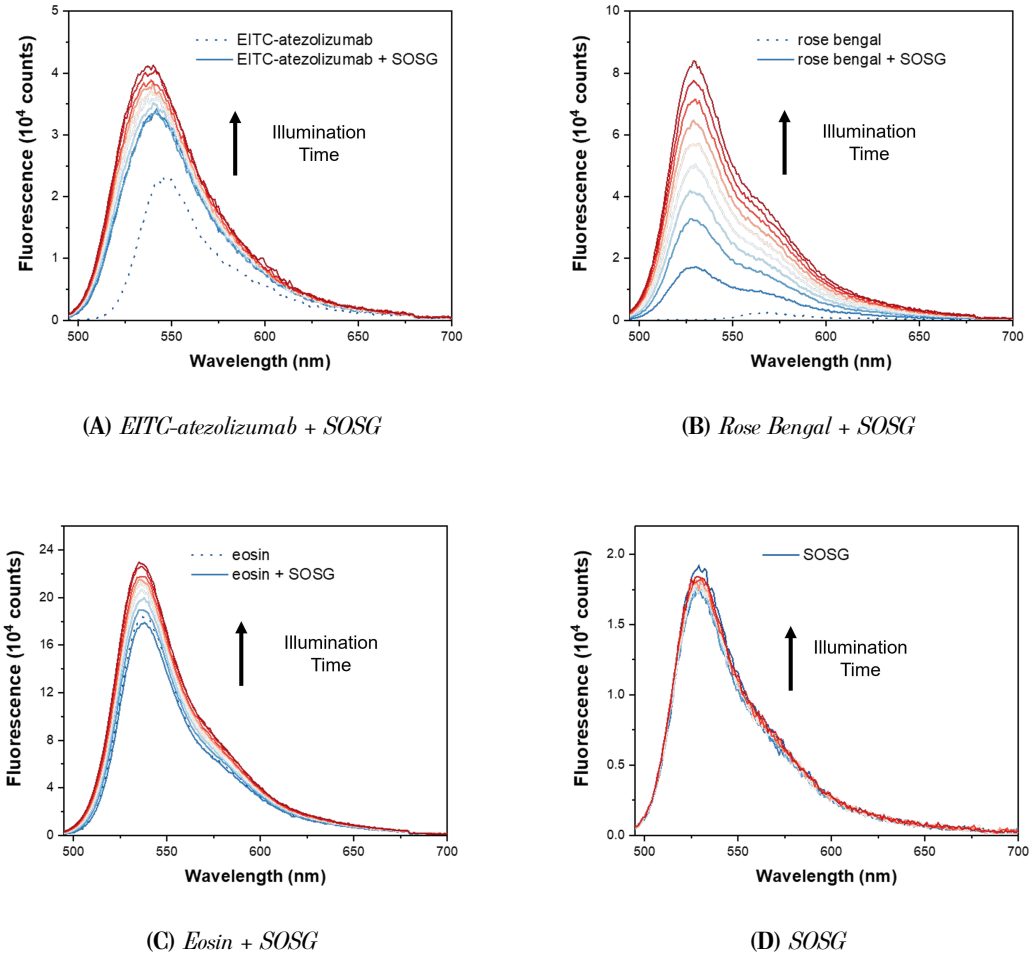

Figure 6.4: Fluorescence emission spectra of SOSG in solution, in the presence of EITC-atezolizumab (A), rose bengal (B), eosin (C), or alone (D) at increasing illumination times (blue to red: 0, 20, 40, 60, 80, 100, 120, 140, and 160 seconds). The $^1O_2$ produced upon irradiation increases the fluorescence intensity of SOSG, which serves as an indicator of $^1O_2$ levels in the solution. The increase in fluorescence intensity is directly proportional to the amount of $^1O_2$ generated over time.

The estimation of $^1O_2$ quantum yield, Φ_Δ, for the EITC-atezolizumab complex was obtained using the fluorescent probe SOSG by comparison with eosin and rose bengal. Firstly, SOSG fluorescent probe was used to calculate the Φ_Δ of eosin in PBS, using rose bengal as reference (which has a known Φ_Δ of 0.76[126]) obtaining a value of 0.65. Then, the fluorescence emission spectra of SOSG in the presence of EITC-atezolizumab, eosin, or rose bengal were collected before and after irradiating the samples at 532 nm. For EITC-atezolizumab, eosin, and rose bengal the fluorescence intensity increases with longer illumination times, reflecting the amount of $^1O_2$ generated upon the irradiation of the PS, while a minimal increment is observed for SOSG alone (Figure 6.4). Finally, the emission intensities of rose

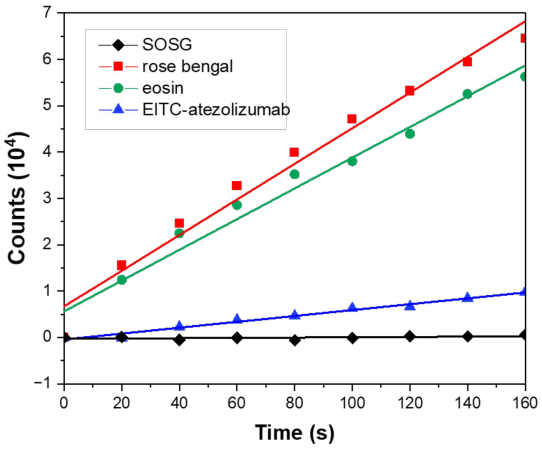

Figure 6.5: Variation of fluorescence emission of SOSG in the presence of rose bengal (red), eosin (green), EITC-atezolizumab (blue), or alone (black) as a function of illumination time.

bengal, eosin, and the EITC-atezolizumab complex were plotted against illumination time and data were fitted to a linear model to determine the slope of the curve for each sample (Figure 6.5). According to equation 5.7, we obtained a quantum yield of 0.11 ± 0.02 for the EITC-atezolizumab complex in PBS buffer. Although this value is lower compared to that of free eosin, which has a Φ_Δ value greater than 0.5[140], it remains sufficiently high for further evaluation of the immunoconjugate in PDT applications. Interestingly, the Φ_Δ for the complex is also lower than its triplet quantum yield. This observation might indicate that while the protein partially shields the PS from oxygen, it does not entirely prevent $^1O_2$ formation[141]. Additionally, the quenching of $^1O_2$ by amino acids in the antibody likely contributes to further decrease the quantum yield.

6.2 The AF647-atezolizumab Complex for Imaging

Alexa Fluor 647 (AF647) is a far-red fluorescent dye widely used in biological research and microscopy due to its desirable photophysical properties. In this study, we conjugated the AF647 dye, in the form of its amine-reactive N-hydroxysuccinimidyl ester, directly to atezolizumab, in order to mimic the supramolecular EITC-atezolizumab complex used in PDT experiments. The dye exhibits a well-defined

absorption spectrum, with a single prominent peak at around 650 nm. The binding of AF647 to atezolizumab does not drastically alter its absorption maximum, even though a slightly blue-shift occurs due to the interactions with the protein (Figure 6.6A). AF647 has a molecular weight of 1250, a molar extinction coefficient of 270,000 M^{-1} cm^{-1} at 650 nm, and a correction factor of 0.03 at 280 nm. These parameters were used to calculate the concentration of atezolizumab from the absorption spectrum and its degree of labeling. As for EITC, we obtained an average DOL of 2.5.

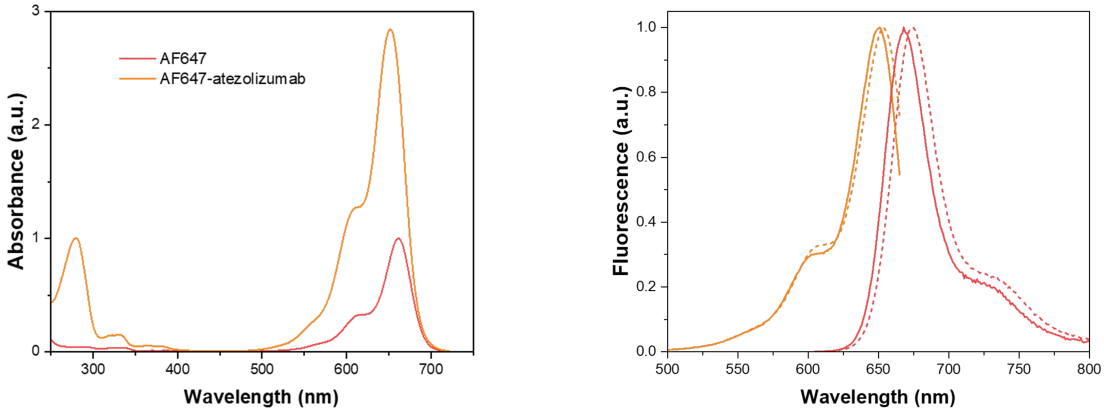

(A) *Absorption Spectra* **(B)** *Excitation/Emission Spectra*

Figure 6.6: Absorption, excitation, and emission spectra of AF647 and AF647-atezolizumab. A) Absorption spectra of AF647 (red) and AF647-atezolizumab (orange) in PBS buffer. Spectra are normalized at 652 nm (AF647) or at 280 nm (AF647-atezolizumab). B) Normalized fluorescence excitation (λ_{em} = 670 nm) and emission spectra (λ_{ex} = 600 nm) of AF647-atezolizumab (solid lines) and AF647 (dashed lines) in PBS buffer.

Even though we proved EITC effectiveness as a PS for developing highly specific immunoconjugates, its relative week fluorescence limits its utility for microscopy. In contrast, AF647 offers significantly higher brightness (Φ_F = 0.33 in PBS), and exhibits minimal photobleaching due to its high photostability. Additionally, AF647 supports multicolor imaging due to its compatibility with various other fluorophores and can be effectively excited using standard lasers in the red to far-red spectrum (around 652 nm). The excitation and emission spectra of AF647 (both free and conjugated to atezolizumab) are reported in Figure 6.6B.

6.3 Counting of PD-L1 Receptors

Targeted PDT relies on the interaction between a photoactive compound and specific receptors or molecules on the target cells. The effectiveness of the treatment can depend on several factors, including how many receptors are available for the compound to bind to. Estimating receptor density, however, can be challenging, due to the complexity of the receptor system and the inherent biological variability among cells and tissues. Receptors are not static; they can undergo internalization, recycling, or downregulation, thus their density on the membrane can change over time[142]. Moreover, receptor

density can differ significantly across various cell types and tissues. Another challenge is the small size of the receptors, typically on the order of nanometers, which makes their accurate measurement difficult with many conventional imaging techniques due to their limited spatial resolution. At present, various biological assays are used to estimate receptor density *in vitro*. However, they often rely on indirect methods, such as detecting receptors in cell lysates or supernatants with antibodies rather than directly measuring receptors on intact cells (e.g., western blotting and ELISA), they might lack of sensitivity and specificity, and they are quite sensitive to the sample preparation. Among these methods, flow cytometry is considered one of the most reliable techniques for evaluating receptor expression on both live and fixed cells. This technique allows for the rapid quantification of cell surface receptors by passing cells through a laser beam and detecting fluorescence from labeled antibodies specific to the receptors of interest. The main drawback of flow cytometry is that it provides relative, rather than absolute, receptor density values, requiring repeated measurements for accurate comparisons between different cell lines. To overcome this limitation, here we propose a quantitative approach based on direct stochastic optical reconstruction microscopy (dSTORM) to detect and quantify PD-L1 membrane receptors with single-molecule resolution. This method should provide more reliable insights into PD-L1 receptors organization and distribution compared to flow cytometry results.

H322 and A549 are both human primary NSCLC adenocarcinoma cell lines, chosen for expressing PD-L1 at different levels. H322 cells are known for their high PD-L1 expression, whereas A549 cells exhibit such low levels of PD-L1 that they are frequently classified as negative for this protein[118]. To further validate our results, we also included in the study human dermal fibroblasts (HuDe) cells derived from human skin tissue. HuDe cells typically have low or negligible PD-L1 expression compared to cancer cells, but a recent study has suggested that PD-L1 can be found also in non-hematopoietic normal cells[143]. Both flow cytometry and dSTORM analysis were conducted on the three selected cell types, and results were compared to provide a more comprehensive understanding of PD-L1 expression on the cell surface.

6.3.1 Staining of PD-L1 Receptors

PD-L1 receptors were visualized with dSTORM. After fixation, cells were incubated with a primary monoclonal antibody specific to PD-L1 and subsequently with an AF647-labelled secondary antibody. To preserve membrane integrity and ensure specific staining of surface receptors, permeabilization was avoided. Then, cells were imaged in TIRF mode to display only the receptor exposed on the surface of the cell basal membrane. This modality involves directing a laser beam at the glass-sample interface at an angle greater than the critical angle, so that the beam is totally reflected and penetrates only a few hundred nanometers into the sample. This localized illumination allows for the selective excitation of fluorophores close to the surface, dramatically increasing the signal-to-noise ratio.

The visual inspection of the dSTORM images in Figure 6.7 suggests a substantial difference in PD-L1

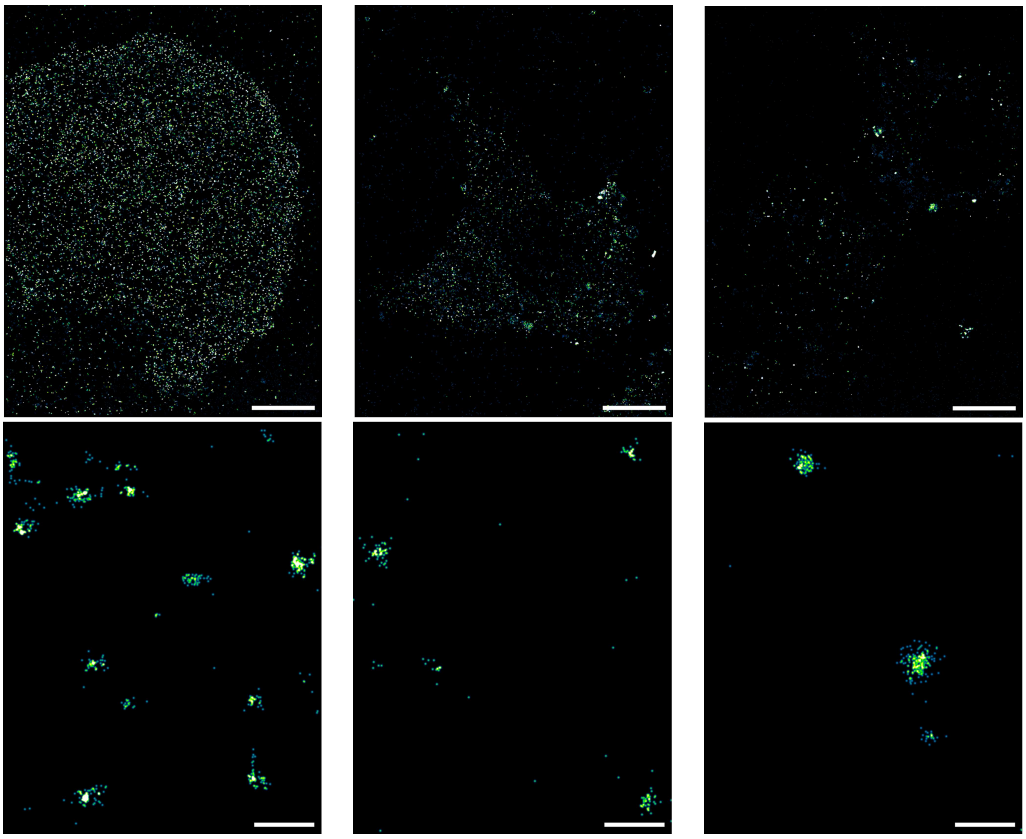

(A) *H322 Cells* **(B)** *A549 Cells* **(C)** *HuDe Cells*

Figure 6.7: dSTORM images of H322 (A), A549 (B) and HuDe (C) cells incubated with an anti-PD-L1 antibody and an AF647-labelled secondarya antibody. Images were collected in TIRF mode. Scale bar: 10 μm. Bottom images are zoom of the corresponding top images to highlight the organization of PD-L1 receptors at the nanoscale. Scale bar: 0.3 μm. Modified from Alampi et. al[110].

expression levels among the three cell types. H322 cells exhibit the highest PD-L1 expression with a relatively uniform distribution of the receptors across the membrane. In contrast, A549 and HuDe cells show lower PD-L1 levels, although the fluorescence signals remain detectable. To confirm that the fluorescence signal originates from the membrane, we focused the laser in a central section of the cell and we acquired super-resolved images in HILO mode, which allows deeper sample penetration. As expected, no fluorescence signals from the nucleus or cytoplasm were observed (Figure 6.8). Additionally, to ensure the specificity of the anti-PD-L1 antibody, we conducted a control experiment with only the secondary antibody. This control helped to identify any non-specific binding of the polyclonal antibody to the sample or glass, which could otherwise increase background signal and lead to misinterpretation of the data. The negligible signal from the secondary antibody alone confirms that the observed fluorescence is due to the specific interaction between the primary antibody and PD-L1 receptors.

A closer look at dSTORM images in Figure 6.7 reveals the presence of localization clusters of approximately 100-200 nm in size. This suggests that PD-L1 receptors may organize into nanoclusters on the membrane surface, although a detailed investigation into their nanoscale distribution is beyond the scope of this study. However, this observation is in agreement with previous studies[144,145], and open

interesting possibilities for future research.

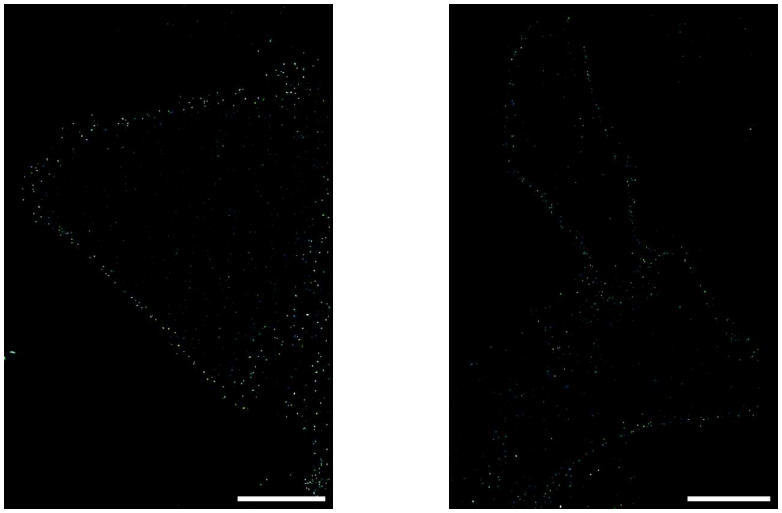

(A) *H322 Cells* **(B)** *A549 Cells*

Figure 6.8: Images of PD-L1 receptors on the membrane of H322 (A) and A549 (B) cells collected with dSTORM microscopy using HILO illumination. Scale bar: 10 μm.

6.3.2 Results of Flow Cytometry Analysis

Flow cytometry experiments were carried out at the Department of Medicine and Surgery (University of Parma) with the CytoFLEX Flow Cytometer (Beckman Coulter Life Sciences, Indianapolis, IN, USA). We followed a standard protocol in which phycoerythrin (PE) isotype was used as negative control to assess the level of non-specific binding and background fluorescence. After harvesting, 5×10^5 cells were incubated with either an anti-PD-L1 antibody conjugated to PE or PE isotype in PBS + 0.5% BSA for 30 minutes on ice in the dark. Following incubation, cells were washed with cold PBS + 0.5% BSA and resuspended in the same buffer for the analysis. Data were analyzed using the Beckman Coulter's Kaluza software (v2.2) and presented as the fold increase in median fluorescence intensity (MFI) relative to the corresponding isotype control (Figure 6.9A). Based on these results, PD-L1 expression in H322 cells is $\sim$ 12-fold higher than in A549 cells (14 ± 5 vs 1.2 ± 0.2) and $\sim$ 13-fold higher than in HuDe cells (14 ± 5 vs 1.1 ± 0.1). Student's t-test was conducted to determine whether the minimal observed differences in MFI between A549 and HuDe cells were statistically significant. However, no differences emerged between the two models ($p > 0.05$).

Although our flow cytometry data confirmed that PD-L1 expression is low in A549 and HuDe cells, we have raised concerns about the adequacy of the negative isotype control used in these experiments. Despite being commonly used to assess non-specific binding of antibodies and to set thresholds for positive staining, isotype controls may not fully represent the binding characteristics of the primary antibody. This is because they do not possess the specific antigen-binding sites of the primary antibody, potentially failing to account for interactions that occur in the absence of specific antigen recognition,

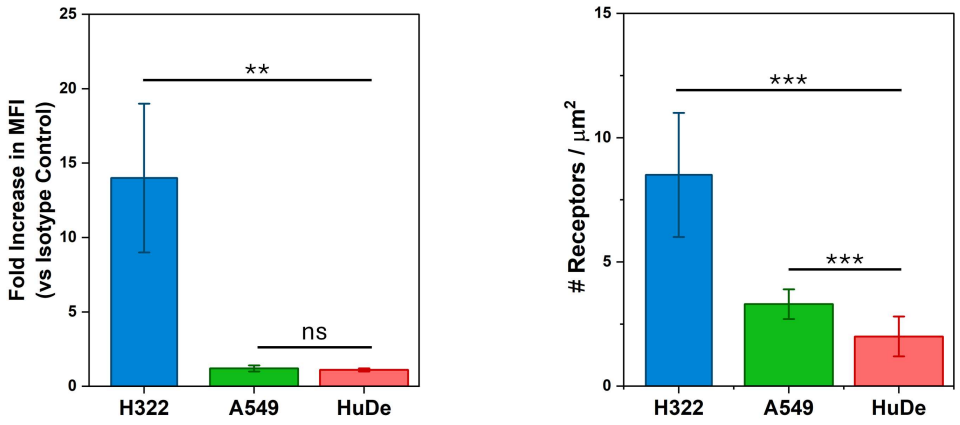

(A) *Flow Cytometry Results* **(B)** *dSTORM Results*

Figure 6.9: Comparison of flow cytometry and dSTORM analysis to assess PD-L1 expression levels of H322, A549, and HuDe cells. A) Flow cytometry results. PD-L1 surface levels are expressed as fold increase in MFI versus the corresponding isotype control. Data are mean values ± SD of at least three independent experiments. **: $p < 0.01$, ns: not significant vs HuDe cells. B) dSTORM results. Quantification of PD-L1 receptors per μ^2 exposed on the surface membrane of the cells. In total, a minimum of 10 cells were analyzed per cell type. ***: $p < 0.001$ vs HuDe cells. Recreated from Alampi et. al[110].

which can result in an inaccurate assessment of background fluorescence[146]. For this reason, we developed a quantitative approach based on the single-molecule detection of PD-L1 receptors with dSTORM to validate the flow cytometry results.

6.3.3 Results of dSTORM Analysis

The analytical workflow for dSTORM imaging analysis is illustrated in Figure 6.10.

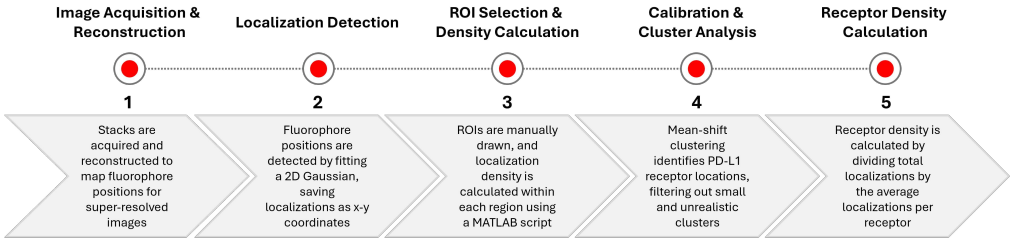

Figure 6.10: Workflow for PD-L1 quantification in dSTORM imaging.

Briefly, PD-L1 receptors were labeled using the indirect immunostaining approach described in Section 5.5.2, employing a primary anti-PD-L1 antibody followed by a secondary antibody conjugated to AF647. Multiple fields of view were imaged to obtain a comprehensive overview of the entire sample, and ensure robust statistical analysis. We calculated the localization density for the selected ROIs (each corresponding to a single cell) with a custom MatLab script. However, this density does not directly reflect the number of receptors present, as each primary antibody used in the immunostaining process can bind multiple secondary antibodies, which in turn are conjugated to multiple fluorophores.

Additionally, a single fluorophore might blink several times during acquisition, producing multiple localizations. To convert dSTORM localization density into receptor density, we employed a calibration method on images acquired using low-concentration primary antibody staining on H322 cells. Then, a mean-shift algorithm was applied to the calibration images to identify clusters of receptors. This way, we were able to identify individual labeled receptors, and quantify the number of localizations per PD-L1 by fitting the histogram of the cluster distribution (Figure 6.11). We obtained an average of 14.3 localizations per cluster. Dividing the localization density to this number we estimated the number of receptors per area. The histogram in Figure 6.9B shows PD-L1 density (# receptors/μm^2) of H322, A549, and HuDe cells compared to the corresponding negative control with the secondary antibody only. Consistent with flow cytometry results, H322 cells exhibit the highest PD-L1 expression levels

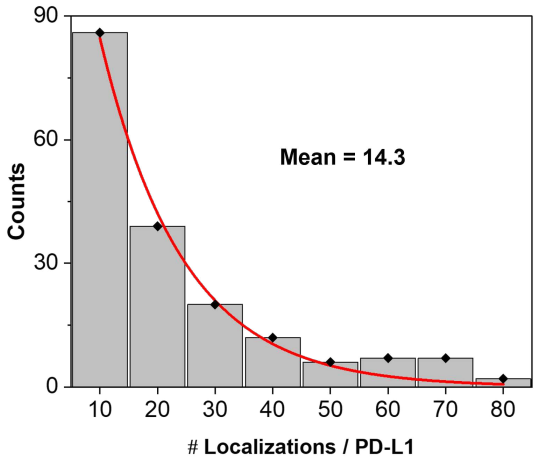

Figure 6.11: Histogram of the cluster distribution representing the number of localizations per single PD-L1 receptor on H322 cells. Receptors were stained with low concentration of primary antibody. The histogram was fitted with a mono-exponential decay function to extrapolate the mean. From Alampi et. al[110].

among the three models, followed by A549 cells and, lastly, HuDe cells. Specifically, H322 cells have an average PD-L1 receptor density of 8.5 ± 2.5 PD-L1/μm^2 , A549 cells show an average density of 3.3 ± 0.6 PD-L1/μm^2, and HuDe cells display the lowest average density of 2.0 ± 0.8 PD-L1/μm^2. Large error bars reflect the inherent variability between cells in the biological sample, where some cells may express higher/lower levels of PD-L1 compared to the others, despite originating from the same culture. These values are in excellent agreement with those reported independently by two other research groups, one that has estimated PD-L1 expression levels on HCC827 NSCLC cells[145] and the other which measured CD19 expression on myeloma cells[147], both using similar approaches. On the contrary, they are substantially lower compared to the reported values for other receptors such as EGFR[6,148]. However, it has to be considered that often receptor levels are induced or manipulated in cell lines used for research and may not reflect the levels of membrane receptors endogenously expressed on the cells. Moreover, other factors including variations in receptor-dye stoichiometry, non-specific background noise, potentially incomplete labeling of receptors on the basal membrane, and

inherent analytical imperfections can contribute to increase uncertainty. Nevertheless, they serve as a valuable quantitative parameter for evaluating the effectiveness of delivery systems and developing personalized therapies.

6.3.4 Final Considerations

For effective PIT clinical outcomes, it is essential to determine the density of target receptors on cell membranes. Flow cytometry, together with immunohistochemistry, is widely used to detect and measure fluorescently labeled antibodies specific to target receptors, in order to compare receptor expression levels between various cell types. However, these techniques have limitations in providing absolute quantitative results, and comparisons across different cell lines or experiments can be challenging due to variations in experimental conditions and instrument settings. In this context, dSTORM super-resolution microscopy can offer significant advantages including the possibility to precisely localize and quantify receptors on the membrane surface[6] and visualize their distribution at the nanoscale[149]. In this work, dSTORM's high single-molecule sensitivity allowed for the detection of PD-L1 expressed at a very low level on both A549 and HuDe cells. In flow cytometry data analysis, the difference in PD-L1 expression between A549 and HuDe cells was not statistically significant, likely because the PD-L1 levels were too low to be detected reliably, leading to both cell types being classified as negative. Qualitative observation of dSTORM images already suggested the presence of PD-L1 receptors on A549 cells at very low levels, justifying further investigations. This observation was eventually confirmed through quantitative analysis, demonstrating that A549 cells, unlike HuDe cells, do express PD-L1 and can be used in PDT experiments to assess treatment efficacy even with minimal receptor expression. In conclusion, we proposed a versatile and efficient method to count membrane receptors on intact cells. Although this approach likely underestimates the actual receptor density due to incomplete labeling of receptors or incomplete detection of fluorophores, it provides absolute quantification of PD-L1 membrane receptors, making it straightforward to compare receptor levels across different cell lines. Furthermore, the method is adaptable to different receptors and fluorophores, as long as they are compatible with dSTORM imaging. Discrepancies between flow cytometry and dSTORM results can be attributed to intrinsic technical differences in data acquisition, sample preparation and sensitivity, as well as potential partial immunolabeling of PD-L1 receptors on the basal membrane[148].

6.4 Binding of Atezolizumab to PD-L1 Receptors

To deliver its therapeutic action, atezolizumab must bind to PD-L1 receptors and carry the PS sufficiently close to the basal membrane to cause effective damage upon excitation. However, conjugation with a fluorophore can impact atezolizumab's binding capability by altering the protein's conformation or steric properties, potentially affecting its affinity or specificity for the target. Therefore, it was crucial

to evaluate whether atezolizumab retains its ability to bind PD-L1 after conjugation with EITC. Due to the weak fluorescence of EITC when bound to the antibody ($\Phi_F = 0.11$), we used the brighter fluorophore AF647 as a substitute for the PS. We assumed that the results for the AF647-atezolizumab complex could be extended to the EITC-atezolizumab complex, as both dyes likely interact with the same residues on the antibody. Additionally, we ensured that both conjugates had the same DOL to maintain similar steric hindrance, despite AF647 having a slightly higher molecular weight compared to EITC.

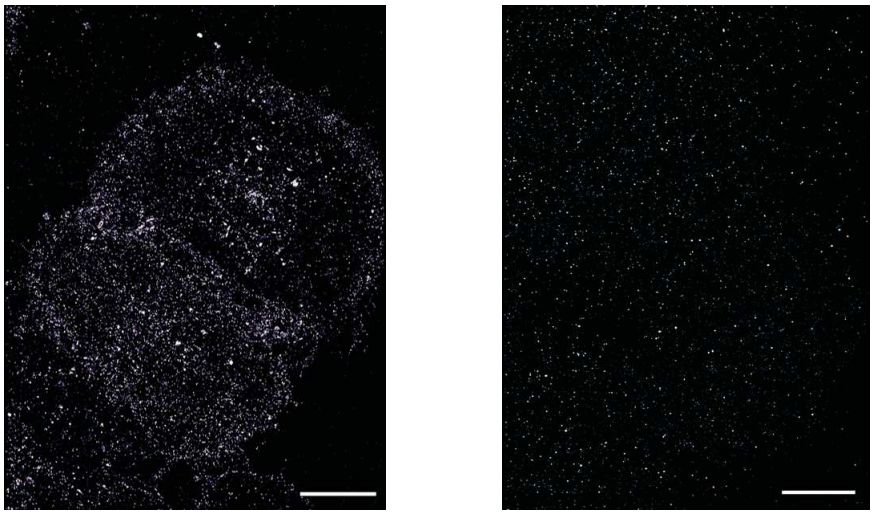

(A) *dSTORM Image with AF647-atezolizumab*

(B) *Control Image with AF647-IgG*

Figure 6.12: Representative dSTORM image of PD-L1 receptors on the membrane of H322 stained with atezolizumab directly conjugated to AF647 (A). Control images were collected incubating the cells with an AF647-labelled IgG (B). Scale bar: 10 μm. From Alampi et. al[110].

For this study, we selected H322 cells as the model system because they exhibit the highest PD-L1 expression among the cell lines tested, ensuring the optimal conditions for evaluating atezolizumab's binding to PD-L1. PD-L1 receptors were stained with AF647-atezolizumab and the fluorescence signal from the basal membrane was collected using a TIRF configuration. A representative dSTORM image of H322 cells is shown in Figure 6.12A. To confirm the specificity of the PD-L1/atezolizumab binding, control experiments were performed using an AF647-labelled IgG to evaluate non-specific binding. Since any significant fluorescence was observed (Figure 6.12B), we concluded that atezolizumab-based complexes specifically target PD-L1.

6.5 Photodynamic Therapy of NSCLC Cells

PDT was performed using the EITC-atezolizumab immunoconjugate on three distinct cell lines expressing PD-L1 at different levels to demonstrate the photodynamic activity of the complex and evaluate the likely correlation between the therapeutic outcome and PD-L1 density on the cell membrane. For

this purpose, H1975, H322 and A549 cell lines were selected. The experiments were conducted in collaboration with the Department of Medicine and Surgery (University of Parma) and the Department of Radiation Biology of the Institute for Cancer Research in Oslo (Norwegian Radium Hospital, Oslo University Hospital). In both laboratories, the same experimental protocol was used (with the only variation being the duration of the incubation period of the complex) in order to establish the PS dose-dependent effects on cell viability due to PDT. Another critical factor in determining the treatment response is the amount of ROS generated immediately after the photoactivation of the PS. ROS are essential for normal cellular functions and signaling; however, their excessive accumulation can cause severe oxidative damage and disrupt cellular homeostasis, leading to cell death[42]. Therefore, in addition to cell viability, we measured the production of ROS in irradiated cells.

6.5.1 Validation of the Protocol: Hypericin-Mediated PDT

To validate the efficacy of our procedure and establish the optimal culture conditions for PDT, we conducted experiments using hypericin on H322 lung carcinoma cells.

Hypericin is a naturally-occurring drug that exhibits preferential binding to cell membranes due to its affinity for lipid-rich regions. When dissolved in polar organic solvents, hypericin becomes photoactive, with high quantum yields of fluorescence (Φ_F = 0.35) and singlet oxygen generation (Φ_Δ = 0.33)[150]. These properties make hypericin an excellent candidate as photosensitizing agent for PDT, where $^1O_2$ is a key mediator of oxidative stress and subsequent cell death. Additionally, its photodynamic activity has been confirmed in a variety of biological systems, including cancer cells[139], bacteria[151] and viruses[152], demonstrating its broad-spectrum utility in therapeutic contexts.

In this study, hypericin was pre-dissolved in DMSO to prepare a millimolar stock solution, which was subsequently diluted in RPMI 1640 medium to achieve a final concentration of 0.3 μM. Following incubation with the hypericin solution for 30 minutes, the cells were extensively washed with PBS to remove any unbound PS, ensuring that subsequent photoactivation would target only membrane-bound hypericin. Fluorescence microscopy images were collected after incubation to confirm the accumulation of hypericin on the plasma membrane (Figure 6.13A). Photoactivation was achieved by exposing the cells to blue light (9.2 mW/cm^2) from a LED lamp for 15 minutes, corresponding to a total light fluence of 8.3 J/cm^2. Three hours post-irradiation, oxidative stress was assessed by measuring H_2O_2 levels in the culture medium using a luminescent assay. As shown in Figure 6.14A, ROS levels are significantly elevated in hypericin-treated cells compared to controls exposed to light only. The increased ROS production correlates with a dramatic reduction in cell viability ($<$ 5%) in the treated group 24 hours after PDT, as measured with the MTT assay (Figure 6.14B). This rapid loss of cell viability suggests that the combination of hypericin and blue light effectively induces rapid cell death, most likely through necrosis rather than apoptosis. The swift onset of cytotoxicity and visual inspection of cell morphology through phase-contrast microscopy, acquired before and after PDT, provided further

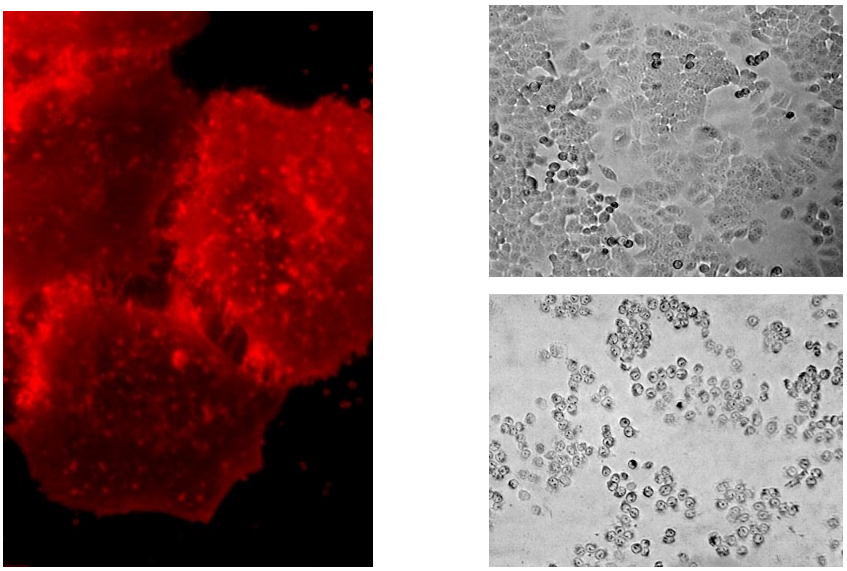

(A) *Fluorescence Imaging of Hypericin Uptake*

(B) *Phase-contrast Imaging of PDT Effects*

Figure 6.13: H322 cells treated with hypericin. A) Uptake of hypericin by fluorescence imaging after 30 minutes of incubation. The PS accumulates mainly on the membrane. B) Effects of PDT on cell morphology 24h post-treatment by contrast phase imaging. Cells were incubated with 0.3 μM hypericin (bottom) or exposed to light only (top).

evidence of necrotic cell death (6.13B). Given that hypericin is predominantly membrane-bound during the 30 minutes-incubation period[139], its cytotoxic effects are likely restricted to the plasma membrane. This is consistent with the observed rapid cell lysis, as damage to the plasma membrane compromises cellular integrity, leading to necrosis.

The high doses of both hypericin and light fluence used in these experiments were deliberately chosen to replicate previously published conditions, thereby ensuring the reliability of our procedure by employing a well-established system with known efficacy[139]. While we recognize that such high doses of both the PS and light are not necessary to achieve a cytotoxic effect (having previously demonstrated the effectiveness of hypericin at 100 nM in the aforementioned study), we aimed to explore these specific conditions for the current investigation.

6.5.2 PDT with EITC-atezolizumab

The applicability of the EITC-atezolizumab immunoconjugate for PDT was finally tested on NSCLC cells. H322 and A549 cells were incubated with increasing doses of EITC-atezolizumab for 2 hours and then exposed to light. Literature indicates that atezolizumab can induce internalization of PD-L1 within 2 hours of incubation[87]. However, only $\sim$ 40% of PD-L1 is internalized at this point, with most of the antibody remaining on the cell membrane, meaning that the PDT effect is still primarily associated with membrane-bound atezolizumab. Preliminary tests used nanomolar concentrations of the complex (from 0.01 μM to 1 μM) consistent with standard PDT protocols for free PSs[139], but they were found non-toxic, even with light doses up to 25.9 J/cm^2 (data not shown). Consequently,

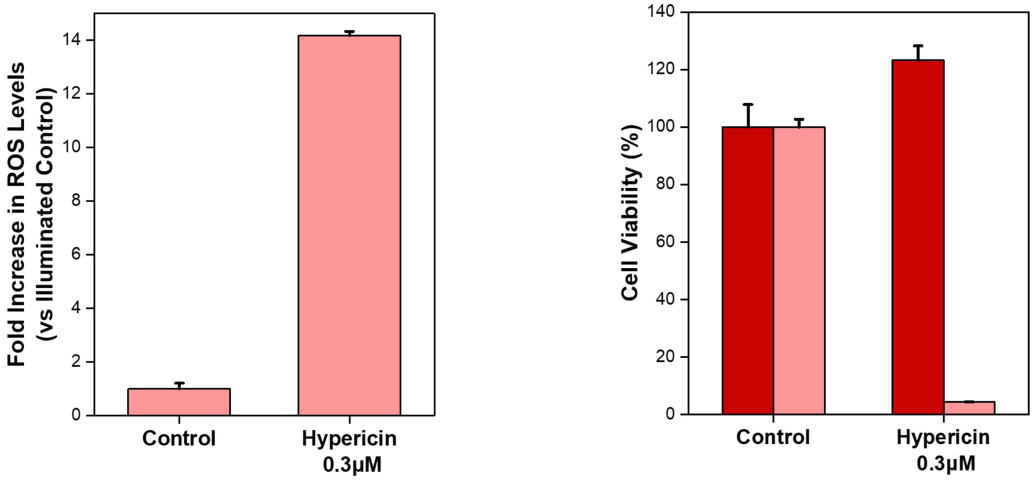

(A) *Oxidative Stress Levels* **(B)** *MTT Assay*

Figure 6.14: Hypericin-mediated PDT. Cells were treated with 0.3 μM of hypericin and illuminated with blue light (fluence: 8.3 J/cm^2). A) ROS-mediated oxidative stress 3 hours after irradiation evaluated with the ROS-Glo H_2O_2 assay. ROS levels in treated cells increase about 14 times compared to control cells exposed to blue light only. Bars are the mean $\pm$ SD of two independent experiments performed in duplicate. B) Cell viability 24 hours after irradiation evaluated with the MTT assay. Treated cells were exposed to light (pink bars) or kept in the dark (red bars) to assess hypericin's citotoxicity. From Alampi et. al[110].

micromolar concentrations of EITC-atezolizumab were tested. Cells were treated with 1 μM, 5 μM, or 10 μM of the complex or with a large excess of atezolizumab (10 μM) for 2 hours and irradiated with blue and green light at 14.4 mW/cm^2 for 1 hour. Early effects of the treatment were observed in both ROS production and cell viability. EITC-atezolizumab increases H_2O_2 levels in a dose-dependent manner in both cell lines, with higher oxidative stress observed in H322 cells compared to A549 cells, where at least 5 μM EITC-atezolizumab is required to trigger significant ROS production (Figure 6.15). Here, "significant ROS production" refers to a statistically significant increase in ROS levels compared to illuminated control cells, used as a baseline. Indeed, each cell line responds differently to oxidative stress, with the critical factor being the balance between ROS generation and removal, rather than the absolute amount of ROS present. Additionally, we observed that RPMI 1640 medium can generate hydrogen peroxide abiotically, which contributes to the overall H_2O_2 levels in the solution. Due to these factors, the average luminescence measured from the plates is not a reliable metric for comparing different cell lines. Instead, the fold increase in ROS generation relative to the corresponding illuminated control with cells offers a more accurate and meaningful parameter. According to this, data are presented as the fold increase in ROS levels over the illuminated cells. Given these results, we can conclude that the EITC-atezolizumab complex triggers ROS production more efficiently in H322 cells compared to A549 cells.

To further investigate cell response to ROS-mediated stress, ATP levels were measured. It is important to note that the ATP assay measures the amount of ATP produced by live cells. A reduction in ATP

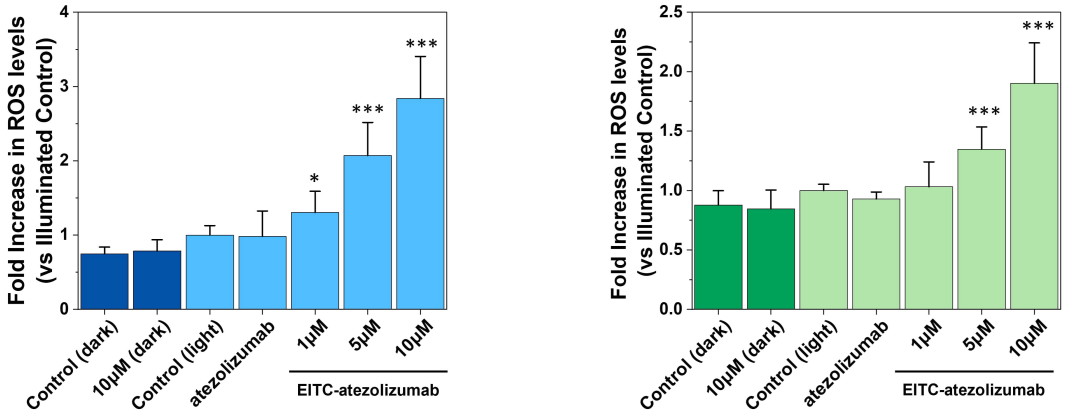

(A) *H322 Cells* **(B)** *A549 Cells*

Figure 6.15: PDT-induced oxidative stress in H322 (blue) and A549 (green) cells when treated with the EITC-atezolizumab complex. ROS levels were measured 3h after irradiation with the ROS-Glo H_2O_2 assay. Data are expressed as the fold increase in ROS levels relative to illuminated control cells, and are the means ± SD of three independent experiments performed in triplicate. *: $p < 0.05$; ***: $p < 0.001$ vs illuminated control. Adapted from Alampi et. al[110].

levels indicates decreased metabolic activity, which may suggest that the cells are either in a quiescent state (from which they can recover) or undergoing cell death. In this study, visual inspection of cell morphology confirmed cell death (see below Figure 6.17), making the ATP a reliable indicator of cell viability. In H322 cells, 1 μM EITC-atezolizumab does not trigger cell death despite increased H_2O_2 levels. Higher concentrations, instead, significantly affect cell viability by generating ROS (Figure6.16A). Three hours after light exposure, viability is reduced by $\sim$ 40% and $\sim$ 75% when 5 μM and 10 μM concentrations of the complex are used, respectively. A549 cells, instead, show even higher sensitivity than H322 cells to the treatment (Figure 6.16B): 5 μM EITC-atezolizumab reduces viability by $\sim$ 65%, despite lower ROS levels. At 10 μM, effects were comparable in the two lines.

The efficacy of EITC-atezolizumab in killing cells was confirmed by the ATP and MTT assays performed 24 hours after the treatment, with consistent results (Figure 6.16C-D). The MTT assay was used to verify that neither light exposure alone nor atezolizumab alone reduces viability, and cells treated with EITC-atezolizumab but kept in the dark remained viable. Thus, the photodynamic action of EITC-atezolizumab is solely responsible for cell death. The ATP results show that cell viability at 24 hours is comparable to that observed at 3 hours. This finding is particularly interesting as it reveals the rapid onset of cell death in both cell lines when treated with high concentrations of the conjugate and exposed to a high light dose. This suggests that an uncontrolled form of cell death, such as necrosis, may be involved rather than a more regulated process like apoptosis. While detailed exploration of the specific death pathways activated by the treatment is beyond the scope of this work, we were able to make some observations based on the qualitative changes in cell morphology post-treatment (Figure 6.17). In both H322 and A549 cells, oxidative stress caused structural alterations leading to either irreversible damage and cell death or a stressed state that alters but does not completely impair

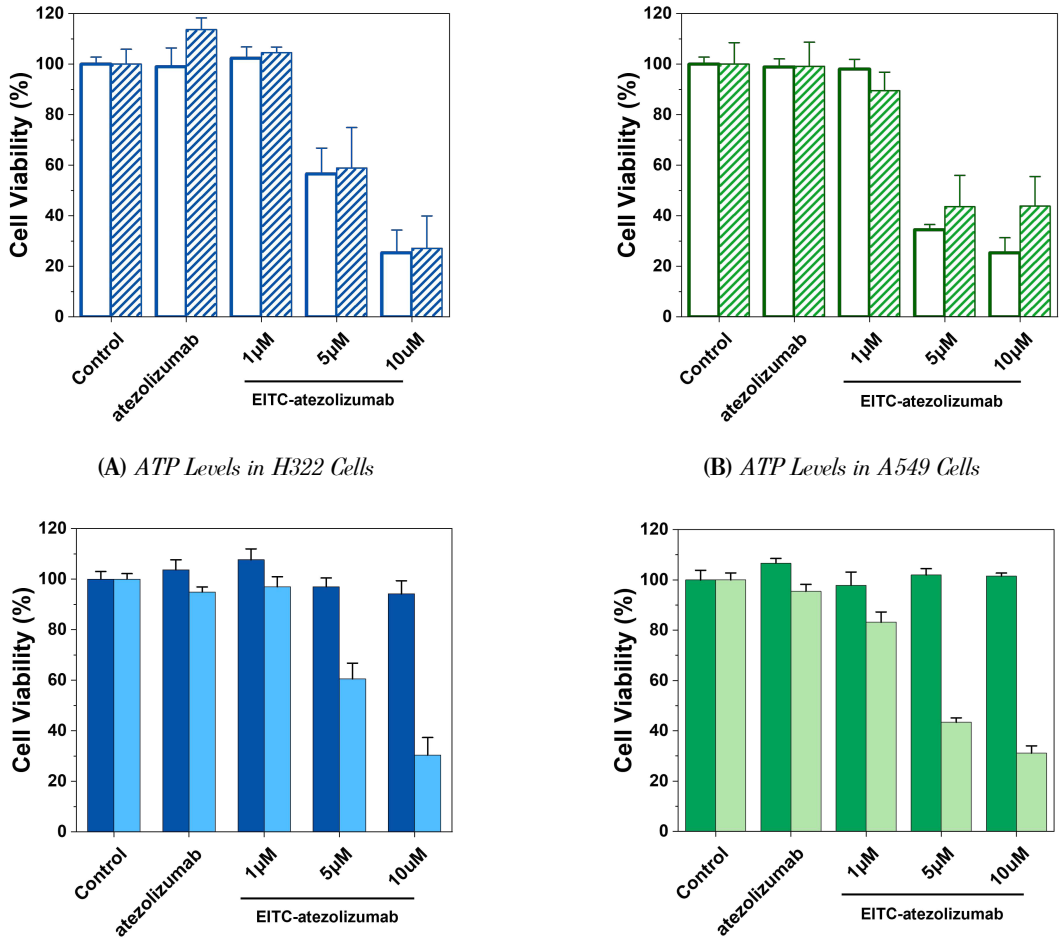

(A) *ATP Levels in H322 Cells*

(B) *ATP Levels in A549 Cells*

(C) *MTT Assay in H1975 Cells*

(D) *MTT Assay in A549 Cells*

Figure 6.16: Effects of PDT with EITC-atezolizumab on cell viability in H322 (blue) and A549 (green) cells. A,B) Cell viability 3 hours (white bars) and 24 hours (dashed bars) after irradiation evaluated with the ATP assay. Data are the means ± SEM of three (H322) or two (A549) independent experiments with four replicates. C,D) Cell viability 24 hours after irradiation evaluated with the MTT assay. Histograms are representative of at least three independent experiments with five replicates carried out in parallel under light and darkness conditions (light blue/light green bars and dark blue/dark green bars, respectively). Cell viability is calculated as a percentage of control and is expressed as the mean ± SD. Adapted from Alampi et. al[110].

cell function. The severity and reversibility of these morphological changes depend on the duration and intensity of the oxidative stress, and on the defense mechanisms against ROS which are cell type-dependent. At the highest concentrations (5 μM and 10 μM), morphological changes in H322 cells indicate cell death, with cells either displaying necrosis-like morphology or rounding up, suggesting detachment from the wells. These changes are evident at 3 hours and still present at 24 hours. At 1 μM, most of the cells survive to PDT treatment, and only a few of them show rounding, indicating potential recovery within 24 hours. Similar observations can be made in A549 cells.

Finally, fluorescence microscopy was used for a quantitative analysis of cell death. One limitation of the ATP and MTT assays is their inability to differentiate between a potential inhibitory effect on cell proliferation and cell death. Therefore, to validate cell viability results, H322 cells were stained with Hoechst 33342 and PI to selectively distinguish between viable and dead cells. The results presented in

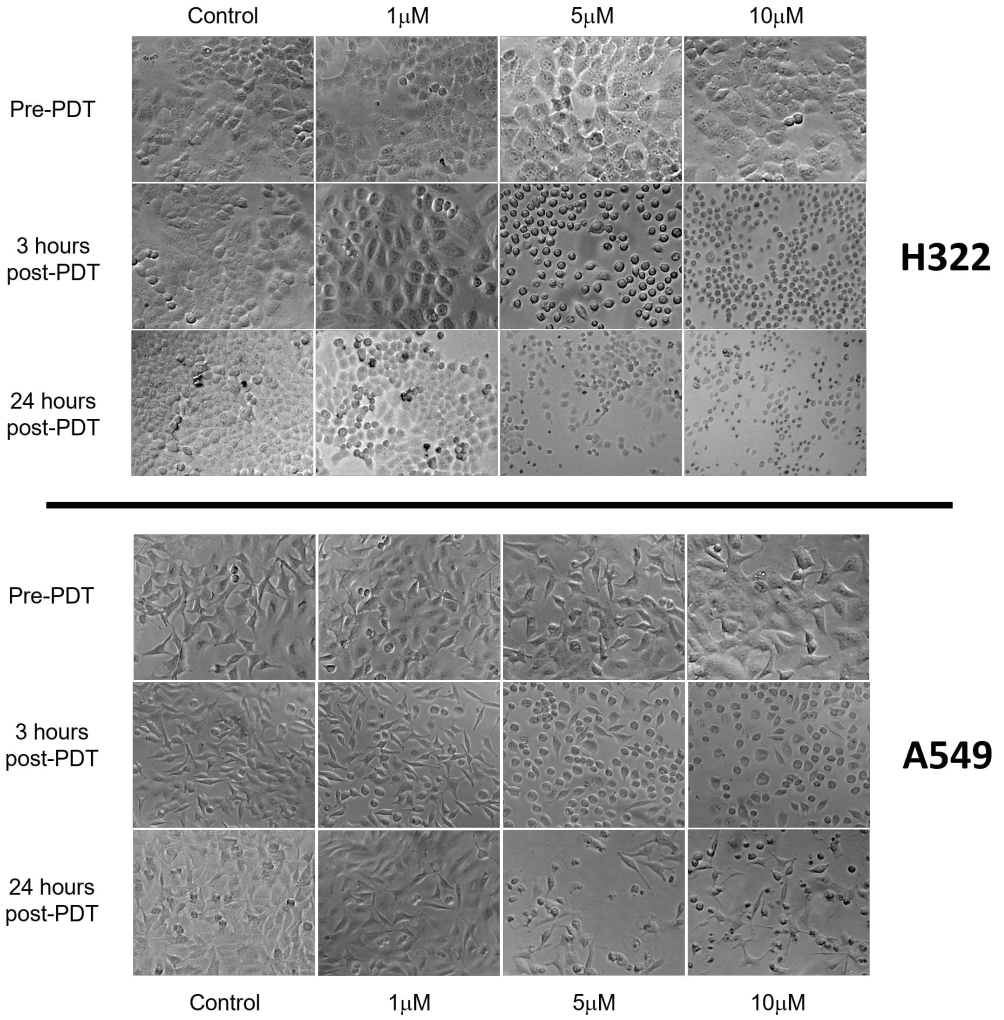

Figure 6.17: Contrast phase images of H322 (top) and A549 (bottom) cells before and after PDT treatment with EITC-atezolizumab. Cells were incubated with 1 μM, 5 μM or 10 μM of the conjugate for 2 hours and then irradiated for 1 hour (fluence: 14.4 mW/cm^2). Pre- and post-PDT indicate cells treated with the immunoconjugate before and after light exposure, respectively. Untreated cells were used as control.

Figure 6.18A are in good agreement with viability assays, with a percentage of cell death of $\sim$ 51% 24 hours after the PDT treatment with EITC-atezolizumab at 10 μM. Again, all control conditions exhibit similar moderate cell death, indicating that neither atezolizumab alone, the light exposure alone, nor the complex kept in the dark have a toxic effect. Additionally, visual inspection of fluorescence images supports the idea of necrotic death, as no nuclei show signs of early apoptosis or significant chromatin condensation (Figure 6.18B). However, the possibility of ferroptosis as an alternative mechanism could not be excluded. Ferroptosis is a regulated form of cell death characterized by iron-dependent lipid peroxidation. Recent research has identified a type of regulated necrosis resembling ferroptosis in cells exposed to ROS-induced lipid peroxidation following PDT with hypericin[153]. Moreover, other studies have been exploring the role of ferroptosis in photodynamic treatments, particularly with third-generation PSs conjugated to monoclonal antibodies[56]. Further investigations are then required to elucidate the main death pathway triggered by the treatment.

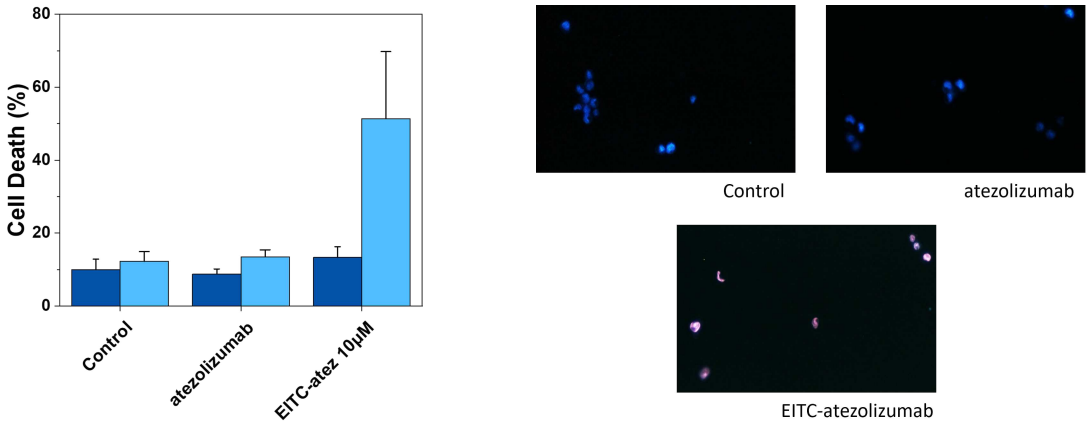

(A) *Cell Death in H322 Cells* **(B)** *Fluorescence Images of H322 Cells*

Figure 6.18: Assessment of cell death by fluorescence microscopy in H322 cells stained with Hoechst 33342/PI 24 hours after PDT treatment. A) Histogram representing the percentages of cell death calculated by determining the ratio of PI-stained cells to total cells per field. Ten fields per condition were counted. Graph represents the mean ± SD of at least three independent experiments carried out under darkness (dark blue) and light (light blue) conditions. B) Representative fluorescence images of cells treated with 10 μM EITC-atezolizumab, 10 μM atezolizumab or only exposed to light (control). Blue and red signals refer to Hoechst 33342 and PI stain, respectively. Adapted from Alampi et. al [110].

6.5.3 Effects of EITC-atezolizumab Internalization on Cell Viability

The diffusion of $^1O_2$ is limited by its short lifetime, meaning that the photodynamic effect is highly dependent on the spatial proximity of the PS to critical cellular targets. As a result, the cellular localization of immunoconjugates is decisive in determining the outcome of PDT treatment. PSs conjugated to internalizing monoclonal antibodies often produce higher photocytotoxic effects than those conjugated to noninternalizing monoclonal antibodies[4], as intracellular localization often places the PS in closer proximity to organelles and other vital structures that are more vulnerable to oxidative damage than the plasma membrane, leading to apoptotic or autophagic cell death pathways. In contrast, noninternalizing monoclonal antibodies tend to remain bound to the cell membrane, where ROS generation may primarily damage the membrane, often resulting in necrosis rather than the more controlled apoptotic pathways. In the context of anti-PD-L1 antibodies, it is well-documented that they can induce PD-L1 internalization upon binding to the receptor[87]. This internalization could potentially enhance PDT effectiveness by concentrating the PS inside the cell, particularly in organelles such as lysosomes or mitochondria, where ROS generation may have more pronounced cytotoxic effects. Therefore, the EITC–atezolizumab conjugate was allowed to be internalized to investigate whether this leads to an improved therapeutic effect compared to membrane-bound interactions alone.

This set of experiments was performed at the Institute for Cancer Research at the Oslo University Hospital. To ensure consistency with previous PDT experiments, H1975 and A549 cell lines were selected as high and low PD-L1 expressers, respectively, based on preliminary flow cytometry results. Flow cytometry was performed on live cells to evaluate the binding of AF647-atezolizumab to PD-L1

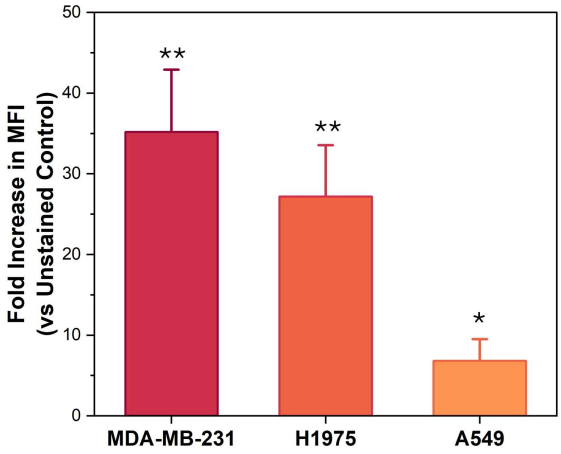

Figure 6.19: PD-L1 surface expression levels measured by flow cytometry. PD-L1 receptors were stained with atezolizumab directly conjugated to AF647 dye. Unstained cells were used as control. For each cell line, the relative PD-L1 expression levels are the fold increase in MFI relative to unstained cells. Data represent the mean ± SD of three independent experiments. **: $p < 0.01$; *: $p < 0.05$ vs unstained cells.

and to assess PD-L1 expression levels across cell lines, with MDA-MB-231 cells serving as a positive control for PD-L1 expression[101]. Cells were harvested at approximately 80% confluence, washed with PBS, and incubated with 1 μM AF647-atezolizumab in a 0.5% BSA solution for 20 minutes on ice to prevent receptor internalization. Following incubation, cells were washed twice with 0.5% BSA to remove unbound antibodies and resuspended in PBS at a density of 1×10^6 cells/mL for analysis. Flow cytometric measurements were conducted using an LSRII flow cytometer (Becton Dickinson, Franklin Lakes, NJ, USA) equipped with a 640 nm laser for AF647 excitation. At least 10,000 events were recorded per sample. Acquired data were analyzed using FlowJo software version 10.7.1 (Treestar, OR, USA). PD-L1 expression levels are reported as the MFI of AF647-atezolizumab binding, normalized to unstained control samples (Figure 6.19). All experiments were conducted in triplicate to ensure reproducibility.

PDT treatment was performed following overnight incubation of the EITC-atezolizumab complex at varying concentrations (0.5 μM, 1 μM, 5 μM, or 10 μM), as described in Section 5.9. Cell viability was assessed using the MTS assay the day after the treatment.

The extended incubation period favors the effective uptake of the complex, resulting in a positive treatment effect. H1975 cells show the most notable response, with less than 25% cell viability observed at 5 μM and 10 μM concentrations. Remarkably, even at a submicromolar concentration of 0.5 μM, a significant reduction in viability (by approximately 40%) is observed. A similar effect is seen in A549 cells, though to a lesser extent, confirming that the treatment remains effective even at lower PD-L1 expression levels. However, A549 cells do not show increased mortality with the extended incubation compared to the previous results from a 2 hours incubation (Figure 6.20). Nevertheless, the effects observed with the two incubation times (2 hours vs. 20 hours) are consistent within the error bars, and

the discrepancies can be attributed to factors such as intrinsic cell variability or differences between the MTT and MTS assays used to evaluate viability.

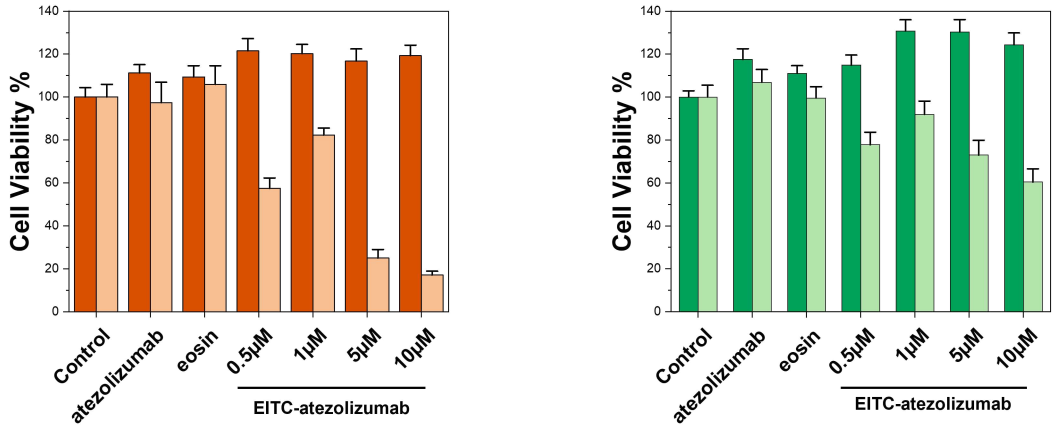

(A) *H1975 Cells* **(B)** *A549 Cells*

Figure 6.20: Cell viability for H1975 (orange) and A549 (green) cells measured with the MTS assay at 24 hours. Cells were incubated overnight with increasing concentrations of EITC-atezolizumab and then irradiated for 1 hour with blue and green light (fluence: 65.2 J/cm^2). Cell viability relative to control cells is expressed as mean ± SEM. Histograms are representative of three (H1975) or two (A549) independent experiments with five replicates performed in parallel under light and darkness conditions (light orange/light green bars and dark orange/dark green bars, respectively).

6.5.4 Final Considerations

Our study showed that the EITC–atezolizumab immunoconjugate effectively induces cell death in NSCLC cells expressing PD-L1 at different levels. While nanomolar or picomolar concentrations are usually sufficient for free PSs, micromolar concentrations were necessary in this case to achieve significant PDT effects, as lower concentrations proved ineffective. These higher doses are often required in more resistant or less targeted cell populations, when the PS needs to generate more ROS for effective killing cells. Notably, high concentrations of atezolizumab have also been used in previous studies[68,101]. However, it is unclear why lower concentrations are ineffective, especially considering that the antibody's dissociation constant is in the nanomolar range (0.62 nM for the monomeric form and 0.19 nM for the dimeric form of PD-L1)[87]). While the reduced quantum yield of $^1O_2$ generation of the complex (approximately one-fifth that of free EITC) partially explains the need for higher doses, it is likely that the interaction with the receptor further diminishes the Φ_Δ, impairing the efficiency of ROS generation. Nevertheless, when high concentrations and light doses are used, EITC–atezolizumab exhibited significant phototoxic activity even in A549 cells, which have low PD-L1 levels. This indicates that intrinsic cell characteristics, such as their ability to respond to ROS-induced stress, may be crucial in determining the response to PDT, and that the efficacy of the treatment may not necessarily correlate with PD-L1 expression levels. Consequently, this complex could be therapeutically effective even in tumor with low amounts of PD-L1[7]. Similar findings have been reported with other targets,

where treatment effectiveness does not directly correlate with receptor expression. For example, HER2 expression levels do not consistently predict treatment outcomes in cholangiocarcinoma and breast cancer[154,155], and different PDT responses have been observed in two B-cell lymphoma cell lines expressing similar levels of CD20[156]. Furthermore, although EGFR expression has been associated with increased PIT efficacy in glioblastoma[157,158], results are inconsistent across other cancers[159,160]. To conclude, the EITC–atezolizumab complex demonstrated effective cell death induction in H1975, H322, and A549 cells, regardless of PD-L1 expression levels. This suggests its potential as a promising PDT approach, even for tumors with low amount of PD-L1. However, understanding the specific mechanisms of cell death and the role of cellular characteristics is crucial for optimizing treatment strategies. While this study offers valuable insights, it is limited to *in vitro* conditions, and further validations through *in vivo* studies are needed[5].

6.6 Photochemical Internalization of Gelonin in NSCLC Cells

Following the assessment of the EITC–atezolizumab complex's effectiveness in inducing cell death through PDT, we explored the potential of PCI in enhancing the cytotoxicity of the immunoconjugate. While PDT primarily functions by generating ROS to induce cell death directly at the target site, PCI employs light to facilitate the release in the cytosol of therapeutic agents, such as toxins or immunotoxins, that are otherwise sequestered within endosomes and susceptible to degradation after cellular uptake.

PCI experiments were carried out at the Norwegian Radium Hospital on H1975 and A549 cells. In these experiments, the EITC-atezolizumab complex was combined with the recombinant toxin gelonin, a type I RIP with confirmed cytotoxic effects on cancer cells[99]. The goal was to determine the impact of this combined treatment on cell viability, assessing whether the PCI technology could enhance the therapeutic efficacy of the conjugate by promoting the intracellular release of gelonin, thereby potentiating the cell-killing effects of the EITC-mediated PDT. Additionally, we investigated whether the binding of atezolizumab to PD-L1 receptors on the surface of cancer cells might influence the cellular response to PDT. By binding to PD-L1, atezolizumab may alter the tumor environment and potentially affect the way cells respond to the combined PDT and PCI treatment.

6.6.1 PCI of Gelonin

Gelonin is a potent ribosome-inactivating protein (RIP) derived from the seeds of the *Gelonium multiflorum plant*. It functions by irreversibly inactivating ribosomes, thereby halting protein synthesis and leading to cell death. Due to its strong cytotoxic properties, gelonin has attracted significant interest in cancer research, particularly as a component of targeted therapies. While gelonin itself exhibits low toxicity in intact cells, its effects are greatly enhanced when used in combination with

antibodies in PCI protocols[99,100,103]. PCI can be used to photo-induce the re-localization of gelonin from endosomal and lysosomal compartments to the cytosol and the nucleus[99].This allows gelonin to reach the cytoplasm in its active form and effectively damage ribosomal RNA.

Preliminary PCI experiments were performed in collaboration with Magdaléna Kozlíková from Charles University (Prague, Czech Republic) to assess the effects of PCI of gelonin on cell viability. To trigger the release of gelonin from the endosomes into the cytosol, we used the amphiphilic PS $TPCS_{2a}$ (fimaporfin)[95]. Fimaporfin is a porphyrin-based PS with two sulfonate groups on adjacent phenyl rings, which mainly absorbs blue (λ_{max} = 420 nm) and red (λ_{max} = 652 nm) light. The PS was allowed to internalize overnight, before replacing the medium with fresh complete medium containing gelonin. Following a 4-hour incubation, the cells were extensively washed with fresh medium before being exposed to blue light for up to 3 minutes. The light-dose dependent cytotoxic response of cells to PCI ($TPCS_{2a}$ + gelonin + light) compared to PDT ($TPCS_{2a}$ + light) is shown in Figure 6.21.

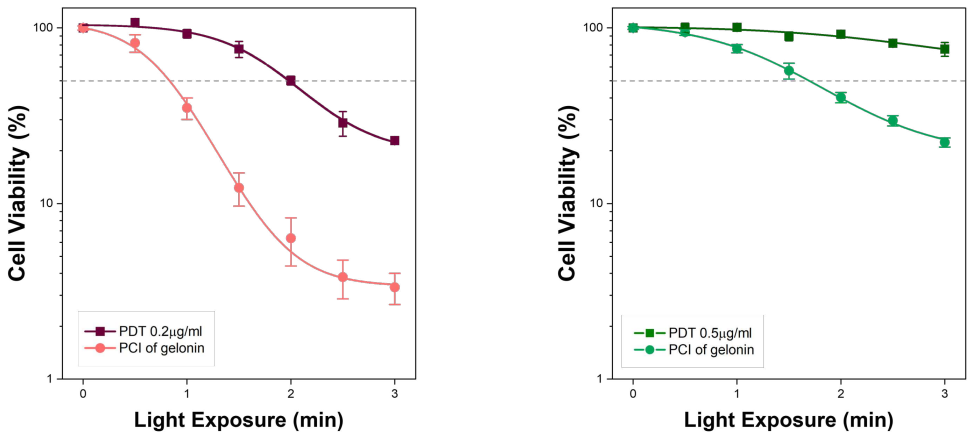

(A) *H1975 Cells* **(B)** *A549 Cells*

Figure 6.21: Light-induced cytotoxicity in H1975 (A) and A549 (B) after PCI of gelonin compared to PDT ($TPCS_{2a}$ + light). Relative cell viabilities are measured 48 hours post-light exposure with the MTS assay, and presented as a percentage of control cells. Data are the mean ± SEM of three independent experiments performed in triplicates.

In both H1975 and A549 cell lines, enhanced cytotoxicity is observed after PCI, with the effect correlating to the light fluence, as measured by the MTS assay. Two days post-illumination, H1975 cell viability decreased by ~50% after just 50 seconds of exposure to light and dropped to less than 10% after 90 seconds in cells treated with gelonin. A549 cells also exhibit sensitivity to PDT, with viability reduced to approximately ~50% in 118 seconds, and a survival of ~ 23% after 3 minutes of light exposure. Interestingly, A549 cells display greater resistance to both PCI and PDT treatments. While PDT alone results in minimal cytotoxicity (< 20%), combining PDT with gelonin reduces cell viability by ~50% after 100 seconds, and by ~80% after 180 seconds of irradiation. These experiments well-shown the synergistic cytotoxic effect between the PS $TPCS_{2a}$ and the toxin gelonin, and were included in this

work as a positive control for the PCI protocol.

6.6.2 PCI of Gelonin in Combination with Unconjugated Atezolizumab

In our PDT experiments, we demonstrated that atezolizumab alone is non-toxic, even at micromolar concentrations (see section 6.5). To evaluate whether atezolizumab could enhance the efficacy of PCI when internalized, H1975 and A549 cells were co-incubated with the PS $TPCS_{2a}$ and atezolizumab at three different concentrations (1 μM, 5 μM, or 10 μM) for 20 hours. Following incubation, the cells were washed, treated with gelonin, and then illuminated according to a standard PCI protocol. Cell viability was assessed two days later, comparing the outcomes of PDT with atezolizumab to those achieved through PCI. The results for both cell lines lead to similar conclusions. As shown in Figure 6.22, no synergistic cytotoxic effect is observed by combining PD-L1 blockade with PCI under the tested conditions. After 3 minutes of illumination, PDT ($TPCS_{2a}$ + 10 μM atezolizumab + light) induces a $\sim$ 59% and a $\sim$ 48% reduction in cell viability in H1975 and A549 cells, respectively. Viability further drops to $\sim$ 25% in H1975 and to $\sim$ 30% in A549 cells with PCI, independent of atezolizumab concentration. We deduced that the greater cytotoxicity of PCI, as compared to PDT with fimaporfin, is primarily due to the toxic action of gelonin released in the cytosol upon illumination. Increasing atezolizumab concentration does not significantly alter the response to PCI treatment, except for a modest effect observed at the highest light dose with 10 μM atezolizumab. However, given the substantial variability, particularly in A549 cells, this slight increase in efficacy does not constitute a significant advantage in favor of PCI over PDT. Thus, we concluded that blocking PD-L1 receptors with atezolizumab does not meaningfully enhance PCI cytotoxicity compared to PDT alone.
Additionally, when considering the results obtained for PCI of gelonin from the previous section (Figure 6.21), we hypothesized that the interaction of atezolizumab with PD-L1 might trigger a cellular response that actually reduces, rather than enhances, the efficacy of PDT (and consequently of PCI). In the presence of the antibody, cell viability in H1975 cells is 3-fold higher after 1 minute of light exposure and 8-fold higher after 2 minutes, compared to the protocol without atezolizumab. Although the discrepancy between the two protocols (with and without the antibody) is less pronounced in A549 cells, PCI is still 1.4-fold less effective after 2 minutes of illumination when the antibody is present. This effect of PD-L1 blockade on PCI efficacy has not been described in the current literature, and it is possible that PD-L1 antibody blocking may reduce the rate of endocytosis, leading to lower uptake of the toxin and a consequent reduction in cytotoxic effect. However, additional studies will be required to confirm this effect and potentially investigate the underlying mechanisms.

6.6.3 PCI of Gelonin in Combination with EITC-atezolizumab

Another set of experiments was planned to evaluate the response of H1975 and A549 cells to PCI of gelonin combined to treatment with EITC-atezolizumab. Cells were either incubated for 20 hours with

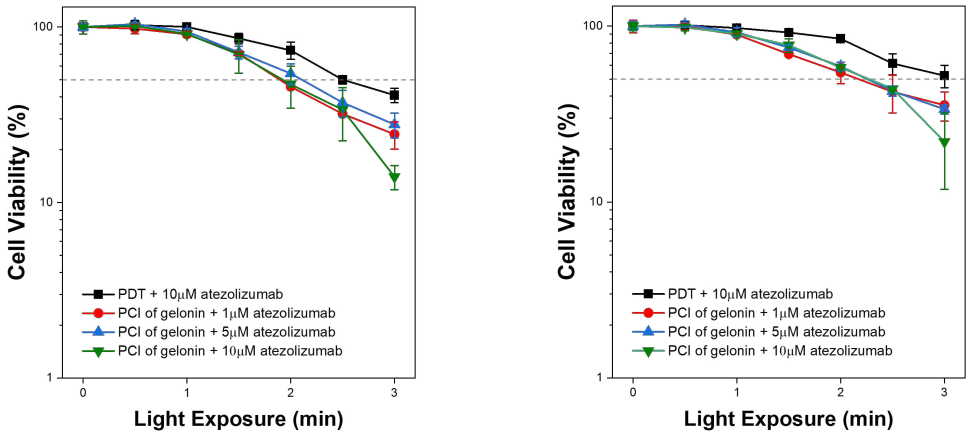

(A) *H1975 Cells* **(B)** *A549 Cells*

Figure 6.22: Blocking of PD-L1 with atezolizumab does not enhanced gelonin's cytotoxicity. Light-dependent PCI of gelonin in H1975 (A) and A549 (B) using increasing concentrations of atezolizumab in combination with $TPCS_{2a}$. Cells were co-incubated with fimaporfin and atezolizumab for 20 hours, subsequently washed and incubated with gelonin for 4 hours prior to light exposure. $TPCS_{2a}$ was diluted in culture medium to a final concentration of 0.2 μg/ml (H1975) or 0.5 μg/ml (A549). Cytotoxicity was evaluated with the MTS assay 48 hours post-irradiantion, and presented as a percentage of control cells. Data are the mean $\pm$ SEM of at least two independent experiments performed in triplicates.

EITC-atezolizumab for PDT only, or co-incubated with gelonin (100 nM) for the PCI experiments, then washed and illuminated with blue and green light. The impact of the PCI treatment was evaluated both increasing the light-exposure time while maintaining a constant EITC-atezolizumab concentration (1 μM), and increasing EITC-atezolizumab concentration up to 5 μM while keeping the light dose fixed (60 minutes of light exposure correspond to $\approx$ 65.2 J/cm^2).

Unfortunately, in H1975 cells increasing either the light dose or the concentration of the complex failed to significantly enhance cytotoxicity. Specifically, using 1 μM EITC-atezolizumab, cell viability is reduced by $\sim$ 20% regardless of the light dose and the presence of gelonin (Figure 6.23A). This finding is in line with previous results from PDT experiments, suggesting that the observed cytotoxic effect is largely due to the PS's inherent toxicity rather than the PCI-mediated delivery of gelonin. Higher EITC-atezolizumab concentrations result in a comparable reduction in viability, within the error bars, with both PDT and PCI leading to $\sim$ 40% cell death, when the light dose is fixed at 60 minutes of illumination (Figure 6.23B).

The effect on the A549 cell line is similar to that observed in H1975 cells. Combining EITC-atezolizumab with gelonin does not result in any increased cytotoxicity when compared to PDT alone (Figure 6.23B). The consistent lack of enhanced cell death across both cell lines suggests a common limitation in the experimental setup or mechanism. One explanation could be that the cellular response to PDT is already maximal, such that additional cytotoxicity from gelonin (even if internalized via PCI) would have minimal impact. Another possibility is that the two selected cell lines may be less responsive to

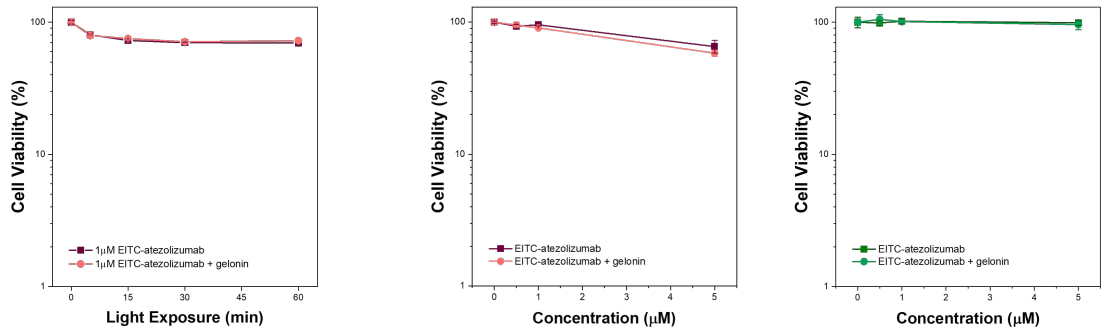

(A) *Fixed Drug Dose* **(B)** *Fixed Light Dose*

Figure 6.23: EITC-atezolizumab cytotoxicity is not enhanced by PCI of gelonin. A) Light-dependent PCI of gelonin in H1975 cells compared to PDT (1 μM EITC-atezolizumab + light). B) Concentration-dependent PCI of gelonin in H1975 (left) and A549 (right) using a fixed light dose (60min $\approx$ 65.2 J/cm^2). Cells were co-incubated with EITC-atezolizumab and gelonin overnight before light exposure. For all experiments, cell viability was evaluated 48 hours post-irradiation using the MTS assay. Representative experiments out of at least two independent experiments performed in triplicates. Data are the mean $\pm$ SEM.

PCI-mediated gelonin delivery under the tested conditions, possibly due to differences in endosomal escape efficiency or the internalization dynamics of the EITC-atezolizumab complex.

6.6.4 Final Considerations

The cytotoxicity of unconjugated atezolizumab, administered to cells either as monotherapy or in combination with PDT, was evaluated in a recent study[101]. The authors demonstrated that the drug is not effective in enhancing the PDT efficacy of the PS fimaporfin at concentrations up to 10 μM and light doses of 1.1 J/cm^2. They concluded that PD-L1 blockade does not affect cell viability. However, in this work, the PS and the antibody were administered to the cells separately and internalized via two distinct mechanisms (i.e., fluid-phase endocytosis and receptor-mediated endocytosis, respectively). This could result in their accumulation in different endocytic vesicles, leading to ineffective PCI treatment. To overcome this potential limitation, we tested the EITC-atezolizumab complex, which has demonstrated significant efficacy as a protein-based PDT agent (see Section 6.5), in combination with PCI of gelonin. In this approach, the PS is covalently linked to atezolizumab, ensuring its internalization alongside the antibody through receptor-mediated endocytosis. Preliminary experiments were conducted to assess the cytotoxic response of the selected NSCLC cell lines to PCI of gelonin alone or in combination with unconjugated atezolizumab. While some variability in the results was observed, particularly in A549 cells, the data suggest that PD-L1 blockade does not synergize with PCI to increase therapeutic efficacy under the tested conditions. Interestingly, our results also imply that PD-L1 inhibition might reduce PCI effectiveness, potentially by reducing the endocytosis rate. Further experiments using alternative cell lines or treatment conditions will be necessary to better elucidate the interaction between immune checkpoint blockade and PCI. Additionally, the absence of enhanced efficacy when combining PCI

with EITC-atezolizumab highlights the need for further investigations into the mechanisms of PD-L1 internalization and trafficking, which may limit PCI's therapeutic potential in these contexts.

6.7 PD-L1 Endocytosis and Intracellular Trafficking in NSCLC Cells

The endosomal trafficking of PD-L1 remains an under-researched area, yet it plays a crucial role in regulating PD-L1 availability on the cell surface. After being synthesized in the endoplasmic reticulum and processed in the Golgi apparatus, PD-L1 is transported to the plasma membrane, where it mediates immune suppression. Once at the membrane, PD-L1 can be internalized via endocytosis and sorted in early endosomes, which direct PD-L1 either back to the plasma membrane for recycling or towards late endosomes and lysosomes for degradation[161]. Recycling is facilitated by proteins like CMTM6, which prevent PD-L1 from being degraded and allow it to return to the membrane[162]. Alternatively, PD-L1 can be marked for degradation via ubiquitination, leading to its transport to multivesicular bodies (MVBs) and ultimately lysosomes, where it is broken down. Post-translational modifications like palmitoylation and interactions with regulatory proteins control the balance between recycling and degradation, determining the levels of PD-L1 available on the cell surface to inhibit immune responses[161,163]. In this context, tracking the colocalization of PD-L1 with intracellular organelles provides crucial insights into whether PD-L1 is predominantly routed towards recycling pathways or targeted for degradation. Understanding these dynamics is particularly important for interpreting our PDT/PCI results, as differences in PD-L1 trafficking between the H1975 and A549 cell lines may lead to varying treatment efficacy or even suggest potential mechanisms of resistance.

To investigate the intracellular dynamics of PD-L1, live H1975 and A549 cells were stained with AF647-atezolizumab for varying time points (10 minutes, 30 minutes, 1 hour, 2 hours, 6 hours, and 24 hours) before fixation. Importantly, anti-PD-L1 therapeutic antibodies do not seem to alter PD-L1 trafficking[161], making atezolizumab an ideal choice for selectively staining PD-L1 while allowing the study of its natural endocytic and trafficking pathways after binding a protein. Detecting PD-L1 within organelles associated with the lysosomal degradation pathway can indicate that atezolizumab not only blocks PD-L1 on the plasma membrane but also facilitates its removal from the cell. By promoting the degradation of PD-L1, atezolizumab may help prevent the recycling of PD-L1 back to the membrane surface, where elevated levels can contribute to immune evasion and diminish the effectiveness of immune responses against tumors[9].

6.7.1 Lysosomal Involvement in PD-L1 Trafficking

As briefly mentioned, a key aspect of this study involves tracking the intracellular distribution of PD-L1 indirectly through its binding to fluorescently tagged atezolizumab. The colocalization between the atezolizumab and lysosomal signals was assessed using quantitative metrics, specifically Pearson's

correlation coefficient and Mander's overlap coefficient. The Pearson's coefficient measures the linear correlation between the two signals across the entire cell population, while Mander's coefficient quantifies the degree of overlap between the two signals in specific regions of interest. Using both metrics provides a refined (even though not comprehensive) understanding of PD-L1 trafficking dynamics and allows to evaluate the extent of its localization within lysosomal compartments. These coefficients were calculated for four out of the six conditions tested, specifically for cells incubated with AF647-atezolizumab for 10 minutes, 2 hours, 6 hours, and 24 hours, along with CellMask for membrane staining and LysoTracker blue to mark lysosomes.

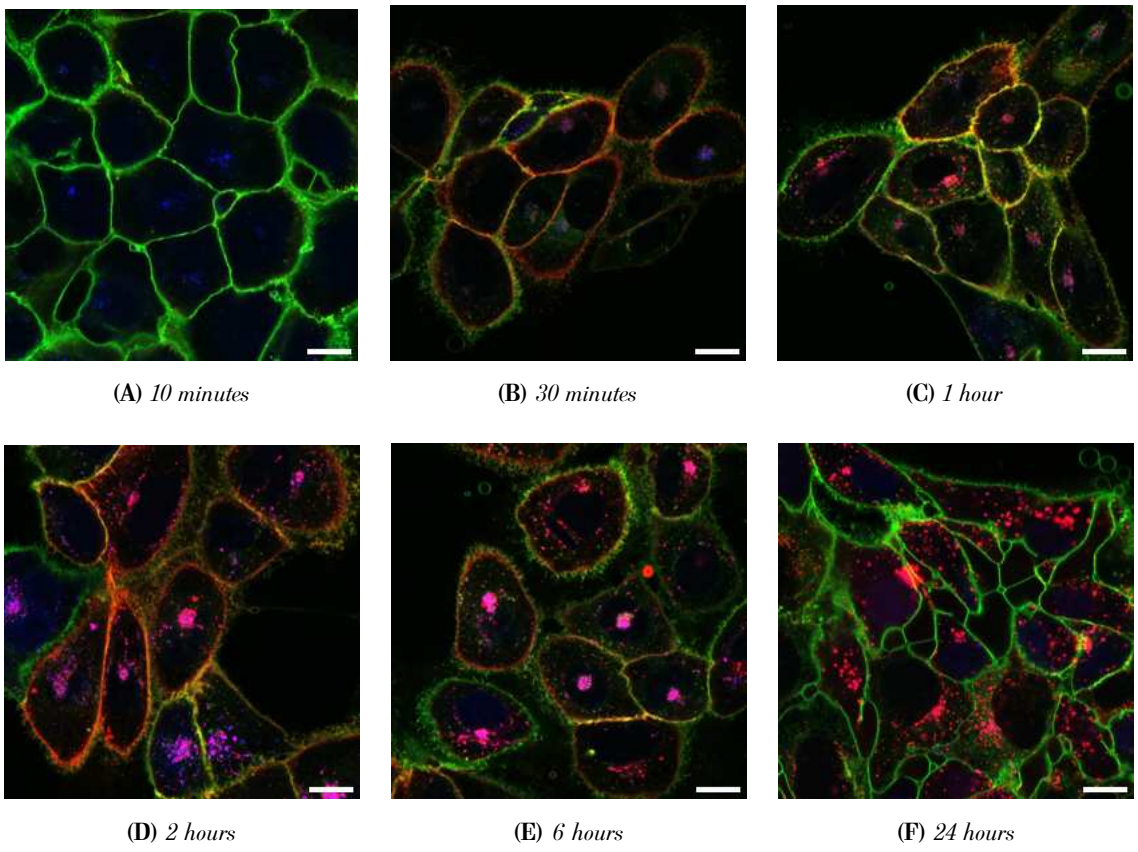

(A) *10 minutes* **(B)** *30 minutes* **(C)** *1 hour*

(D) *2 hours* **(E)** *6 hours* **(F)** *24 hours*

Figure 6.24: Confocal images of H1975 cells showing PD-L1 trafficking at various time points after incubation with AF647-atezolizumab (red) for 10 minutes (A), 30 minutes (B), 1 hour (C), 2 hours (D), 6 hours (E), and 24 hours (F). Cells were co-stained with Cell Mask (green) for membrane visualization and LysoTracker (blue) to mark lysosomes. Early time points (A–C) show PD-L1 primarily localized to the cell membrane (yellow signal indicates colocalization between AF647-atezolizumab and the CellMask), with increasing internalization into the cytoplasm by 2–6 hours (D–E). At 6 hours, likely formation of MVBs and notable colocalization with lysosomes is observed (pink clusters), while by 24 hours (F), PD-L1 appears predominantly intracellular, with reduced lysosomal colocalization, suggesting potential recycling. Scale bar: 10 μm.

Representative confocal images of the H1975 and A549 cell lines are presented in Figure 6.24 and Figure 6.25, respectively. At the early time points, PD-L1 predominantly localizes to the cell membrane, where it is readily accessible for antibody binding in both cell lines (images A and B). Starting at around 1 hour of incubation, distinct localization patterns of PD-L1 emerge. In H1975 cells, PD-L1 progressively moves away from the plasma membrane to the cytosol, where it accumulates in

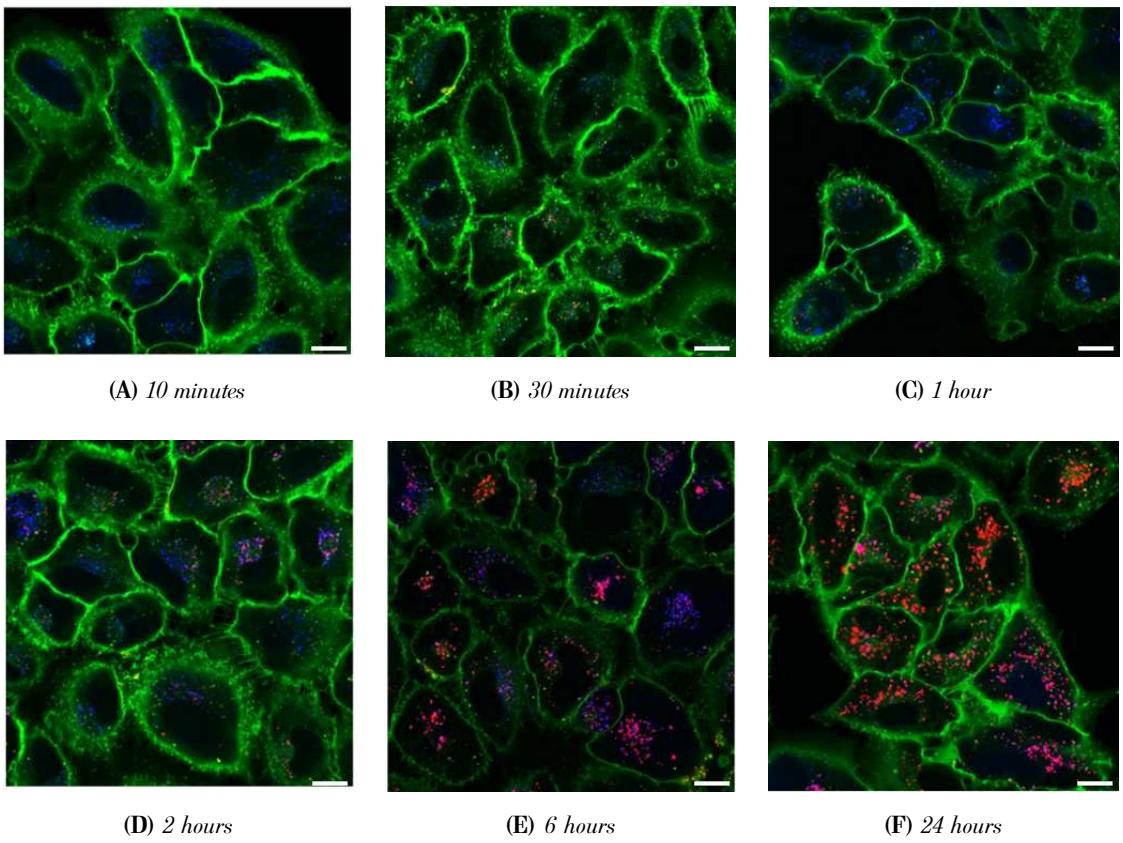

(A) *10 minutes* **(B)** *30 minutes* **(C)** *1 hour*

(D) *2 hours* **(E)** *6 hours* **(F)** *24 hours*

Figure 6.25: Confocal images of A549 cells showing PD-L1 trafficking at various time points after incubation with AF647-atezolizumab (red) for 10 minutes (A), 30 minutes (B), 1 hour (C), 2 hours (D), 6 hours (E), and 24 hours (F). Cells were co-stained with Cell Mask (green) for membrane visualization and LysoTracker (blue) to mark lysosomes. Over time, PD-L1 internalization and its colocalization with lysosomes steadily increase, without the formation of clusters, indicating a clear pathway towards lysosomal degradation and without apparent recycling of PD-L1. Scale bar: 10 μm.

LysoTracker-positive intracellular compartments forming clusters (pink clusters in Figures 6.24 C-E). These clustered structures, primarly found in the perinuclear region, suggest the formation of MVBs, typically indicative of the fusion of early endosomes with late endosomes or lysosomes. This is consistent with the expectation that PD-L1 is routed towards lysosomal degradation after binding atezolizumab, subsequently reducing its availability on the cell surface. Quantitative analysis confirms a strong, increasing colocalization between PD-L1 and lysosomes over time, reaching a maximum at 6 hours (Figure 6.26A). However, by 24 hours, both the imaging data (Figure 6.24F) and quantitative metrics show a decrease in colocalization and the disappearance of the clusters, suggesting that PD-L1 may be recycled back to the plasma membrane. If confirmed, this could represent a cell-specific mechanism in which PD-L1 is not only targeted for degradation but also recycled, depending on cellular context or environmental cues. This finding is consistent with existing literature indicating that PD-L1 trafficking is modulated by cellular signaling pathways and interactions with other receptors[9,164].

In contrast, A549 cells exhibit distinctly different trafficking dynamics. No aggregate formation was observed in this cell line, but PD-L1 is found in punctate structures that likely correspond to lysosomal vesicles (pink dots in Figure 6.25 C-F). Accordingly, the degree of colocalization between PD-L1 and

lysosomes steadily increases from 10 minutes to 24 hours (Figure 6.26A), suggesting a more definitive lysosomal degradation pathway for PD-L1 in this cell line.

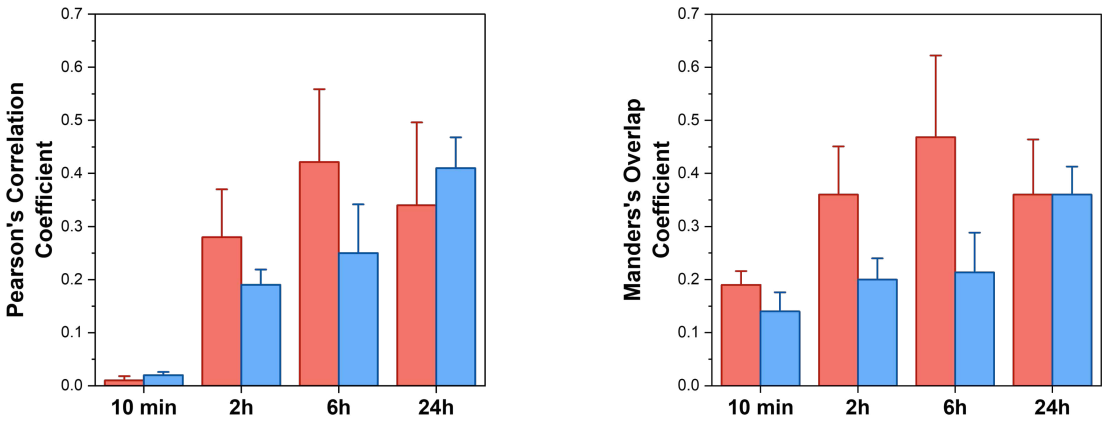

(A) *Pearson's Coefficient* **(B)** *Mander's Coefficient*

Figure 6.26: Quantification of PD-L1 colocalization with lysosomes in H1975 (red) and A549 (blue) cells using Pearson's correlation coefficient (A) and Mander's overlap coefficient (B) at different time points (10 min, 2h, 6h, and 24h) after incubation with AF647-atezolizumab. Pearson's coefficient reflects the overall correlation between PD-L1 and lysosomal markers, while Mander's coefficient measures the extent of PD-L1 overlap with lysosomes. In H1975 cells, colocalization increases up to 6 hours and decreases at 24 hours, suggesting potential PD-L1 recycling. In contrast, A549 cells show a continuous increase in colocalization, indicating steady lysosomal degradation. The results are mean ± SD of three individual experiments.

The differences between the two cell lines suggest that PD-L1 trafficking and recycling may be influenced by intrinsic cellular characteristics, potentially leading to variability in therapeutic outcomes when treated with atezolizumab. Furthermore, the steady increase in Mander's coefficient in A549 cells contrasts with the trend observed in H1975 cells, where the coefficient initially rises to a maximum and then decreases (Figure 6.26B). This difference highlights the distinct cellular mechanisms at play and reinforces the notion that PD-L1 trafficking can vary significantly across NSCLC subtypes, with potential implications for the efficacy of PD-L1-targeted therapies.

6.7.2 CD63-Mediated Vesicular Sorting of PD-L1

The previous findings highlight the importance of further investigating the mechanisms that regulate PD-L1 recycling and degradation across different cell lines. Since intracellular trafficking is a complex process involving various pathways and compartments, understanding the ones responsible for PD-L1 sorting and degradation is crucial. To clarify the nature of these compartments, NSCLC cells were double-stained with AF647-atezolizumab and CD63, a well-established marker for late endosomes, MVBs, and lysosomes. The CD63 receptor plays a key role in vesicle trafficking and fusion events and is integral to the formation and maturation of MVBs, which can either fuse with lysosomes for degradation or be rerouted to the plasma membrane for exosome release[161]. Assessing CD63 colocalization with

PD-L1, we aimed to confirm our previous results obtained with LysoTracker (see previous Section 6.7.1) and determine whether PD-L1 is primarily trafficked towards lysosomal degradation or if it may also follow an endocytic recycling pathway.

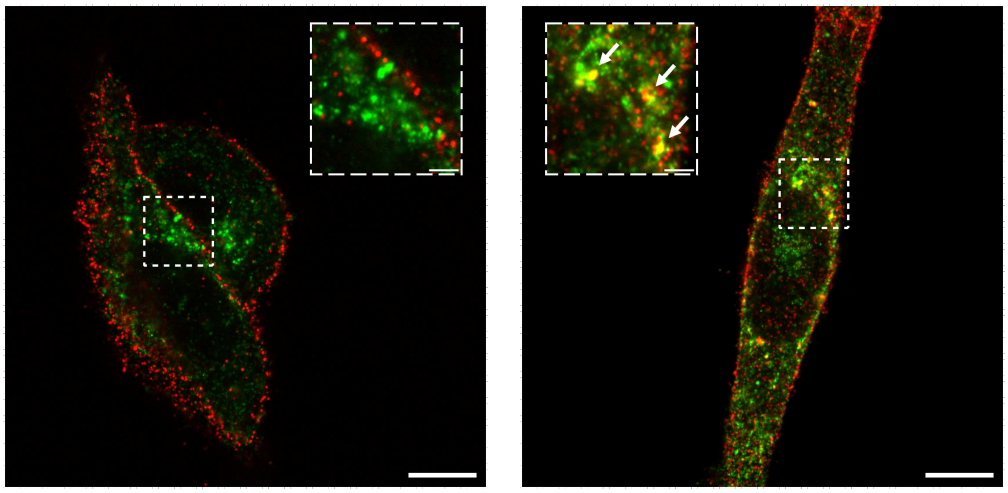

(A) *10 minutes*

(B) *2 hours*

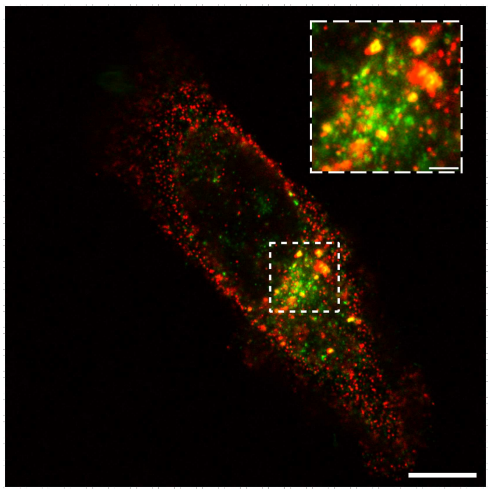

(C) *6 hours*

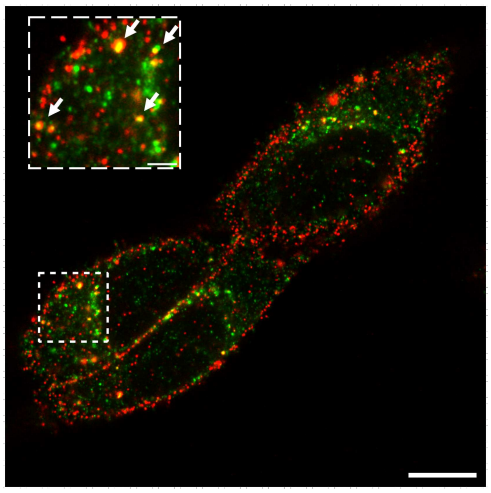

(D) *24 hours*

Figure 6.27: Confocal images of H1975 cells showing PD-L1 colocalization with CD63-positive organelles. Cells were incubated with AF647-atezolizumab (red) for 10 minutes (A), 2 hours (B), 6 hours (C), and 24 hours (D), fixed, permeabilized, and co-labeled with CD63 (green) for MVBs and late endosomes. Scale bar: 10 μm. White boxes are zooms of corresponding images to visualize yellow puncta representing the colocalization between PD-L1 and CD63 (white arrows). Zoom scale bar: 2 μm

To investigate these dynamics, H1975 and A549 cells were incubated with AF647-atezolizumab at critical time points (10 minutes, 2 hours, 6 hours, and 24 hours) to track the fate of PD-L1 following internalization.

In H1975 cells, PD-L1 exhibits a well-defined trafficking pattern following internalization, moving from early endosomes to late endosomes and lysosomes, as shown in Figure 6.27. Membrane-bound PD-L1 does not colocalize with CD63 and is likely sequestered in early endocytic vesicles, still proximal to the membrane, prior to being directed to deeper intracellular compartments. By 2 hours, a significant fraction of PD-L1 has been internalized, although the signal at the plasma membrane remains detectable.

Colocalization with CD63-positive organelles becomes evident in the perinuclear region, indicating that a subset of PD-L1 has reached late endosomes or lysosomal compartments and may be sorted for degradation at this stage (yellow puncta in Figure 6.27B). A strong colocalization is still present at 6 hours, with clusters predominantly localized in the perinuclear region and concentrated on one side of the nucleus. As already observed, by 24 hours, the distribution of PD-L1 appears more widespread throughout the cell, with some clusters remaining in the perinuclear region and other apparently moving towards the membrane. This redistribution might indicate that while PD-L1 is still undergoing degradation in lysosomal compartments, some internalized PD-L1 may be redirected toward recycling compartments at this later stage.

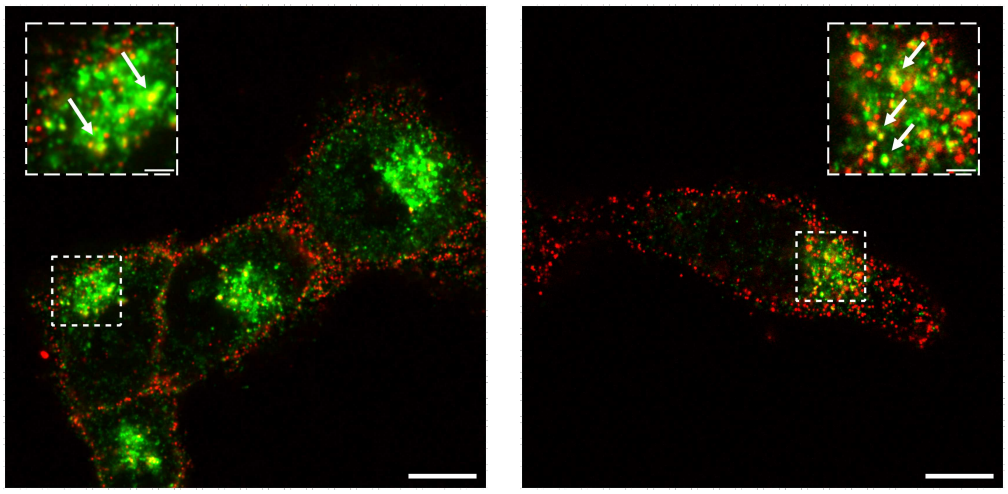

(A) *10 minutes* **(B)** *2 hours*

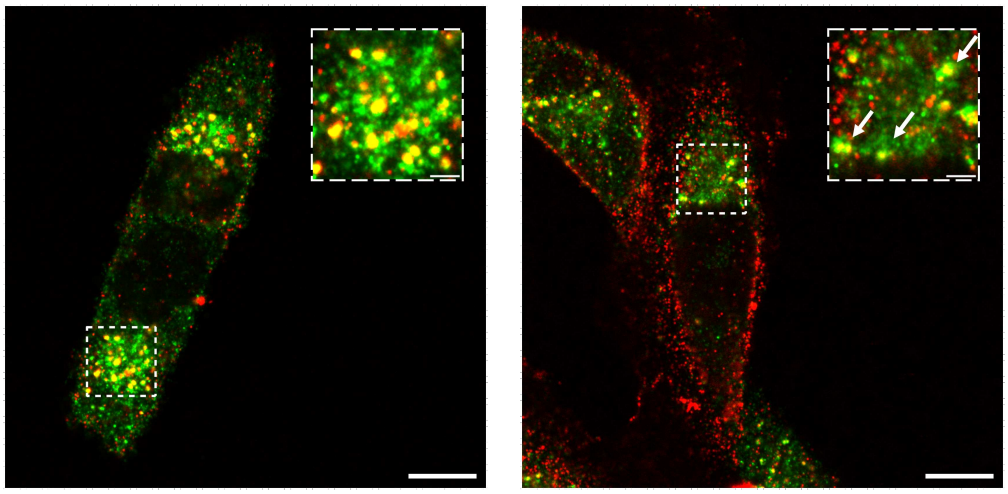

(C) *6 hours* **(D)** *24 hours*

Figure 6.28: Confocal images of A549 cells showing PD-L1 colocalization with CD63-positive organelles. Cells were incubated with AF647-atezolizumab (red) for 10 minutes (A), 2 hours (B), 6 hours (C), and 24 hours (D), fixed, permeabilized, and co-labeled with CD63 (green) for MVBs and late endosomes. Scale bar: 10 μm. White boxes are zooms of corresponding images to visualize yellow puncta representing the colocalization between PD-L1 and CD63 (white arrows). Zoom scale bar: 2 μm

In contrast to H1975, where the redistribution of PD-L1 suggests a shift toward recycling compartments at later stages, A549 cells exhibit a distinctive pattern of PD-L1 trafficking characterized by a pronounced

one-sided clustering of CD63-positive organelles, typically located on one side of the nucleus (Figure 6.28). This striking asymmetry suggests a highly organized intracellular sorting mechanism for PD-L1 that differs from the other cell line. Surprisingly, small yellow puncta are detectable even at the very early stages of endocytic dynamics, and a similar pattern persists at 2 hours mark. This observation indicates that PD-L1 might be rapidly transported into or in proximity to CD63-stained lysosomes or MVBs, occurring at a rate faster than typically expected. This accelerated transport raises the possibility of an equally rapid exocytosis rate, which could help maintain surface levels of PD-L1. As observed in H1975 cells, the strongest colocalization between PD-L1 and CD63-positive vesicles is observed at 6 hours in the perinuclear region, potentially reflecting further progression of PD-L1 into MVBs or lysosomal compartments. By 24 hours, although the overall colocalization decreases, yellow clusters remain localized predominantly on one side of the nucleus (Figures 6.28 C-D). This sustained colocalization over time supports the notion of continuous sorting of PD-L1 toward lysosomes and possibly MVBs, even at the later stages of the endocytic pathway.

The specificity of the observed colocalization between PD-L1 and CD63 in both cell lines was validated through a control experiment, where cells were co-stained with AF647-atezolizumab and the AF488-labeled secondary antibody (without the CD63 primary antibody). In this control, only a weak nonspecific signal from the secondary antibody was detected (Figure 6.29), confirming the reliability of our results.

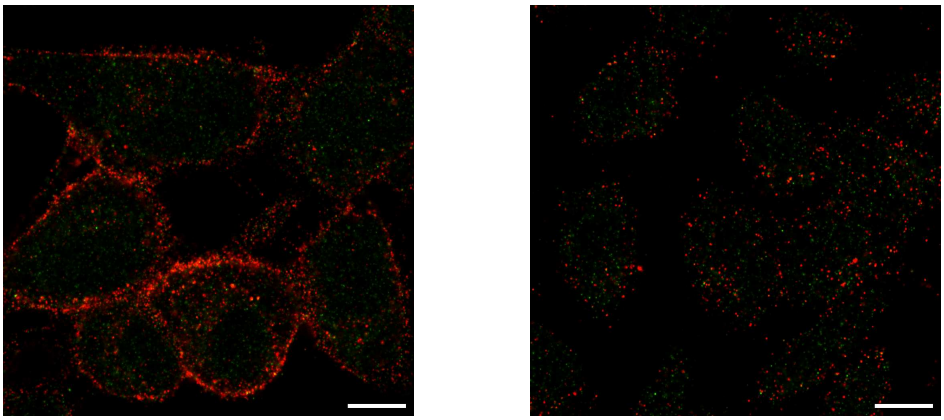

(A) *H1975 Cells* **(B)** *A549 Cells*

Figure 6.29: Control confocal images for colocalization specificity in H1975 (A) and A549 (B) cells. Cells were co-stained with AF647-atezolizumab (red) and an AF488-labeled secondary antibody (green), without the CD63 primary antibody. Only a weak nonspecific signal from the secondary antibody was detected, confirming the specificity of the observed colocalization in previous experiments. Scale bar: 10 μm.

6.7.3 Final Considerations

The intracellular trafficking of PD-L1 refers to the processes that regulate its movement, distribution, and degradation within cells after it is synthesized or internalized. Recent studies have elucidated the dynamic modulation of PD-L1 levels on the cell surface, which directly influences immune evasion

strategies. For instance, palmitoylation of PD-L1 has been shown to enhance its stability and promote its recycling back to the cell membrane, potentially contributing to immune evasion[163]. Another study identified the CMTM6 protein as a key regulator of PD-L1 surface expression, with its upregulation promoting PD-L1 recycling only 10-15 minutes after internalization. This pathway contributes to sustain PD-L1 availability on the cell surface[162]. Interestingly, membrane-bound PD-L1 has been observed to undergo continue internalization through ligand binding-independent processes as well[9]. In light of that, understanding PD-L1's trafficking is crucial because its localization, both on the cell surface and within intracellular compartments, directly impacts its role in immune evasion and its susceptibility to therapies, including photoimmunotherapy[164].

The findings presented in this study provide valuable insights into the intricate dynamics of PD-L1 trafficking in NSCLC cells, revealing unexpected differences in intracellular sorting and degradation mechanisms between the H1975 and A549 cell lines. H1975 cells demonstrate a dual mechanism where PD-L1 can be both recycled and degraded. The formation of clusters that disappear at later stages of endocytosis (likely representing MVBs that are positive for CD63) aligns with exosome formation. However, MVBs can fuse with either lysosomes or the plasma membrane, and co-staining all these structures with specific markers will be essential to confirm exosomal secretion. In contrast, A549 cells show a pattern of sustained and increasing colocalization of PD-L1 with LysoTracker and CD63-positive organelles over time, suggesting a more definitive pathway towards lysosomal degradation with no evidence of recycling. This is further supported by the absence of clusters and the confined localization of CD63-positive organelles in the perinuclear region.

This divergence in trafficking behavior between the two cell lines underscores the role of intrinsic cellular characteristics in modulating the efficacy of PD-L1-targeted therapies, such as atezolizumab[161]. The implications of these findings have particular relevance in the context of cancer immunotherapy, where PD-L1 expression levels on tumor cells are critical for therapeutic response[5]. Studies have shown that increased PD-L1 recycling correlates with poor response to immune checkpoint inhibitors, as it sustains elevated PD-L1 levels on the tumor surface, promoting immune evasion. A recent study has emphasized the role of exosomal PD-L1 secreted by diffuse large B-cell lymphoma cells, demonstrating that this exosomal PD-L1 can interact with PD-1 receptors on T-cells, further contributing to T-cell inactivation alongside PD-L1 on the tumor cell surface[165]. Conversely, manipulating PD-L1 trafficking to favor degradation of PD-L1 can lead to a decrease in immune suppression, thereby facilitating a more effective anti-tumor immune response[9,164]. Moreover, differences in PD-L1 trafficking dynamics may reflect broader cellular signaling pathways that govern PD-L1 regulation, as previous research has shown that the TME and cytokine signaling can influence PD-L1 expression and degradation.

It is important to note, however, that these experiments are still ongoing and therefore cannot yet serve as conclusive proof of our hypothesis. Repeating these experiments to obtain a robust statistical base will be essential, especially to enable more quantitative analyses of the extent of colocalization between

CD63 and PD-L1. Despite these limitations, the current results provide a strong initial indication of CD63 colocalization with PD-L1, allowing us to present representative images as preliminary data. Future studies should aim to elucidate the molecular pathways underpinning these trafficking dynamics, potentially identifying novel therapeutic targets to enhance the efficacy of PD-L1 blockade. Additionally, exploring the impact of other regulatory proteins and post-translational modifications on PD-L1 trafficking will be essential for developing strategies that can effectively modulate PD-L1 levels and improve patient outcomes in NSCLC[164].

Chapter 7

Conclusions

In this thesis, we explored the potential of a novel light-sensitive supramolecular complex designed to target PD-L1 for photoimmunotherapy in NSCLC. By conjugating the PS eosin-5-isothiocyanate (EITC) to atezolizumab, an FDA-approved immune checkpoint inhibitor, we aimed to develop a therapeutic platform that combines localized, light-induced cytotoxicity with immune modulation via PD-L1 inhibition. Our findings demonstrated the impact of PD-L1 expression levels on therapeutic efficacy and highlighted PCI's role in enhancing PDT outcomes. The following conclusions summarize the most significant results and their implications:

1. The EITC-atezolizumab Conjugate is a Promising Candidate for Photoimmunotherapy

Our results demonstrated that the EITC-atezolizumab conjugate effectively combines photosensitization with PD-L1 targeting, supporting its use in integrated PDT and immune checkpoint therapy. The conjugate efficiently generates $^1O_2$, with a quantum yield of 0.11, and selectively targets PD-L1-expressing cells. *In vitro* experiments on NSCLC cells confirmed a dose-dependent reduction in cell viability due to ROS generation upon light exposure. Additionally, by conjugating the PS to atezolizumab, the cytotoxic effects are confined to PD-L1-expressing cells, minimizing off-target damage and improving therapeutic specificity. This targeted approach underscores the importance of receptor-mediated drug delivery in oncology, where balancing efficacy and safety is paramount. Another key advantage of this immunoconjugate lies in its versatility. While this study focused on PD-L1 targeting in NSCLC, the platform can be adapted for use in various cancers where PD-L1 is overexpressed, such as melanoma, colorectal, and breast cancers. Beyond PD-L1 targeting, this conjugation methodology is also adaptable to other monoclonal antibodies, PSs, and even theranostic agents, broadening potential applications to different immune targets and cancer types.

2. PD-L1 Density Alone Does Not Predict PDT Efficacy

In this study, we developed a quantitative approach to measure PD-L1 receptor density at the nanoscale

level using dSTORM. This high-resolution imaging technique allowed us to quantify PD-L1 receptors per square micrometer on the cell surface, a significant improvement over traditional methods like flow cytometry that provide only qualitative or bulk population-level data. By correlating these precise measurements with therapeutic outcomes, we were able to demonstrate that receptor density alone is an unreliable predictor of PDT efficacy, underscoring the need for multifactorial biomarkers. Cells with high PD-L1 expression did show slightly greater susceptibility to treatment, but the increase in cytotoxicity was marginal compared to cells with lower PD-L1 expression, suggesting that factors beyond PD-L1 density play a larger role in determining the overall treatment efficacy. This is an important observation because it broadens the potential application of EITC-atezolizumab to many cancers, particularly those with heterogeneous or low PD-L1 expression that are often excluded from PD-L1-targeted therapies. Additionally, this finding underscores the potential advantage of combining PDT with immune checkpoint inhibition to provide a two-pronged attack that can potentially overcome the limitations faced by immune checkpoint inhibitors in cases where PD-L1 expression is not high enough to ensure strong immune response activation but where direct cytotoxic effects can still induce meaningful tumor cell death.

3. Photochemical Internalization Enhances PDT Efficacy but Does Not Synergize with PD-L1 Blockade

Photochemical internalization (PCI) was evaluated as a strategy to enhance therapeutic delivery by promoting endosomal escape. While PCI improved the internalization of molecules such as gelonin, it did not show significant synergy when combined with the EITC-Atezolizumab conjugate. This lack of synergy may be due to PD-L1 recycling, which allows the receptor to return to the cell surface after initial internalization, potentially limiting the sustained impact of PD-L1-targeted therapies.

4. PD-L1 Recycling May Be a Key Factor in Therapeutic Outcomes

Our study on PD-L1 trafficking provided valuable insights into the recycling and degradation pathways following atezolizumab binding. We observed that PD-L1 is directed to lysosomal compartments for partial degradation, but a fraction of the receptor is recycled back to the cell surface in some subtypes of NSCLC cells. This recycling could diminish the overall efficacy of PD-L1-targeted therapies, as tumor cells may retain functional PD-L1 even after treatment. Understanding PD-L1 trafficking dynamics is critical for optimizing therapies that target this immune checkpoint. Future strategies could focus on inhibiting PD-L1 recycling or enhancing its degradation to improve long-term therapeutic outcomes.

Despite the promising results, several limitations remain. Future research should focus on optimizing dosing and light exposure, potentially by exploring more potent PSs or more efficient light delivery systems. Furthermore, translating these findings to animal models will be a critical step to investigate the conjugate's performance *in vivo*, where pharmacokinetics, biodistribution, safety

profiles, and the clinical potential of this approach can be assessed. Additionally, more research on PD-L1 trafficking mechanisms will be essential for developing strategies to block receptor recycling and improve long-term therapeutic outcomes.

In conclusion, this thesis has demonstrated the feasibility of using a PS conjugated to an immune checkpoint inhibitor for targeted cancer therapy. Combining PDT with immune modulation offers a powerful, multi-pronged approach to cancer treatment. The adaptability of the conjugation platform to various antibodies and PSs paves the way for the development of personalized therapies tailored to individual tumors. The theranostic potential of this approach, enabling both therapeutic and diagnostic capabilities, further enhances its clinical value, offering more precise and effective cancer management. Overall, this work contributes to the ongoing evolution of personalized oncology through targeted, light-activated therapies.

Bibliography

[1] F. Bray, M. Laversanne, H. Sung, J. Ferlay, R.L. Siegel, I. Soerjomataram, and A. Jemal. Global cancer statistics 2022: GLOBOCAN estimates of incidence and mortality worldwide for 36 cancers in 185 countries. *CA Cancer J Clin.*, 74(3):229–263, 2024.

[2] O. Rodak, M.D. Peris-Díaz, M. Olbromski, M. Podhorska-Okołów, and P. Dziegiel. Current landscape of non-small cell lung cancer: Epidemiology, histological classification, targeted therapies, and immunotherapy. *Cancers (Basel).*, 13(18):4705, 2021.

[3] D. Mew, C.K. Wat, G.H. Towers, and J.G. Levy. Photoimmunotherapy: treatment of animal tumors with tumor-specific monoclonal antibody-hematoporphyrin conjugates. *J Immunol.*, 130(3):1473–1477, 1983.

[4] A. Mussini, E. Uriati, P. Bianchini, A. Diaspro, L. Cavanna, S. Abbruzzetti, and C. Viappiani. Targeted photoimmunotherapy for cancer. *Biomol Concepts.*, 13(1):126–147, 2022.

[5] S. Taki, K. Matsuoka, Y. Nishinaga, K. Takahashi, H. Yasui, C. Koike, M. Shimizu, M. Sato, and K. Sato. Spatiotemporal depletion of tumor-associated immune checkpoint PD-L1 with near-infrared photoimmunotherapy promotes antitumor immunity. *J Immunother Cancer.*, 9(11):e003036, 2021.

[6] L. Woythe, P. Madhikar, N. Feiner-Gracia, C. Storm, and L. Albertazzi. A single-molecule view at nanoparticle targeting selectivity: Correlating ligand functionality and cell receptor density. *ACS Nano.*, 16(3):3785–3796, 2022.

[7] X. Zhao, Y. Bao, B. Meng, Z. Xu, S. Li, X. Wang, R. Hou, W. Ma, D. Liu, J. Zheng, and M. Shi. From rough to precise: PD-L1 evaluation for predicting the efficacy of PD-1/PD-L1 blockades. *Front Immunol.*, 13:920021, 2022.

[8] K. Berg, P.K. Selbo, L. Prasmickaite, T.E. Tjelle, K. Sandvig, J. Moan, G. Gaudernack, O. Fodstad, S. Kjølsrud, H. Anholt, G.H. Rodal, S.K. Rodal, and A. Høgset. Photochemical internalization: a novel technology for delivery of macromolecules into cytosol. *Cancer Res.*, 59(6):1180–1183, 1999.

[9] Z. Ye, Y. Xiong, W. Peng, W. Wei, L. Huang, J. Yue, C. Zhang, G. Lin, F. Huang, L. Zhang, S. Zheng, and J. Yue. Manipulation of PD-L1 endosomal trafficking promotes anticancer immunity. *Adv Sci (Weinh).*, 10(6):e2206411, 2023.

[10] T. Yang, Y. Xiong, Y. Zeng, Y. Wang, J. Zeng, J. Liu, S. Xu, and L.S. Li. Current status of immunotherapy for non-small cell lung cancer. *Front Pharmacol.*, 13:989461, 2022.

[11] American Cancer Society. Non-small cell lung cancer stages. `https://www.cancer.org/cancer/types/lung-cancer/detection-diagnosis-staging/staging-nsclc.html`. Accessed: 2024-01-29.

[12] R. Bai, Z. Lv, D. Xu, and J. Cui. Predictive biomarkers for cancer immunotherapy with immune checkpoint inhibitors. *Biomark Res.*, 8:34, 2020.

[13] G. Gunaydin, M.E. Gedik, and S. Ayan. Photodynamic therapy-current limitations and novel approaches. *Front Chem.*, 9:691697, 2021.

[14] O. Raab. Uber die wirkung fluoreszierender stoffe auf infusorien. *Z. Biol*, 39:524–546, 1900.

[15] H. Von Tappeiner and A. Jesionek. Therapeutische versuche mit fluoreszeirenden stoffen. *Muench. Med. Wochenschr*, 47:2042–2044, 1903.

[16] H. von Tappeiner and J. Ueber. Wirkung der photodynamischen(fluorescierenden) stoffe auf protozoan und enzyme. *Drsch Arch Klin Med.*, 80:427–487, 1904.

[17] H. von Tappeiner and J. Die. Sensibilisierende wirkung fluorescierender substanzer. Gasammerre unter suchungen uber die phorodynamische erscheinung. *Leipzig: FCW Vogel*, 1907.

[18] T.J. Dougherty, C.J. Gomer, B.W. Henderson, G. Jori, D. Kessel, M. Korbelik, J. Moan, and Q. Peng. Photodynamic therapy. *J Natl Cancer Inst.*, 90(12):899–905, 1998.

[19] P. Agostinis, K. Berg, K.A. Cengel, T.H. Foster, A.W. Girotti, S.O. Gollnick, S.M. Hahn, M.R. Hamblin, A. Juzeniene, D. Kessel, M. Korbelik, J. Moan, P. Mroz, D. Nowis, J. Piette, B.C. Wilson, and J. Golab. Photodynamic therapy of cancer: an update. *CA Cancer J Clin*, 61(4):250–81, 2011.

[20] A.P. Castano, T.N. Demidova, and M.R. Hamblin. Mechanisms in photodynamic therapy: Part three-photosensitizer pharmacokinetics, biodistribution, tumor localization and modes of tumor destruction. *Photodiagnosis Photodyn Ther.*, 2(2):91–106, 2005.

[21] N. Mariño-Ocampo, L. Dibona-Villanueva, E. Escobar-Álvarez, and et al. Recent photosensitizer developments, delivery strategies and combination-based approaches for photodynamic therapy. *Photochem Photobiol.*, 99(2):469–497, 2023.

[22] A. Mussini, E. Uriati, C. Hally, S. Nonell, P. Bianchini, A. Diaspro, S. Pongolini, P. Delcanale, S. Abbruzzetti, and C. Viappiani. Versatile supramolecular complex for targeted antimicrobial photodynamic inactivation. *Bioconjug Chem.*, 33(4):666–676, 2022.

[23] P. Delcanale, E. Uriati, M. Mariangeli, A. Mussini, A. Moreno, D. Lelli, L. Cavanna, P. Bianchini, A. Diaspro, S. Abbruzzetti, and C. Viappiani. The interaction of Hypericin with SARS-Cov-2 reveals a multimodal antiviral activity. *ACS Appl Mater Interfaces.*, 14(12):14025–14032, 2022.

[24] L.M. Baltazar, A. Ray, D.A. Santos, P.S. Cisalpino, A.J. Friedman, and J.D. Nosanchuk. Antimicrobial photodynamic therapy: an effective alternative approach to control fungal infections. *Front Microbiol.*, 6:202, 2015.

[25] J.H. Correia, J.A. Rodrigues, S. Pimenta, T. Dong, and Z. Yang. Photodynamic therapy review: Principles, photosensitizers, applications, and future directions. *Pharmaceutics.*, 13(9):1332, 2021.

[26] R.M. Eisberg and R. Resnick. *Quantum Physics of Atoms, Molecules, Solids, Nuclei and Particles.* Wiley, 1985.

[27] Edinburgh Instruments. A typical jablonski diagram showing the possible radiative and non-radiative transitions. `https://www.edinst.com/us/blog/jablonski-diagram-2/`. Accessed: 2023-02-14.

[28] Gilbert N. Lewis and M. Kasha. Phosphorescence and the triplet state. *J. Am. Chem. Soc.*, 66(12):2100–2116, 1944.

[29] Mostafa A. El-Sayed. Triplet state. its radiative and nonradiative properties. *Acc. Chem. Res.*, 1(1):8–16, 1968.

[30] Joseph R. Lakowicz. *Principles of fluorescence spectroscopy.* Lakowicz, Joseph R., 1983.

[31] W.T. Borden, R. Hoffmann, T. Stuyver, and B. Chen. Dioxygen: What makes this triplet diradical kinetically persistent? *Journal of the American Chemical Society*, 139(26):9010–9018, 2017.

[32] F. Wilkinson, W.P. Helman, and A.B. Ross. Rate constants for the decay and reactions of the lowest electronically excited singlet state of molecular oxygen in solution. an expanded and revised compilation. *J. Phys. Chem. Ref. Data*, 24:663–677, 1995.

[33] P. Ogilby and K. Mikkelsen. Singlet sigma: The “other” singlet oxygen in solution. *Photochemistry and Photobiology*, 70(4):369–379, 1999.

[34] J.W. Snyder, E. Skovsen, J. Lambert, L. Poulsena, and P.R. Ogilby. Optical detection of singlet oxygen from single cells. *Phys. Chem. Chem. Phys.*, 8:4280–4293, 2006.

[35] M. Niedre, M.S. Patterson, and B.C. Wilson. Direct near-infrared luminescence detection of singlet oxygen generated by photodynamic therapy in cells in vitro and tissues in vivo. *Photochem Photobiol.*, 75(4):382–391, 2002.

[36] S. Kim, M. Fujitsuka, and T. Majima. Photochemistry of singlet oxygen sensor green. *J Phys Chem B.*, 117(45):13985–13992, 2013.

[37] S. Suzen, H. Gurer-Orhan, and L. Saso. Detection of reactive oxygen and nitrogen species by electron paramagnetic resonance (EPR) technique. *Molecules.*, 22(1):181, 2017.

[38] J.R. Kanofsky and P. Sima. Singlet oxygen production from the reactions of ozone with biological molecules. *Journal of biological chemistry*, 266(14):9039–9042, 1991.

[39] C. Pierlot, J. Barbillat, V. Nardello-Rataj, and et al. Optimisation of the chemical generation of singlet oxygen ($^1O_2$, $^1\Delta g$) from the hydrogen peroxide-lanthanum III catalytic system using an improved NIR spectrometer. *Photochem Photobiol Sci*, 8:1024–1031, 2009.

[40] A.M. Held, D.J. Halko, and J.K. Hurst. Mechanisms of chlorine oxidation of hydrogen peroxide. *J. Am. Chem. Soc.*, 100(18):5732–5740, 1978.

[41] H. Jablonowski, J. Santos Sousa, KD. Weltmann, and et al. Quantification of the ozone and singlet delta oxygen produced in gas and liquid phases by a non-thermal atmospheric plasma with relevance for medical treatment. *Sci Rep*, 8:12195, 2018.

[42] A.A. Alfadda and RM. Sallam. Reactive oxygen species in health and disease. *J Biomed Biotechnol.*, 2012:936486, 2012.

[43] C Schweitzer and R. Schmidt. Physical mechanisms of generation and deactivation of singlet oxygen. *Chem. Rev.*, 103(5):1685–1758, 2003.

[44] K. Lang, J. Mosinger, and D.M. Wagnerová. Photophysical properties of porphyrinoid sensitizers non-covalently bound to host molecules; models for photodynamic therapy. *Coord. Chem. Rev.*, 248(3–4):321–350, 2004.

[45] M.J. Davies. Reactive species formed on proteins exposed to singlet oxygen. *Photochem. Photobiol. Sci.*, 3:17–25, 2004.

[46] Ogilby P.R. Singlet oxygen: there is indeed something new under the sun. *Chem. Soc. Rev.*, 39:3181–3209, 2010.

[47] J. Moan and K. Berg. The photodegradation of porphyrins in cells can be used to estimate the lifetime of singlet oxygen. *Photochem Photobiol.*, 53(4):549–553, 1991.

[48] A. Baker and J.R. Kanofsky. Quenching of singlet oxygen by biomolecules from L1210 leukemia cells. *Photochem Photobiol.*, 55(4):523–528, 1992.

[49] S. Hatz, L. Poulsen, and P.R. Ogilby. Time-resolved singlet oxygen phosphorescence measurements from photosensitized experiments in single cells: Effects of oxygen diffusion and oxygen concentration. *Photochem Photobiol.*, 84:1284–1290, 2008.

[50] I.O.L. Bacellar and M.S. Baptista. Mechanisms of photosensitized lipid oxidation and membrane permeabilization. *ACS Omega*, 4(26):21636–21646, 2019.

[51] P. Di Mascio, G.R. Martinez, S. Miyamoto, G.E. Ronsein, M.H.G. Medeiros, and J. Cadet. Singlet molecular oxygen reactions with nucleic acids, lipids, and proteins. *Chem. Rev.*, 119(3):2043–2086, 2019.

[52] I.B. Matheson, R.D. Etheridge, N.R. Kratowich, and J. Lee. The quenching of singlet oxygen by amino acids and proteins. *Photochem Photobiol.*, 21(3):165–171, 1975.

[53] R.L. Jensen, J. Arnbjerg, and P.R. Ogilby. Reaction of singlet oxygen with tryptophan in proteins: a pronounced effect of the local environment on the reaction rate. *J Am Chem Soc.*, 134(23):9820–9826, 2012.

[54] B. Sjöberg, S. Foley, A. Staicu, A. Pascu, M. Pascu, and M. Enescu. Protein reactivity with singlet oxygen: Influence of the solvent exposure of the reactive amino acid residues. *J Photochem Photobiol B.*, 159:106–110, 2016.

[55] P. Mroz, A. Yaroslavsky, G.B. Kharkwal, and M.R. Hamblin. Cell death pathways in photodynamic therapy of cancer. *Cancers (Basel)*, 3(2):2516–39, 2011.

[56] T. Mishchenko, I. Balalaeva, A. Gorokhova, and et al. Which cell death modality wins the contest for photodynamic therapy of cancer? *Cell Death Dis*, 13:455, 2022.

[57] K. Plaetzer, T. Kiesslich, T. Verwanger, and B. Krammer. The modes of cell death induced by PDT: An overviewr. *Medical Laser Application*, 18(1):7–19, 2003.

[58] R. Scherz-Shouval and Z. Elazar. ROS, mitochondria and the regulation of autophagy. *Trends Cell Biol.*, 17(9):422–427, 2007.

[59] David. Kessel. Pathways to paraptosis after ER photodamage in OVCAR-5 cells. *Photochemistry and Photobiology*, 95:1239–1242, 2019.

[60] H.Z. Lee, W.H. Yang, M.J. Hour, C.Y. Wu, W.H. Peng, B.Y. Bao, P.H. Han, and D.T. Bau. Photodynamic activity of aloe-emodin induces resensitization of lung cancer cells to anoikis. *Eur J Pharmacol.*, 648(1–3):50–58, 2010.

[61] D.E. Dolmans, D. Fukumura, and R.K. Jain. Photodynamic therapy for cancer. *Nat Rev Cancer.*, 3(5):380–387, 2003.

[62] National Cancer Institute at National Institutes of Health, U.S. Department of Health, and Human Services. Definition of photosensitizer - NCI dictionary of cancer terms - NCI. `https://www.cancer.gov/publications/dictionaries/cancer-terms/def/photosensitizer`. Accessed: 2024-02-22.

[63] M.R. Detty, S.L. Gibson, and S.J. Wagner. Current clinical and preclinical photosensitizers for use in photodynamic therapy. *J Med Chem.*, 47(16):3897–3915, 2004.

[64] R.R. Allison and C.H. Sibata. Oncologic photodynamic therapy photosensitizers: a clinical review. *Photodiagnosis Photodyn Ther.*, 7(2):61–75, 2010.

[65] A.E. O'Connor, W.M. Gallagher, and A.T. Byrne. Porphyrin and nonporphyrin photosensitizers in oncology: Preclinicaland clinical advances in photodynamic therapy. *Photochemistry and Photobiology*, 85:1053–1074, 2009.

[66] A.B. Ormond and H.S. Freeman. Dye sensitizers for photodynamic therapy. *Materials (Basel)*, 6(3):817–840, 2013.

[67] S. D'Alessandro and R. Priefer. Non-porphyrin dyes used as photosensitizers in photodynamic therapy. *J. Drug Deliv. Sci. Technol.*, 60:101979, 2020.

[68] Q. Pan, K. Li, X. Cheng, L. Chen, Q. Yu, H. Fan, L. Zheng, Z. Yang, and F. Ni. A photoactivatable antibody-Chlorin e6 conjugate enabling singlet oxygen production for tumor-targeting photodynamic therapy. *Biomed Mater.*, 16(4), 2021.

[69] J. Karges. Clinical development of metal complexes as photosensitizers for photodynamic therapy of cancer. *Angew Chem Int Ed Engl.*, 61(5):e202112236, 2022.

[70] S.R. Alves, I.R. Calori, and A.C. Tedesco. Photosensitizer-based metal-organic frameworks for highly effective photodynamic therapy. *Materials Science Engineering C*, 131:112514, 2021.

[71] L. Benov. Photodynamic therapy: current status and future directions. *Med Princ Pract.*, 24 Suppl 1(Suppl 1):14–28, 2015.

[72] J.S. Friedberg, R. Mick, J.P. Stevenson, T. Zhu, T.M. Busch, D. Shin, D. Smith, M. Culligan, A. Dimofte, E. Glatstein, and S.M. Hahn. Phase ii trial of pleural photodynamic therapy and surgery for patients with non-small-cell lung cancer with pleural spread. *J Clin Oncol.*, 22(11):2192–2201, 2004.

[73] D. Luo, K.A. Carter, D. Miranda, and J.F. Lovell. Chemophototherapy: An emerging treatment option for solid tumors. *Adv Sci (Weinh)*, 4(1):1600106, 2016.

[74] D. Viswanath and Y.Y. Won. Combining radiotherapy (RT) and photodynamic therapy (PDT): Clinical studies on conventional RT-PDT approaches and novel nanoparticle-based RT-PDT approaches under preclinical evaluation. *ACS Biomater Sci Eng.*, 8(9):3644–3658, 2022.

[75] H.S. Hwang, H. Shin, J. Han, and K. Na. Combination of photodynamic therapy (PDT) and anti-tumor immunity in cancer therapy. *J Pharm Investig.*, 48(2):143–151, 2018.

[76] M. Overchuk, R.A. Weersink, B.C. Wilson, and G. Zheng. Photodynamic and photothermal therapies: Synergy opportunities for nanomedicine. *ACS Nano.*, 17(9):7979–8003, 2023.

[77] V. Vilas-Boas, F. Carvalho, and B. Espiña. Magnetic hyperthermia for cancer treatment: Main parameters affecting the outcome of in vitro and in vivo studies. *Molecules.*, 25(12):2874, 2020.

[78] Y. Zheng, J. Ye, Z. Li, H. Chen, and Y. Gao. Recent progress in sono-photodynamic cancer therapy: From developed new sensitizers to nanotechnology-based efficacy-enhancing strategies. *Acta Pharm Sin B.*, 11(8):2197–2219, 2021.

[79] J.S. Marshall, R. Warrington, W. Watson, and H.L. Kim. An introduction to immunology and immunopathology. *Allergy, Asthma Clinical Immunology*, 14 (Suppl 2)(49), 2018.

[80] D.M. Pardoll. The blockade of immune checkpoints in cancer immunotherapy. *Nat Rev Cancer.*, 12(4):252–264, 2012.

[81] S.R.G. Fernandes, R. Fernandes, B. Sarmento, and J.P.C. Pereira, P.M.R.and Tomé. Photoimmunoconjugates: novel synthetic strategies to target and treat cancer by photodynamic therapy. *Org Biomol Chem.*, 17(10):2579–2593, 2019.

[82] M. Mitsunaga, M. Ogawa, N. Kosaka, L.T. Rosenblum, P.L. Choyke, and H. Kobayashi. Cancer cell-selective in vivo near infrared photoimmunotherapy targeting specific membrane molecules. *Nat Med.*, 17(12):1685–1691, 2011.

[83] Y. Maruoka, H. Wakiyama, P.L. Choyke, and H. Kobayashi. Near infrared photoimmunotherapy for cancers: A translational perspective. *EBioMedicine.*, 70:103501, 2021.

[84] T. Nagaya, S. Okuyama, F. Ogata, Y. Maruoka, P.L. Choyke, and H. Kobayashi. Endoscopic near infrared photoimmunotherapy using a fiber optic diffuser for peritoneal dissemination of gastric cancer. *Cancer Sci.*, 19(6):1902–1908, 2018.

[85] F.S. Hodi, S.J. O'Day, D.F. McDermott, R.W. Weber, J.A. Sosman, and et al. Haanen, J.B. Improved survival with ipilimumab in patients with metastatic melanoma. *N Engl J Med.*, 363(8):711–723, 2010.

[86] Y. Jiang, M. Chen, H. Nie, and Y. Yuan. PD-1 and PD-L1 in cancer immunotherapy: clinical implications and future considerations. *Hum Vaccin Immunother.*, 15(5):1111–1122, 2019.

[87] A. Zanello, M. Bortolotti, S. Maiello, A. Bolognesi, and L. Polito. Anti-PD-L1 immunoconjugates for cancer therapy: Are available antibodies good carriers for toxic payload delivering? *Front Pharmacol.*, 13:972046, 2022.

[88] A. Matusz-Fisher and A.R. Tan. Combination of HER2-targeted agents with immune checkpoint inhibitors in the treatment of HER2-positive breast cancer. *Expert Opin Biol Ther.*, 22(3):385–395, 2022.

[89] L. Ulfo, P.E. Costantini, M. Di Giosia, A. Danielli, and M. Calvaresi. EGFR-targeted photodynamic therapy. *Pharmaceutics.*, 14(10):241, 2022.

[90] P.K. Selbo, A. Weyergang, A. Høgset, O.J. Norum, M.B. Berstad, M. Vikdal, and K. Berg. Photochemical internalization provides time- and space-controlled endolysosomal escape of therapeutic molecules. *J Control Release.*, 148(1):2–12, 2010.

[91] W. Jerjes, T.A. Theodossiou, H. Hirschberg, A. Høgset, A. Weyergang, P.K. Selbo, Z. Hamdoon, C. Hopper, and K. Berg. Photochemical internalization for intracellular drug delivery. From basic mechanisms to clinical research. *J Clin Med.*, 9(2):528, 2020.

[92] G.J. Doherty and H.T. McMahon. Mechanisms of endocytosis. *Annu Rev Biochem.*, 78:857–902, 2009.

[93] K. Berg, A. Høgset, L. Prasmickaite, A. Weyergang, A. Bonsted, A. Dietze, P.J. Lou, S.G. Bown, O.J. Norum, H.M.T. Mollergard, and P.K. Selbo. Photochemical internalization (PCI): a novel technology for activation of endocytosed therapeutic agents. *Med. Laser Appl.*, 21(4):239–250, 2006.

[94] L. Prasmickaite, A. Høgset, P.K. Selbo, B.Ø. Engesaeter, M. Hellum, and K. Berg. Photochemical disruption of endocytic vesicles before delivery of drugs: a new strategy for cancer therapy. *Br J Cancer.*, 86(4):652–657, 2002.

[95] K. Berg, S. Nordstrand, P.K. Selbo, D.T. Tran, E. Angell-Petersen, and A. Høgset. Disulfonated tetraphenyl chlorin (TPCS2a), a novel photosensitizer developed for clinical utilization of photochemical internalization. *Photochem Photobiol Sci.*, 10(10):1637–1651, 2011.

[96] A.A. Sultan, W. Jerjes, K. Berg, A. Høgset, C.A. Mosse, R. Hamoudi, Z. Hamdoon, C. Simeon, D. Carnell, M. Forster, and C. Hopper. Disulfonated tetraphenyl chlorin (TPCS2a)-induced photochemical internalisation of bleomycin in patients with solid malignancies: a phase 1, dose-escalation, first-in-man trial. *Lancet Oncol.*, 17(9):1217–1229, 2016.

[97] J. Trojan, A. Hoffmeister, B. Neu, S. Kasper, A. Dechêne, C. Jürgensen, J. Schirra, R. Jakobs, D. Palmer, P.K. Selbo, H. Olivecrona, L. Finnesand, A. Høgset, P. Walday, and R. Sturgess. Photochemical internalization of gemcitabine is safe and effective in locally advanced inoperable cholangiocarcinoma. *Oncologist.*, 27(6):430–433, 2022.

[98] T. Otterhaug, S. Janetzki, M.J.P. Welters, M. Håkerud, A.G. Nedberg, V.T. Edwards, S. Boekestijn, N.M. Loof, P.K. Selbo, H. Olivecrona, S.H. van der Burg, and A. Høgset. Photochemical internalization enhanced vaccination is safe, and gives promising cellular immune responses to an HPV peptide-based vaccine in a phase i clinical study in healthy volunteers. *Front Immunol.*, 11:576756, 2021.

[99] P.K. Selbo, K. Sandvig, V. Kirveliene, and K. Berg. Release of gelonin from endosomes and lysosomes to cytosol by photochemical internalization. *Biochim Biophys Acta.*, 1475(3):307–313, 2000.

[100] A. Dietze, A. Bonsted, A. Høgset, and K. Berg. Photochemical internalization enhances the cytotoxic effect of the protein toxin gelonin and transgene expression in sarcoma cells. *Photochem Photobiol.*, 78(3):283–289, 2003.

[101] J.J.W. Wong and P.K. Selbo. Light-controlled elimination of PD-L1+ cells. *J Photochem Photobiol B.*, 225:112355, 2021.

[102] P.K. Selbo, G. Sivam, O. Fodstad, K. Sandvig, and K. Berg. In vivo documentation of photochemical internalization, a novel approach to site specific cancer therapy. *Int J Cancer.*, 92(5):761–766, 2001.

[103] P.K. Selbo, G. Sivam, O. Fodstad, K. Sandvig, and K. Berg. Photochemical internalisation increases the cytotoxic effect of the immunotoxin MOC31-gelonin. *Int J Cancer.*, 87(6):253–259, 2000.

[104] A. Weyergang, P.K. Selbo, and K. Berg. Photochemically stimulated drug delivery increases the cytotoxicity and specificity of EGF-saporin. *J Control Release.*, 111(1-2):165–173, 2006.

[105] W.L. Yip, A. Weyergang, K. Berg, H.H. Tønnesen, and P.K. Selbo. Targeted delivery and enhanced cytotoxicity of cetuximab-saporin by photochemical internalization in EGFR-positive cancer cells. *Mol Pharm.*, 4(2):241–251, 2007.

[106] A. Weyergang, A.S. Fremstedal, E. Skarpen, Q. Peng, K.A. Mohamedali, M.S. Eng, L.H. Cheung, M.G. Rosenblum, J. Waltenberger, and K. Berg. Light-enhanced VEGF121/rGel: A tumor targeted modality with vascular and immune-mediated efficacy. *J Control Release.*, 288:161–172, 2018.

[107] B. Fan, W. Peng, Y. Zhang, P. Liu, and J. Shen. ROS conversion promotes the bactericidal efficiency of eosin Y based photodynamic therapy. *Biomater. Sci.*, 11:4930–4937, 2023.

[108] G.A. Johnson, N. Muthukrishnan, and J.P. Pellois. Photoinactivation of Gram positive and Gram negative bacteria with the antimicrobial peptide (KLAKLAK)(2) conjugated to the hydrophilic photosensitizer eosin Y. *Bioconjug Chem.*, 24(1):114–123, 2013.

[109] G. López-Pea, S. Simón-Fuente, D.H. Ortgies, M.Á. Moliné, E. Martín Rodríguez, F. Sanz-Rodríguez, and M. Ribagorda. Eosin Y-functionalized upconverting nanoparticles: Nanophotosensitizers and deep tissue bioimaging agents for simultaneous therapeutic and diagnostic applications. *Cancers (Basel)*, 15(1):102, 2022.

[110] P. Delcanale, M.M. Alampi, A. Mussini, C. Fumarola, M. Galetti, P.G. Petronini, C. Viappiani, S. Bruno, and S. Abbruzzetti. A photoactive supramolecular complex targeting PD-L1 reveals a weak correlation between photoactivation efficiency and receptor expression levels in Non-Small-Cell Lung Cancer tumor models. *Pharmaceutics*, 15:2776, 2023.

[111] K.M. Zak, R. Kitel, S. Przetocka, P. Golik, K. Guzik, B. Musielak, A. Dömling, G. Dubin, and T.A. Holak. Structure of the complex of human Programmed Death 1, PD-1, and its ligand PD-L1. *Structure*, 23(12):2341–2348, 2015.

[112] T. Azuma, S. Yao, G. Zhu, A.S. Flies, S.J. Flies, and L. Chen. B7-H1 is a ubiquitous antiapoptotic receptor on cancer cells. *Blood.*, 111(7):3635–3643, 2008.

[113] M. Gato-Caas, M. Zuazo, H. Arasanz, M. Ibañez-Vea, L. Lorenzo, G. Fernandez-Hinojal, R. Vera, C. Smerdou, E. Martisova, I. Arozarena, and et.al. PD-L1 signals through conserved sequence motifs to overcome interferon-mediated cytotoxicity. *Cell Rep.*, 20(8):1818–1829, 2017.

[114] C. Nieto, B. Miller, N. Alzofon, and et. al. The programmed death ligand 1 interactome demonstrates bidirectional signaling coordinating immune suppression and cancer progression in head and neck squamous cell carcinoma. *J Natl Cancer Inst.*, 115(11):1392–1403, 2023.

[115] S. Jalali, T. Price-Troska, C. Bothun, J. Villasboas, H.J. Kim, Z.Z. Yang, A.J. Novak, H. Dong, and S.M. Ansell. Reverse signaling via PD-L1 supports malignant cell growth and survival in classical Hodgkin lymphoma. *Blood Cancer J.*, 9(3):22, 2019.

[116] W. Yu, Y. Hua, H. Qiu, J. Hao, K. Zou, Z. Li, S. Hu, P. Guo, M. Chen, S. Sui, Y. Xiong, F. Li, J. Lu, W. Guo, G. Luo, and W. Deng. PD-L1 promotes tumor growth and progression by activating WIP and β-catenin signaling pathways and predicts poor prognosis in lung cancer. *Cell Death Dis.*, 11(7):506, 2020.

[117] Y.J. Lee, J.B. Lee, S.J. Ha, and H.R. Kim. Clinical perspectives to overcome acquired resistance to anti-programmed death-1 and anti-programmed death ligand-1 therapy in non-small cell lung cancer. *Mol Cells.*, 44(5):363–373, 2021.

[118] A. Cavazzoni, G. Digiacomo, R. Alfieri, S. La Monica, C. Fumarola, M. Galetti, M. Bonelli, D. Cretella, V. Barili, A. Zecca, E. Giovannetti, M. Fiorentino, M. Tiseo, P.G. Petronini, and A. Ardizzoni. Pemetrexed enhances membrane PD-L1 expression and potentiates T cell-mediated cytotoxicity by anti-PD-L1 antibody therapy in Non-Small-Cell Lung Cancer. *Cancers (Basel)*, 12(3):666, 2020.

[119] Genentech Inc. Tecentriq (Atezolizumab). U.S. Food and Drug Administration website. `https://www.accessdata.fda.gov/scripts/cder/daf/index.cfmevent=overview.process&ApplNo=761041`. Accessed: 2024-04-22.

[120] M. Li, R. Zhao, J. Chen, and et al. Next generation of anti-PD-L1 Atezolizumab with enhanced anti-tumor efficacy in vivo. *Sci. Rep.*, 11:5774, 2021.

[121] F. Zhang, X. Qi, X. Wang, D. Wei, J. Wu, L. Feng, H. Cai, Y. Wang, N. Zeng, T. Xu, A. Zhou, and Y. Zheng. Structural basis of the therapeutic anti-PD-L1 antibody Atezolizumab. *Oncotarget.*, 8(52):90215–90224, 2017.

[122] C.N. Pace, F. Vajdos, L. Fee, G. Grimsley, and T. Gray. How to measure and predict the molar absorption coefficient of a protein. *Protein Sci.*, 4(11):2411–2423, 1995.

[123] X.F. Zhang, J. Zhang, and L. Liu. Fluorescence properties of twenty fluorescein derivatives: lifetime, quantum yield, absorption and emission spectra. *J Fluoresc.*, 24(3):819–826, 2014.

[124] A. Penzkofer, A. Beidoun, and M. Daiber. Intersystem-crossing and excited-state absorption in eosin Y solutions determined by picosecond double pulse transient absorption measurements. *J. Lumin.*, 51(6):297–314, 1992.

[125] G. Porter, E.S. Reid, and C.J. Tredwell. Time resolved fluorescence in the picosecond region. *Chem. Phys. Lett.*, 29(3):469–472, 1974.

[126] F. Wilkinson, W.P. Helman, and A.B. Ross. Quantum yields for the photosensitized formation of the lowest electronically excited singlet state of molecular oxygen in solution. *J. Phys. Chem. Ref. Data*, 22(1):113–262, 1993.

[127] Federal Register. D&C Red no. 21 and D&C Red no. 22. *Federal Register*, 47:53843–53846, 1982.

[128] M. Chakraborty and A.K. Panda. Spectral behaviour of eosin y in different solvents and aqueous surfactant media. *Spectrochim Acta A Mol Biomol Spectrosc.*, 81(1):458–465, 2011.

[129] S. Abbruzzetti, S. Bruno, S. Faggiano, E. Grandi, A. Mozzarelli, and C. Viappiani. Time-resolved methods in biophysics. 2. monitoring haem proteins at work with nanosecond laser flash photolysis. *Photochem Photobiol Sci*, 5:1109–1120, 2006.

[130] S. van de Linde, A. Löschberger, T. Klein, M. Heidbreder, S. Wolter, M. Heilemann, and M. Sauer. Direct stochastic optical reconstruction microscopy with standard fluorescent probes. *Nat Protoc.*, 6(7):991–1009, 2011.

[131] G.T. Dempsey, J.C. Vaughan, K.H. Chen, M. Bates, and X. Zhuang. Evaluation of fluorophores for optimal performance in localization-based super-resolution imaging. *Nat Methods*, 8(12):1027–1036, 2011.

[132] U. Endesfelder and M. Heilemann. Direct stochastic optical reconstruction microscopy (dSTORM). *Methods Mol Biol*, 1251:263–276, 2015.

[133] P. Delcanale, B. Miret-Ontiveros, M. Arista-Romero, S. Pujals, and L. Albertazzi. Nanoscale mapping functional sites on nanoparticles by points accumulation for imaging in nanoscale topography (PAINT). *ACS Nano.*, 12(8):7629–7637, 2018.

[134] K.W. Dunn, M.M. Kamocka, and J.H. McDonald. A practical guide to evaluating colocalization in biological microscopy. *Am J Physiol Cell Physiol.*, 300(4):C723–42, 2011.

[135] R.D. Petty, L.A. Sutherland, E.M. Hunter, and I.A. Cree. Comparison of MTT and ATP-based assays for the measurement of viable cell number. *J Biolumin Chemilumin*, 10(1):29–34, 1995.

[136] S.P.M. Crouch, R. Kozlowski, K.J. Slater, and J. Fletcher. The use of ATP bioluminescence as a measure of cell proliferation and cytotoxicity. *Journal of Immunological Methods*, 160(1):81–88, 1993.

[137] C. Fumarola, S. La Monica, R.R. Alfieri, E. Borra, and G.G. Guidotti. Cell size reduction induced by inhibition of the mTOR/S6K-signaling pathway protects Jurkat cells from apoptosis. *Cell Death Differ.*, 12(10):1344–1357, 2005.

[138] S. Duellman, G. Shultz, J.and Vidugiris, and J. A. Cali. New luminescent assay for detection of reactive oxygen species. *Promega Corporation Web site*, 2013.

[139] P. Bianchini, M. Cozzolino, M. Oneto, L. Pesce, F. Pennacchietti, M. Tognolini, C. Giorgio, S. Nonell, L. Cavanna, P. Delcanale, S. Abbruzzetti, A. Diaspro, and C. Viappiani. Hypericin–Apomyoglobin: An enhanced photosensitizer complex for the treatment of tumor cells. *Biomacromolecules*, 20(5):2024–2033, 2019.

[140] T.J. Deerinck, M.E. Martone, V. Lev-Ram, D.P. Green, R.Y. Tsien, D.L. Spector, S. Huang, and M.H. Ellisman. Fluorescence photooxidation with eosin: a method for high resolution immunolocalization and in situ hybridization detection for light and electron microscopy. *J Cell Biol.*, 126(4):901–910, 1994.

[141] J. Comas-Barceló, B. Rodríguez-Amigo, S. Abbruzzetti, P.D. Rey-Puech, M. Agut, S. Nonell, and C. Viappiani. A self-assembled nanostructured material with photosensitising properties. *RSC Adv.*, 3:17874–17879, 2013.

[142] J. Liu, X. Peng, S. Yang, X. Li, M. Huang, S. Wei, S. Zhang, G. He, H. Zheng, Q. Fan, L. Yang, and H. Li. Extracellular vesicle PD-L1 in reshaping tumor immune microenvironment: biological function and potential therapy strategies. *Cell Commun Signal.*, 20(1):14, 2022.

[143] A.C. Beenen, T. Sauerer, N. Schaft, and J. Dörrie. Beyond cancer: Regulation and function of PD-L1 in health and immune-related diseases. *Int J Mol Sci.*, 23(15):8599, 2022.

[144] K. Paloja, J. Weiden, J. Hellmeier, A.S. Eklund, S.C.M. Reinhardt, I.A. Parish, R. Jungmann, and M.M.C. Bastings. Balancing the nanoscale organization in multivalent materials for functional inhibition of the Programmed Death-1 immune checkpoint. *ACS Nano.*, 18(2):1381–1395, 2024.

[145] M. Ruglioni, S. Civita, T. Salvadori, S. Cristiani, V. Carnicelli, S. Barachini, I. Petrini, I. Nepita, M. Castello, A. Diaspro, P. Bianchini, B. Storti, R. Bizzarri, S. Fogli, and R. Danesi. Nanoscale engagement and clusterization of Programmed death ligand 1 (PD-L1) in the membrane lipid rafts of Non-Small Cell Lung Cancer cells. *bioRxiv*, 2022.

[146] M.N. Andersen, S.N. Al-Karradi, T.W. Kragstrup, and M. Hokland. Elimination of erroneous results in flow cytometry caused by antibody binding to Fc receptors on human monocytes and macrophages. *Cytometry A.*, 89(11):1001–1009, 2016.

[147] T. Nerreter, S. Letschert, R. Gø"tz, S. Doose, S. Danhof, H. Einsele, M. Sauer, and M. Hudecek. Super-resolution microscopy reveals ultra-low CD19 expression on myeloma cells that triggers elimination by CD19 CAR-T. *Nat. Commun.*, 10:3137, 2019.

[148] F. Wäldchen, J. Schlegel, R. Götz, M. Luciano, M. Schnermann, S. Doose, and M. Sauer. Whole-cell imaging of plasma membrane receptors by 3D lattice light-sheet dSTORM. *Nat. Commun.*, 11(1):887, 2020.

[149] N. Ehmann, S. Van de Linde, A. Alon, D. Ljaschenko, X.Z. Keung, T. Holm, A. Rings, A. DiAntonio, S. Hallermann, U. Ashery, M. Heckmann, M. Sauer, and R.J. Kittel. Quantitative super-resolution imaging of Bruchpilot distinguishes active zone states. *Nat. Commun.*, 5:4650, 2014.

[150] P. Delcanale, F. Pennacchietti, G. Maestrini, and et al. Subdiffraction localization of a nanostructured photosensitizer in bacterial cells. *Sci Rep*, 5:15564, 2015.

[151] C.M. Yow, H.M. Tang, E.S. Chu, and Z. Huang. Hypericin-mediated photodynamic antimicrobial effect on clinically isolated pathogens. *Photochem Photobiol.*, 88(3):626–632, 2012.

[152] J.M. Jacobson, L. Feinman, L. Liebes, N. Ostrow, V. Koslowski, A. Tobia, B.E. Cabana, D. Lee, J. Spritzler, and A.M. Prince. Pharmacokinetics, safety, and antiviral effects of hypericin, a derivative of St. John's wort plant, in patients with chronic hepatitis C virus infection. *Antimicrob Agents Chemother.*, 45(2):517–524, 2001.

[153] S. Shui, Z. Zhao, H. Wang, M. Conrad, and G. Liu. Non-enzymatic lipid peroxidation initiated by photodynamic therapy drives a distinct ferroptosis-like cell death pathway. *Redox Biol.*, 45:102056, 2021.

[154] H. Hirata, M. Kuwatani, K. Nakajima, Y. Kodama, Y. Yoshikawa, M. Ogawa, and N. Sakamoto. Near-infrared photoimmunotherapy (NIR-PIT) on cholangiocarcinoma using a novel catheter device with light emitting diodes. *Cancer Sci.*, 112(2):828–838, 2021.

[155] H. Yamaguchi, N. Pantarat, T. Suzuki, and A. Evdokiou. Near-infrared photoimmunotherapy using a small protein mimetic for HER2-overexpressing breast cancer. *Int J Mol Sci.*, 20(23):5835, 2019.

[156] Y.D. Heryanto, H. Hanaoka, T. Nakajima, A. Yamaguchi, and Y. Tsushima. Applying near-infrared photoimmunotherapy to B-cell lymphoma: comparative evaluation with radioimmunotherapy in tumor xenografts. *Ann Nucl Med.*, 31(9):669–677, 2017.

[157] T.A. Burley, J. Mączyńska, A. Shah, W. Szopa, K.J. Harrington, J.K.R. Boult, A. Mrozek-Wilczkiewicz, M. Vinci, J.C. Bamber, W. Kaspera, and G. Kramer-Marek. Near-infrared photoimmunotherapy targeting EGFR-shedding new light on glioblastoma treatment. *Int J Cancer*, 142(11):2363–2374, 2018.

[158] J. Mączyńska, F. Raes, C. Da Pieve, and et al. Triggering anti-GBM immune response with EGFR-mediated photoimmunotherapy. *BMC Medicine*, 20(1):179, 2022.

[159] E. Driehuis, S. Spelier, I. Beltrán Hernández, R. de Bree, S.M. Willems, H. Clevers, and S. Oliveira. Patient-derived head and neck cancer organoids recapitulate EGFR expression levels of respective tissues and are responsive to EGFR-targeted photodynamic therapy. *Clin Med.*, 8(11):1880, 2019.

[160] W. Peng, H.S. de Bruijn, E. Farrell, M. Sioud, V. Mashayekhi, S. Oliveira, G.M. van Dam, J.L.N. Roodenburg, M.J.H. Witjes, and D.J. Robinson. Epidermal growth factor receptor (EGFR) density may not be the only determinant for the efficacy of EGFR-targeted photoimmunotherapy in human head and neck cancer cell lines. *Lasers Surg Med.*, 50(5):513–522, 2018.

[161] E.Y. Lemma, A. Letian, N.K. Altorki, and T.E. McGraw. Regulation of PD-L1 trafficking from synthesis to degradation. *Cancer Immunol Res.*, 11(7):866–874, 2023.

[162] M. Burr, C. Sparbier, Y.C. Chan, and et al. CMTM6 maintains the expression of PD-L1 and regulates anti-tumour immunity. *Nature*, 549(7670):101–105, 2017.

[163] H. Yao, J. Lan, C. Li, and et al. Inhibiting PD-L1 palmitoylation enhances T-cell immune responses against tumours. *Nat Biomed Eng.*, 3(4):306–317, 2019.

[164] A. Letian, E.Y. Lemma, P. Cavaliere, N. Dephoure, N.K. Altorki, and T.E. McGraw. Proximity proteome mapping reveals PD-L1-dependent pathways disrupted by anti-PD-L1 antibody specifically in EGFR-mutant lung cancer cells. *Cell Commun Signal.*, 21(1):58, 2023.

[165] H. Zeng and et. al. Exosomal PD-L1 promotes the formation of an immunosuppressive microenvironment in gastric diffuse large B-cell lymphoma. *Oncol Rep.*, 49(5):88, 2023.

List of Acronyms

BSA	Bovine Serum Albumin
DMEM	Dulbecco's Modified Eagle Medium
DMSO	Dimethyl Sulfoxide
DOL	Degree of Labeling
EITC	Eosin 5-Isothiocyanate
FBS	Fetal Bovine Serum
FDA	Food and Drug Administration
HOMO	Highest Occupied Molecular Orbital
IC	Internal Conversion
ICIs	Immune Checkpoint Inhibitors
IgG	Immunoglobulin G
ISC	Inter System Crossing
LFP	Laser Flash Photolysis
LUMO	Least Unoccupied Molecular Orbital
MFI	Median Fluorescence Intensity
NSCLC	Non-Small Cell Lung Cancer
PBS	Phosphate-buffered Saline
PCI	Photochemical Internalization
PD-1	Programmed Cell Death Protein-1
PD-L1	Programmed Cell Death Ligand-1
PDT	Photodynamic Therapy
PET	Photo-induced Electron Transfer
PFA	Paraformaldehyde
PI	Propidium Iodide
PIT	Photoimmunotherapy
PS	Photosensitizer
RIPs	Ribosome-Inactivating Proteins
ROS	Reactive Oxygen Species
RPMI	Roswell Park Memorial Institute

SOSG	Singlet Oxygen Sensor Green
STORM	STochastic Optical Reconstruction Microscopy
TCSPC	Time-Correlated Single Photon Counting
TIRF	Total Internal Reflection Fluorescence
TME	Tumor Microenvironment
VR	Vibrational Relaxation

List of Figures

List of Tables

Acknowledgement

I would like to express my gratitude to my supervisor, Prof. Stefania Abbruzzetti, for her guidance throughout this project. Her expertise has been important in shaping both my research and my PhD journey. I am also very grateful to Prof. Cristiano Viappiani and my colleagues in the Biophysics group at the University of Parma, Pietro Delcanale, Andrea Mussini, and Lucia Bellanova. Their contributions and support have been essential over the years.

During my PhD, I had the opportunity to collaborate with different remarkable research groups who warmly welcomed me into their teams. I was incredibly fortunate to meet wonderful people and inspiring scientists whose enthusiasm for research and kindness made these experiences truly meaningful.

Most of the biological assays and PDT experiments presented in this work were performed in collaboration with the group of Prof. Pier Giorgio Petronini at the Department of Medicine and Surgery (University of Parma). I am especially grateful to Claudia Fumarola and Maricla Galletti for their constant support and guidance; much of what I have learned about cellular biology is due to their teaching and expertise.

I am particularly thankful to Dr. Pål Selbo and Dr. Kristian Berg for hosting me in their laboratory at the Institute for Cancer Research in Oslo (Norway). Although brief, my time with their group was an invaluable educational experience, and great opportunity to learn about PCI technology. I also thank Ellen Skarpen for her help with confocal experiments and colocalization analysis, and Magdaléna for being both a fantastic colleague and an amazing friend.

Some of the confocal experiments presented here were conducted at the Italian Institute of Technology in Genoa (Italy), in collaboration with the Nanoscopy group led by Prof. Alberto Diaspro. My thanks extend to Prof. Paolo Bianchini for his supervision, as well as to Matteo Mariangeli and Simone Civita for their assistance in the lab and for their friendship.

Finally, I would like to gratefully acknowledge the financial support provided to this PhD project by the University of Parma (grant "Bando di Ateneo per la Ricerca 2020 - PARTE 1 - Azione A1: A multi-strategy approach for PD-L1-targeted Photodynamic Therapy"), and the Fondazione di Piacenza e Vigevano (project "La terapia fotodinamica targeted: un approccio multivalente per il trattamento dei tumori con una possibile rilevanza per l'epidemia SARS-CoV-2").